Construction of the perturbed gravitational field induced by a rotating ring around a black hole and the visualization of space-time curvature with tendex and vortex lines

Yasumichi Sano

Department of Earth and Space Science

Graduate School of Science

Osaka University, Osaka, JAPAN

1-1 Machikaneyama-cho, Toyonaka, Osaka 560-0043, Japan

sano@vega.ess.sci.osaka-u.ac.jp

Abstract

Extreme mass ratio inspirals are one of the important candidates of gravitational wave source. They are binary systems which are composed of a massive black hole and a stellar-mass compact object at galactic centers. For the future gravitational wave astronomy, it is very important to predict the wave forms accurately. For that purpose, we need to know the accurate motion of the smaller object in the black hole space-time. The motion of the smaller object is different from the motion of a test particle due to the gravitational self-force, which is the effect of the perturbation of the space-time induced by the object itself. Therefore it is important to calculate the perturbation of the black hole space-time induced by the accompanying small mass.

The perturbation of a black hole space-time at the first order of (m/M) has been considered by many authors, where M and m are the black hole mass and the mass of smaller object, respectively. In the case of the Schwarzschild black hole (non-spinning, spherical black hole), one can calculate the metric perturbation by solving the separated radial equations by Regge & Wheeler (1957) and Zerilli (1970). However, in the case of the spinning Kerr black hole, the same formalism cannot be used due to lack of spherical symmetry. On the other hand, it is known that the perturbation of the Newman-Penrose variables, ψ_0 and ψ_4, can be calculated by solving the Teukolsky equations (Teukolsky 1973). However, the construction of the metric perturbation from ψ_0 and ψ_4 is a non-trivial problem, and it has been a long-standing problem to obtain the metric perturbation.

In the first part of this thesis, we investigate a method to construct the metric perturbation

from ψ_0 and ψ_4 via the Hertz potential. One problem of this method is that the ψ_0 and ψ_4 do not have the information of $l = 0$ and $l = 1$ modes of the perturbations. These lower mode perturbations are mass and angular momentum perturbation of the space-time, respectively. To tackle this problem, we consider the perturbations of the Schwarzschild and Kerr metric by a rotating ring, and find a procedure to include the lower mode perturbations properly. As a result, for the first time, we obtain the explicit Kerr metric perturbation including both mass and angular momentum perturbation, using the Hertz potential. We also consider the perturbation of the Kerr metric by a point particle at rest, and obtain the metric perturbation in a similar manner as the ring case.

In the second part of this thesis, we consider the visualization of space-time curvature, using the tendex and vortex line. This method was proposed by Nichols *et al.* (2011). These lines are associated with the tidal and frame-dragging effects of the space-time. We visualize our results of the perturbed Kerr space-time and discuss the outcomes. Further, we visualize the space-time of a black hole binary which is constructed by a different study. It is an approximate black hole binary space-time obtained by the asymptotic matching method by Mundim *et al.* (2014). Through our visualization, we find unphysical distortions of the lines produced by the insufficient accuracy of the metric. We discuss how we can improve the asymptotic matching to avoid these unphysical distortions of tendex and vortex lines.

Contents

Acknowledgements

First, I would like to give great thanks to Professor Hideyuki Tagoshi for being my supervisor for years. I could continue the research and write papers and this thesis because he supported and encouraged me patiently.

Next I would like to thank Professors Kentaro Nagamine, Fumio Takahara, Yutaka Fujita, and Toru Tsuribe for their support and discussions. I would also like to thank our secretary, Ms. Yasuko Nishii, for her kind support. I also wish to thank every student and postdoctoral researcher I have ever met in the Theoretical Astrophysics Group at Osaka University. They enriched my life in the lab very much. In addition, I wish to thank one irreplaceable friend Mana Kishimoto for inspiring, encouraging, and caring me continuously.

Finally, I would like to thank my parents for their unconditional support.

Chapter 1

Introduction

An astronomical black hole can be described by the Kerr metric. The Kerr metric is a stationary, axisymmetric exact solution of the Einstein equation. It was discovered by Kerr in 1963, about 50 years after the Schwarzschild metric was found (1916), which is the static and spherically symmetric exact solution (non-spinning black hole). Indeed it took a long time to find the rotating generalization of it.

After the Schwarzschild metric was found, its stability was studied. Regge and Wheeler (1957) discussed the first order perturbations of the Schwarzschild metric, and found that the odd-parity perturbations can be described by a separated radial ordinary differential equation. Later, Zerilli (1970) derived the radial equation for the even-parity. The formalism by Regge, Wheeler, and Zerilli (RWZ) allows us to calculate the first order metric perturbation. In their formalism, it is possible to decompose the perturbation equation for metric using spherical harmonics and Fourier transformation. In other words, the formalism relies on the spherical symmetry of the Schwarzschild metric.

On the other hand, because the Kerr metric does not have spherical symmetry, the RWZ formalism cannot be applied. However, Teukolsky (1972, 1973) found a separated radial ordinary differential equation (Teukolsky equation) using the Newman-Penrose formalism. By solving the Teukolsky equation, one can obtain the perturbations of ψ_0 and ψ_4, which correspond to

the ingoing and outgoing gravitational radiation, respectively. The ψ_0 and ψ_4 are part of the Weyl scalars, which are complex quantities defined with components of the Weyl tensor, which is the trace-free part of the Riemann curvature tensor (see Chapter 2 for definitions). The perturbation equation is decomposed using spin-weighted spheroidal harmonics and Fourier transformation. For spin $s = \pm 2$, ± 1, and 0, the Teukolsky equation becomes equations for the Weyl scalars ψ_0 and ψ_4, electromagnetic field, and neutrino field, respectively. Despite of the remarkable discovery of the Teukolsky equation, calculation of the metric perturbation for the case of the Kerr metric has been a long-standing problem.

Investigating the perturbation of the Kerr metric is not only interesting theoretically, but also important in the context of gravitational wave astronomy. Extreme mass ratio inspirals are one of the promising and important candidates of gravitational wave sources. They are binary systems composed of a massive black hole of mass M and a stellar-mass compact object of mass m at galactic centers. The gravitational wave is emitted while the smaller object inspirals into the massive black hole. There are many future projects aiming to observe the gravitational wave from such binaries with space laser interferometers, such as eLISA (Amaro-Seoane *et al.* 2011), DECIGO (Seto *et al.* 2001; Kawamura *et al.* 2011), and BBO (Crowder & Cornish 2005). For a detection by a detector such as eLISA, masses have to be in the range $M \sim 10^5 - 10^7 M_\odot$ and $m \sim 1 - 10^2 M_\odot$, based on the constraints of the frequency and amplitude of the wave. The mass ratio then becomes $\mu \equiv m/M \sim 10^{-7} - 10^{-3}$. Such system emits gravitational wave for a long time $\sim \mu^{-1} MG/c^3$, which corresponds to many orbital cycles before the smaller object plunges into the massive black hole (Amaro-Seoane *et al.* 2014). Therefore, it is necessary to model the motion accurately so that the phase of predicted waveform matches. Higher accuracy is required for parameter estimation, which is to extract physical information of the EMRI from an detected signal.

The self-force formalism has been developed to describe the motion of the small object around a black hole. In the test particle limit, the small object obeys the geodesic motion which is derived from the unperturbed black hole metric. However, when we take into account

the distortion of the space-time by the small object, the motion is influenced. We write the metric of the system as

$$g_{\mu\nu} = g^{(0)}_{\mu\nu} + h^{(1)}_{\mu\nu} + h^{(2)}_{\mu\nu} + \mathcal{O}(\mu^3), \tag{1.1}$$

where $g^{(0)}_{\mu\nu}$ is the unperturbed metric of the black hole, and $h^{(1)}_{\mu\nu}$ and $h^{(2)}_{\mu\nu}$ denote the first and second order perturbation, respectively. The equation of motion of the small object can be written as

$$\frac{D^2 z^\mu}{\mathrm{d}\tau^2} = F_1^\mu + F_2^\mu + \mathcal{O}(\mu^3), \tag{1.2}$$

where $z^\mu(\tau)$ is the object's world line. The proper time τ in the left-hand side is defined with respect to the unperturbed metric $g^{(0)}_{\mu\nu}$ and the derivatives are also with respect to $g^{(0)}_{\mu\nu}$. In the limit of $\mu \to 0$, the right-hand side vanishes and the equation becomes the geodesic equation under $g^{(0)}_{\mu\nu}$. We call F_n^μ the nth-order gravitational self-force. Effects by the first-order F_1^μ and second-order F_2^μ are considered to be sufficient for parameter estimation. While many calculations of first-order effects have been performed for the Schwarzschild black hole case, the Kerr case is relatively less developed. The calculations for second-order effects still have a long way to go (Amaro-Seoane *et al.* 2014). Below we discuss the first-order perturbation of the metric, $h^{(1)}_{\mu\nu}$, which is required for both F_1^μ and F_2^μ.

It is proved that the first-order self-force on the small object can be given by the perturbation $h^{(1)}_{\mu\nu}$ which is induced by a point particle (Gralla & Wald 2008; Pound 2010). One method to compute $h^{(1)}_{\mu\nu}$ in the Kerr space-time is to directly solve the coupled partial differential equations numerically. On the other hand, there is a method to compute metric perturbation starting from the Teukolsky equation. In this method, we use the formalism by Chrzanowski (1975) and Kegeles & Cohen (1979), to construct the metric perturbation in a radiation gauge, via the Hertz potential. The first step is to obtain the Weyl scalars, ψ_0 and ψ_4, by solving the Teukolsky equation. The second step is to obtain the Hertz potential from ψ_0 and ψ_4. However, since ψ_0 and ψ_4 do not have the information of $l = 0$ and $l = 1$ modes, undetermined degrees of freedom remain in the Hertz potential. The lower modes of $l = 0$ and $l = 1$ are important, because they correspond to the mass perturbation and the angular momentum per-

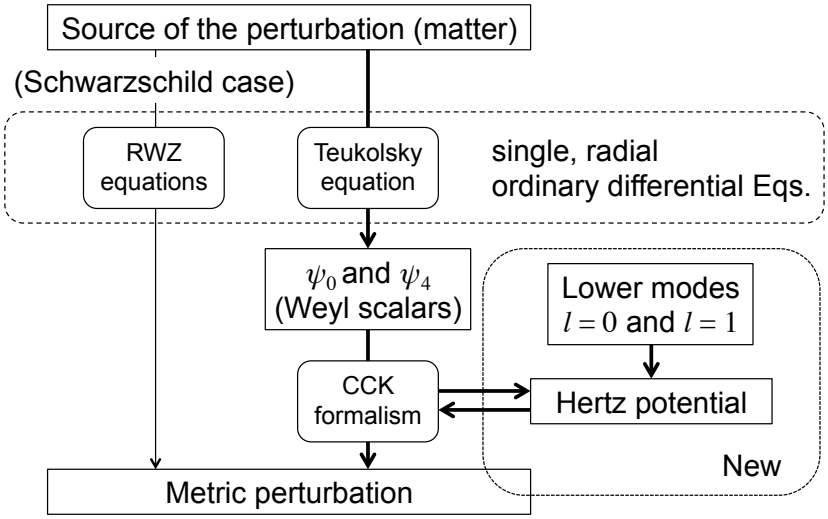

Figure 1.1: Formulations and methods to calculate the first order metric perturbation of a black hole space-time. For the Schwarzschild case, the formalism by Regge, Wheeler, and Zerilli (RWZ) allows us to obtain the metric perturbation by solving ordinary differential equations. However, their formalism cannot be used for the Kerr case. The thick arrows represent the method we take. In this method we first obtain the Weyl scalars (ψ_0 and ψ_4) by solving the Teukolsky equation, and find the Hertz potential using ψ_0 and ψ_4, in the formalism by Chrzanowski, Cohen, and Kegels (CCK). Since these two Weyl scalars do not have the information of $l = 0$ and $l = 1$ modes, including these modes is not a trivial problem.

turbation of the space-time, respectively. Including these information and determining other degrees of freedom are the difficult points in this method. Fig. 1.1 summarizes the formalism and methods.

Keidl, Friedman, & Wiseman (2007) are the first people who calculated the explicit metric perturbation by matter using this method. They considered the perturbation of the Schwarzschild space-time by a particle at rest. They considered this model because it is very simple, though it is unphysical that a particle is at rest in the gravitational field of a black hole. They found that the undetermined degrees of freedom in the Hertz potential reduce to

eight complex constants, and determined them by considering the regularity of the perturbed gravitational field. In their space-time, they found an inevitable singular line, which starts from the particle and radially extends to the event horizon or infinity. They also investigated the meaning of each constant, and identified which one corresponds to the mass perturbation, angular momentum perturbation, and gauge freedom. Since their set-up is unphysical, interpretation of the value of mass perturbation is unclear. The angular momentum perturbation was not included in the model either. Despite of these problems, as a next step, Friedman's group studied the self-force on a particle which is on a circular orbit on the equatorial plane of the Schwarzschild space-time (Keidl *et al.* 2010; Shah *et al.* 2011) and the Kerr space-time (Shah, Friedman, & Keidl 2012). They numerically obtained the gauge invariant effects of the self-force. However, they no longer used the Hertz potential to add the lower modes in those works. They added the lower mode perturbation in a gauge that they call "Kerr gauge." It means that the constructed metric perturbation is not in the radiation gauge.

In the first part of this thesis, we consider the perturbation of the black hole space-time by a circular, rotating mass ring, in order to resolve the questions which remained in the study of Keidl, Friedman, & Wiseman (2007). There are two reasons why we consider a rotating ring. The first reason is its simplicity. Perturbed space-time is stationary and axisymmetric, as in the rest particle case. The second one is the angular momentum. Since the ring is rotating, we can deal with both the mass and angular momentum perturbation of the space-time, which are important in the orbiting particle case too. As the unperturbed black hole space-time, the Schwarzschild metric and the Kerr metric are considered. We present an explicit procedure to construct the metric perturbation. We also apply this procedure to the perturbation of the Kerr metric by a particle at rest, the Kerr version of the work by Keidl, Friedman, & Wiseman (2007). We discuss the parameters which correspond to the mass and angular momentum perturbation in the Hertz potential. Fig. 1.2 summarizes the previous works and our works.

This study of constructing the metric perturbation in the radiation gauge becomes impor-

	Previous works			This work		
	Keidl+07	Keidl+10	Shah+12	**Sano+14**	**Sano+15**	
Black Hole	Schwarzschild	Schwarzschild	Kerr	Schwarzschild	Kerr	Kerr
Matter	Particle at rest	Particle: circular geodesics		Rotating ring		Particle at rest
Configuration	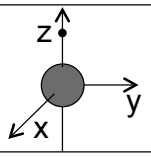	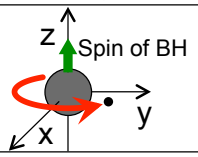		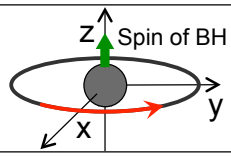		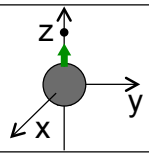
Lower modes	$l = 0$	$l = 0$ and $l = 1$ in "Kerr gauge"		$l = 0$ and $l = 1$		$l = 0$
Result	Metric perturbation in radiation gauge	Gauge invariant effects of self-force		Metric perturbation in radiation gauge		

Figure 1.2: Calculations of metric perturbation using the CCK formalism, which can be used for Kerr metric perturbations. Shah, Friedman, & Keidl (2012) numerically obtained the gauge invariant effects of the self-force on a circular orbiting particle. However, the relation to the standard formulation for the self-force is unclear. We examine the method to obtain the metric perturbation including the lower modes, $l = 0$ and $l = 1$, in a radiation gauge. We consider the perturbation by a rotating ring around a black hole (BH) because the set-up is simple (stationarity and axisymmtery) and both $l = 0$ and $l = 1$ are involved. We also consider the Kerr version of the work by Keidl, Friedman, & Wiseman (2007) because the set-up is simple.

tant when we use the newly proposed prescription for calculating the self-force. The MiSaTaQuWa formulation (Mino, Sasaki, & Tanaka 1997; Quinn & Wald 1997) for the calculation of the self-force requires the metric perturbation in the Lorenz gauge as an input. Pound, Merlin, & Barack (2014) found local gauge transformations that allow us to move from the radiation gauge to the Lorenz gauge. The problem of the inevitable singularity is also dealt with. Our result in this thesis is an important preparation for the actual calculation of the self-force using the method by Pound, Merlin, & Barack (2014).

In the last part of this thesis, we consider the visualization of the space-time curvature using tendex and vortex line, which was proposed by Nichols *et al.* (2011). These lines are basically field lines which represent the tidal effect and the frame-dragging effect of the space-

time curvature. Since they have physical meanings, they could be of some help for intuitive understanding of the space-time. Nichols *et al.* (2011) proposed this tool for the visualization of numerical relativity simulations and for obtaining new insights. Basic properties of the lines, dependence on the coordinate transformations, and typical patterns of the lines produced by quasi-normal modes of a black hole were studied in the subsequent works by the same people (Zhang *et al.* 2012; Nichos *et al.* 2012). We use the tendex and vortex lines to visualize our results of perturbed metric. We obtain representations that are useful for explaining the procedure to add the lower mode perturbations. We also apply the visualization to a binary black hole space-time which was analytically constructed using the asymptotic matching method by Mundim *et al.* (2014). Through our visualization, we discuss the accuracy of the matching and other properties of the space-time, including the propagating gravitational wave.

This thesis is organized as follows. In Chapter 2, we review the Newman-Penrose formalism and the Teukolsky equation. In Chapter 3, we review the CCK formalism. Formulae for calculating the metric perturbation from the Hertz potential are presented. In Chapter 4, we consider the perturbation induced by a rotating ring around a black hole (Sano & Tagoshi 2014, 2015). We present a method to include the lower modes properly. We also consider the perturbation of the Kerr metric by a particle at rest. The visualization is discussed in Chapter 5. We conclude in Chapter 6. Throughout this thesis, we adopt the units of $c = G = 1$.

Chapter 2

Teukolsky equation

In this chapter, we review basic formulae including the Teukolsky equation, which are used to obtain the metric perturbation in the Kerr background. We also discuss the symmetry of the equations.

2.1 Tetrad formalism

We denote the tetrad by $(e_\mu)^a$, where $\mu = 1,\ 2,\ 3,\ 4$ is the label of basis vectors and a is the "slot" in the context of the abstract index notation (Wald 1984). The dual basis vectors $(e^\nu)_b$ are defined by

$$(e_\mu)^a(e^\nu)_a = \delta_\mu{}^\nu, \tag{2.1}$$

and they satisfy

$$\sum_\mu (e_\mu)^a(e^\mu)_b = \delta^a{}_b. \tag{2.2}$$

Below, we omit $\sum$ adopting the Einstein summation convention.

We denote the tetrad components of the metric g_{ab} by $\eta_{\mu\nu}$ and assume that they are constant:

$$\eta_{\mu\nu} = g_{ab}(e_\mu)^a(e_\nu)^b, \quad \eta^{\mu\nu} = g^{ab}(e^\mu)_a(e^\nu)_b. \tag{2.3}$$

The tetrad components of $\nabla_b A_a$ can be written as

$$\begin{aligned} A_{\mu;\nu} \equiv (\nabla_b A_a)(e_\mu)^a(e_\nu)^b &= [\nabla_b (A_\kappa)(e^\kappa)_a](e_\mu)^a(e_\nu)^b \\ &= (\nabla_b A_\kappa)(e^\kappa)_a(e_\mu)^a(e_\nu)^b + A_\kappa(\nabla_b(e^\kappa)_a)(e_\mu)^a(e_\nu)^b \\ &= (e_\nu)^b(\partial_b A_\kappa)\delta^\kappa{}_\mu + A_\kappa \eta^{\kappa\rho}(\nabla_b(e_\rho)_a)(e_\mu)^a(e_\nu)^b \\ &= A_{\mu,\nu} + A_\kappa \eta^{\kappa\rho}\gamma_{\rho\mu\nu}, \end{aligned} \tag{2.4}$$

where we define the directional derivative $A_{\mu,\nu} \equiv (e_\nu)^b \partial_b A_\mu$ and the Ricci rotation coefficients,

$$\gamma_{\rho\mu\nu} \equiv (\nabla_b(e_\rho)_a)(e_\mu)^a(e_\nu)^b = -\gamma_{\mu\rho\nu}. \tag{2.5}$$

This definition follows Newman & Penrose (1962). While we use this definition, other references use different notations and definitions. See Appendix A on this matter.

2.2 Newman-Penrose formalism

In the Newman-Penrose formalism, we use null tetrad which satisfies $(e_\mu)_a(e_\mu)^a = 0$:

$$(e_1)^a = l^a, \quad (e_2)^a = n^a, \quad (e_3)^a = m^a, \quad (e_4)^a = \overline{m}^a. \tag{2.6}$$

Here, $\overline{m}^a$ is the complex conjugate of m^a. We choose them so that

$$-l_a n^a = m_a \overline{m}^a = 1, \quad l_a m^a = l_a \overline{m}^a = n_a m^a = n_a \overline{m}^a = 0 \tag{2.7}$$

hold. Namely, the non-zero tetrad components of the metric are $\eta_{12} = \eta_{21} = -1$ and $\eta_{34} = \eta_{43} = 1$.

The Weyl tensor C_{abcd} is the trace free part of the Riemann curvature tensor R_{abcd} (Wald 1984):

$$C_{abcd} = R_{abcd} - (g_{a[c}R_{d]b} - g_{b[c}R_{d]a}) + \frac{1}{3}R g_{a[c}g_{d]b}, \tag{2.8}$$

where $R_{ab} = R_{adb}{}^d$ is the Ricci tensor and $R = R_a{}^a$ is the Ricci scalar. Any trace of the Weyl tensor C_{abcd} vanishes. At a vacuum point of the space-time, $C_{abcd} = R_{abcd}$ holds because the

Ricci tensor R_{ab} vanishes at such a point, according to the Einstein equation in the following form:

$$R_{ab} = 8\pi \left(T_{ab} - \frac{1}{2} g_{ab} T \right), \tag{2.9}$$

where T_{ab} is the energy-momentum tensor, and $T = T_a{}^a$. Units with $c = G = 1$ are used.

While the Riemann tensor has 20 independent components, the Weyl tensor has 10 independent components. In the Newman-Penrose formalism, the independent complex components are chosen as follows:

$$\Psi_0 = +C_{1313}, \quad \Psi_1 = +C_{1312}, \quad \Psi_2 = +C_{1342}, \quad \Psi_3 = +C_{1242}, \quad \Psi_4 = +C_{4242}. \tag{2.10}$$

These are called the Weyl scalars.

Next, we define the spin coefficients in terms of the Ricci rotation coefficients:

$$\kappa = -\gamma_{131}, \qquad \rho = -\gamma_{134}, \qquad \varpi = +\gamma_{241}, \qquad \lambda = +\gamma_{244}, \tag{2.11a}$$

$$\nu = +\gamma_{242}, \qquad \mu = +\gamma_{243}, \qquad \tau = -\gamma_{132}, \qquad \sigma = -\gamma_{133}, \tag{2.11b}$$

$$\epsilon = -\frac{1}{2}(\gamma_{121} - \gamma_{341}), \qquad \alpha = +\frac{1}{2}(\gamma_{214} - \gamma_{434}), \tag{2.11c}$$

$$\gamma = +\frac{1}{2}(\gamma_{212} - \gamma_{432}), \qquad \beta = -\frac{1}{2}(\gamma_{123} - \gamma_{343}). \tag{2.11d}$$

These definitions are different by sign from the definitions in Newman & Penrose (1962). However, the value of each spin coefficients agree due to the difference of signature of the metric. See Appendix A for details.

2.3 Kerr metric

In this section, we review the Newman-Penrose quantities in the case of the Kerr space-time. In the Boyer-Lindquist coordinates, the Kerr metric is

$$\begin{aligned} \mathrm{d}s^2 = &- \left(1 - \frac{2Mr}{\Sigma} \right) \mathrm{d}t^2 - \frac{4Mar \sin^2\theta}{\Sigma} \mathrm{d}t\mathrm{d}\phi + \frac{\Sigma}{\Delta} \mathrm{d}r^2 \\ &+ \Sigma \mathrm{d}\theta^2 + \sin^2\theta \left(r^2 + a^2 + \frac{2Ma^2 r \sin^2\theta}{\Sigma} \right) \mathrm{d}\phi^2, \end{aligned} \tag{2.12}$$

where a is the Kerr parameter, $\Sigma = r^2 + a^2\cos^2\theta$, and $\Delta = r^2 - 2Mr + a^2$. The Kinnersley tetrad is used as a null tetrad associated with the Kerr metric:

$$l^a = \frac{r^2+a^2}{\Delta}(\partial_t)^a + (\partial_r)^a + \frac{a}{\Delta}(\partial_\phi)^a, \tag{2.13a}$$

$$n^a = \frac{\Delta}{2\Sigma}\left[\frac{r^2+a^2}{\Delta}(\partial_t)^a - (\partial_r)^a + \frac{a}{\Delta}(\partial_\phi)^a\right], \tag{2.13b}$$

$$m^a = \frac{1}{\sqrt{2}(r+ia\cos\theta)}\left[ia\sin\theta(\partial_t)^a + (\partial_\theta)^a + i\csc\theta(\partial_\phi)^a\right], \tag{2.13c}$$

where $(\partial_t)^a$, $(\partial_r)^a$, $(\partial_\theta)^a$, and $(\partial_\phi)^a$ are the coordinate basis vectors associated with the Boyer-Lindquist coordinates t, r, θ, and ϕ, respecitvely.

With the Kerr metric Eq. (2.12) and the Kinnersley tetrad Eq. (2.13), the non-vanishing spin coefficients are

$$\begin{gathered}\rho = -\frac{1}{r-ia\cos\theta}, \quad \mu = \frac{\Delta}{2\Sigma}\rho, \quad \gamma = \mu + \frac{r-M}{2\Sigma}, \\ \varpi = \rho^2\frac{ia\sin\theta}{\sqrt{2}}, \quad \tau = \frac{\rho}{\overline{\rho}}\overline{\varpi}, \quad \beta = -\overline{\rho}\frac{\cot\theta}{2\sqrt{2}}, \quad \alpha = \varpi - \overline{\beta}.\end{gathered} \tag{2.14}$$

The non-zero Weyl scalar is

$$\begin{aligned}\Psi_2 = M\rho^3 &= 2\gamma\rho - 2(2\beta+\tau)\varpi \\ &= 2\gamma\rho - 2(2\alpha-\varpi)\tau.\end{aligned} \tag{2.15}$$

Other Weyl scalars, Ψ_0, Ψ_1, Ψ_3, and Ψ_4, are zero for the unperturbed Kerr metric. The first order correction to each Weyl scalar is denoted by ψ_0, ψ_1, ψ_2, and ψ_4, respectively. Because the unperturbed Ψ_0, Ψ_1, Ψ_3, and Ψ_4 are zero, perturbations ψ_0 and ψ_4 are gauge invariant quantities, and called ingoing and outgoing radiative part, respectively (Teukolsky 1972, 1973). They have the real part and the imaginary part, which correspond to the two degrees of freedom of the gravitational radiation. However, ψ_0 and ψ_4 do not contain the information on the perturbation in the mass and the angular momentum of the space-time. That means, for a non-vacuum perturbation, ψ_0 and ψ_4 alone do not uniquely specify the gravitational perturbation (Wald 1973).

2.4 Partial derivative operators

In the Newman-Penrose formalism, many symbols are used to denote partial derivative operators. We mention their definitions, and introduce some auxiliary symbols that we use for later explanations. Further, we briefly discuss the notation of spin-weight raising and lowering operators.

First, we define four directional derivatives along the Kinnersley tetrad (2.13):

$$\boldsymbol{D} \equiv {}_{,1} = l^a \partial_a, \quad \boldsymbol{\Delta} \equiv {}_{,2} = n^a \partial_a, \quad \boldsymbol{\delta} \equiv {}_{,3} = m^a \partial_a, \quad \overline{\boldsymbol{\delta}} = {}_{,4} = \overline{m}^a \partial_a. \tag{2.16}$$

We also use auxiliary symbols,

$$\tilde{\boldsymbol{D}} \equiv -\frac{2\Sigma}{\Delta}\boldsymbol{\Delta}, \quad \tilde{\boldsymbol{\Delta}} \equiv -\frac{\Delta}{2\Sigma}\boldsymbol{D}, \quad \tilde{\boldsymbol{\delta}} \equiv \frac{\overline{\rho}}{\rho}\overline{\boldsymbol{\delta}}, \quad \tilde{\overline{\boldsymbol{\delta}}} = \overline{\tilde{\boldsymbol{\delta}}} \equiv \frac{\rho}{\overline{\rho}}\boldsymbol{\delta}. \tag{2.17}$$

These are the $(t \to -t,\ \phi \to -\phi)$ versions of the original $\boldsymbol{D}$, $\boldsymbol{\Delta}$, $\boldsymbol{\delta}$, and $\overline{\boldsymbol{\delta}}$. The first one, $\tilde{\boldsymbol{D}}$ is used in Keidl *et al.* (2010) and other previous papers. We follow the notation by Keidl *et al.* (2010). Below we have several pairs of equations which are related each other by $(l^a \leftrightarrow n^a,\ m^a \leftrightarrow \overline{m}^a)$ exchanges. By using the auxiliary symbols, the symmetry between two equations will be clear. Further, note that the "tilde" versions of directional derivatives become the same as the original ones in the case of stationary and axisymmetric space-time.

We introduce partial derivative operators $\eth^+_{(s)}$ and $\eth^-_{(s)}$,

$$\eth^+_{(s)} \equiv -(\partial_\theta + i \csc\theta \partial_\phi - s\cot\theta), \tag{2.18a}$$

$$\eth^-_{(s)} \equiv -(\partial_\theta - i \csc\theta \partial_\phi + s\cot\theta). \tag{2.18b}$$

These operators raises and lowers the spin weight s, respectively. The spin-weighted spherical harmonics ${}_sY_{lm}(\theta,\phi)$ can be obtained from the usual spherical harmonics $Y_{lm}(\theta,\phi) = {}_0Y_{lm}(\theta,\phi)$ using the following equations:

$$\eth^+_{(s)}\ {}_sY_{lm} = +\sqrt{(l-s)(l+s+1)}\ {}_{s+1}Y_{lm}, \tag{2.19a}$$

$$\eth^-_{(s)}\ {}_sY_{lm} = -\sqrt{(l+s)(l-s+1)}\ {}_{s-1}Y_{lm}. \tag{2.19b}$$

In some references including Newman & Penrose (1966), the raising and lowering operators are denoted by $\eth$ and $\overline{\eth}$. However, this overline does not mean the complex conjugate in this case:

$$\overline{\eth^{+}_{(s)}\ {}_sY_{lm}} = \eth^{-}_{(-s)}\ {}_s\overline{Y}_{lm} \neq \eth^{-}_{(s)}\ {}_s\overline{Y}_{lm}. \tag{2.20}$$

So we prefer the notation $\eth^{+}_{(s)}$ and $\eth^{-}_{(s)}$ in order to avoid confusions. We also explicitly put the subscript (s) because $\eth^{+}_{(s)}$ and $\eth^{-}_{(s)}$ depend on s.

We can derive

$$\eth^{-}_{(s+1)}\eth^{+}_{(s)} = \csc\theta\partial_\theta(\sin\theta\partial_\theta) + \csc^2\theta{\partial_\phi}^2 + 2si\csc^2\theta\cos\theta\partial_\phi - (s^2\cot^2\theta - s), \tag{2.21a}$$

$$\eth^{+}_{(s-1)}\eth^{-}_{(s)} = \csc\theta\partial_\theta(\sin\theta\partial_\theta) + \csc^2\theta{\partial_\phi}^2 + 2si\csc^2\theta\cos\theta\partial_\phi - (s^2\cot^2\theta + s). \tag{2.21b}$$

Note that in the right-hand side, only the sign before s differs. The operators $\eth^{+}$ and $\eth^{-}$ and directional derivatives $\boldsymbol{\delta}$ and $\overline{\boldsymbol{\delta}}$ are related as follows:

$$(\boldsymbol{\delta} - 2s\beta) = \frac{\overline{\rho}}{\sqrt{2}}[-ia\sin\theta\partial_t + \eth^{+}_{(s)}], \tag{2.22a}$$

$$(\overline{\boldsymbol{\delta}} + 2s\overline{\beta}) = \frac{\rho}{\sqrt{2}}[+ia\sin\theta\partial_t + \eth^{-}_{(s)}]. \tag{2.22b}$$

These relations are useful when we solve the Teukolsky equation, particularly in stationary and axisymmetric cases. In Keidl *et al.* (2010), they use $\mathcal{L}$ and write the equivalent equation as

$$(\boldsymbol{\delta} - 2s\beta) = \frac{\overline{\rho}}{\sqrt{2}}\mathcal{L}_s. \tag{2.23}$$

2.5 Teukolsky equation

The master equations for perturbed $\psi_{(s=2)} = \psi_0$ and $\psi_{(s=-2)} = \rho^{-4}\psi_4$ are given by Teukolsky (1973) as

$$\begin{aligned}
&[(\boldsymbol{D} - 4\rho - \overline{\rho})(\boldsymbol{\Delta} + \mu - 4\gamma) - (\boldsymbol{\delta} - \overline{\alpha} - 3\beta + \overline{\varpi} - 4\tau)(\overline{\boldsymbol{\delta}} - 4\alpha + \varpi) - 3\Psi_2]\psi_0 \\
&= 4\pi[-(\boldsymbol{\delta} - \overline{\alpha} - 3\beta + \overline{\varpi} - 4\tau)(\boldsymbol{\delta} - 2\overline{\alpha} - 2\beta + \overline{\varpi})T_{11} + (\boldsymbol{\delta} - \overline{\alpha} - 3\beta + \overline{\varpi} - 4\tau)(\boldsymbol{D} - 2\overline{\rho})T_{13} \\
&\qquad + (\boldsymbol{D} - 4\rho - \overline{\rho})(\boldsymbol{\delta} - 2\beta + 2\overline{\varpi})T_{13} - (\boldsymbol{D} - 4\rho - \overline{\rho})(\boldsymbol{D} - \overline{\rho})T_{33}] \quad (2.24)
\end{aligned}$$

and

$$\begin{aligned}
&[(\boldsymbol{\Delta} + 4\mu + \overline{\mu} + 3\gamma - \overline{\gamma})(\boldsymbol{D} - \rho) - (\overline{\boldsymbol{\delta}} + \overline{\beta} + 3\alpha - \overline{\tau} + 4\varpi)(\boldsymbol{\delta} + 4\beta - \tau) - 3\Psi_2]\psi_4 \\
&= 4\pi[-(\overline{\boldsymbol{\delta}} + \overline{\beta} + 3\alpha - \overline{\tau} + 4\varpi)(\overline{\boldsymbol{\delta}} + 2\overline{\beta} + 2\alpha - \overline{\tau})T_{22} + (\overline{\boldsymbol{\delta}} + \overline{\beta} + 3\alpha - \overline{\tau} + 4\varpi)(\boldsymbol{\Delta} + 2\overline{\mu} + 2\gamma)T_{24} \\
&+ (\boldsymbol{\Delta} + 4\mu + \overline{\mu} + 3\gamma - \overline{\gamma})(\overline{\boldsymbol{\delta}} + 2\alpha - 2\overline{\tau})T_{24} - (\boldsymbol{\Delta} + 4\mu + \overline{\mu} + 3\gamma - \overline{\gamma})(\boldsymbol{\Delta} + \overline{\mu} + 2\gamma - 2\overline{\gamma})T_{44}], \quad (2.25)
\end{aligned}$$

respectively. Here $T_{\mu\nu}$ is the tetrad components of the energy-momentum tensor T_{ab}. By using the auxiliary symbols Eq. (2.17), these equations can be rewritten as follows:

$$[(\boldsymbol{D} - 4\rho - \overline{\rho})(\boldsymbol{\Delta} + \mu - 4\gamma) - (\boldsymbol{\delta} - 2\beta - 4\tau)(\overline{\boldsymbol{\delta}} - 4\alpha + \varpi) - 3\Psi_2]\psi_{(2)} = 4\pi\frac{T_{(2)}}{\Sigma}, \quad (2.26)$$

$$[(\tilde{\boldsymbol{D}} - 4\rho - \overline{\rho})(\tilde{\boldsymbol{\Delta}} + \mu - 4\gamma) - (\tilde{\boldsymbol{\delta}} - 2\beta - 4\tau)(\overline{\tilde{\boldsymbol{\delta}}} - 4\alpha + \varpi) - 3\Psi_2]\frac{4}{\Delta^2}\psi_{(-2)} = 4\pi\frac{4}{\Delta^2}\frac{T_{(-2)}}{\Sigma}, \quad (2.27)$$

where we define $T_{(s=2)}$ and $T_{(s=-2)}$ as

$$\begin{aligned}
\frac{T_{(2)}}{\Sigma} &= -(\boldsymbol{\delta} - 2\beta - 4\tau)(\boldsymbol{\delta} - \overline{\varpi})T_{11} + (\boldsymbol{\delta} - 2\beta - 4\tau)(\boldsymbol{D} - 2\overline{\rho})T_{13} \\
&\qquad + (\boldsymbol{D} - 4\rho - \overline{\rho})(\boldsymbol{\delta} + 2\overline{\alpha})T_{13} - (\boldsymbol{D} - 4\rho - \overline{\rho})(\boldsymbol{D} - \overline{\rho})T_{33}, \quad (2.28)
\end{aligned}$$

$$\begin{aligned}
\frac{4}{\Delta^2}\frac{T_{(-2)}}{\Sigma} &= -(\tilde{\boldsymbol{\delta}} - 2\beta - 4\tau)(\tilde{\boldsymbol{\delta}} - \overline{\varpi})\frac{4\Sigma^2}{\Delta^2}T_{22} + (\tilde{\boldsymbol{\delta}} - 2\beta - 4\tau)(\tilde{\boldsymbol{D}} - 2\overline{\rho})\frac{2\Sigma}{-\Delta}\frac{\overline{\rho}}{\rho}T_{24} \\
&\qquad + (\tilde{\boldsymbol{D}} - 4\rho - \overline{\rho})(\tilde{\boldsymbol{\delta}} + 2\overline{\alpha})\frac{2\Sigma}{-\Delta}\frac{\overline{\rho}}{\rho}T_{24} - (\tilde{\boldsymbol{D}} - 4\rho - \overline{\rho})(\tilde{\boldsymbol{D}} - \overline{\rho})\frac{\overline{\rho}^2}{\rho^2}T_{44}. \quad (2.29)
\end{aligned}$$

The left hand sides of Eqs. (2.26) and (2.27) become

$$\frac{1}{2\Sigma}\left\{\left[\frac{(r^2+a^2)^2}{\Delta}-a^2\sin^2\theta\right]{\partial_t}^2+\frac{4Mar}{\Delta}\partial_t\partial_\phi+\left(\frac{a^2}{\Delta}-\frac{1}{\sin^2\theta}\right){\partial_\phi}^2\right.$$
$$-\frac{1}{\Delta^2}\partial_r(\Delta^3\partial_r)-\frac{1}{\sin\theta}\partial_\theta(\sin\theta\partial_\theta)-2s\left[\frac{a(r-M)}{\Delta}+\frac{i\cos\theta}{\sin^2\theta}\right]\partial_\phi$$
$$\left.-2s\left[\frac{M(r^2-a^2)}{\Delta}-r-ia\cos\theta\right]\partial_t+(s^2\cot^2\theta\mp s)\right\}\frac{\Delta^{s/2}\psi_{(s)}}{\Delta}. \quad (2.30)$$

In the last term, the upper sign $(-)$ is for $s=2$ and the lower sign $(+)$ is for $s=-2$. The same term appears in Eq. (2.21). Eq. (2.30) is a different, but equivalent expression of Eq. (4.7) in Teukolsky (1973). A more familiar expression is

$$L_{(s)}\psi_{(s)}=-8\pi T_{(s)}, \quad (2.31)$$

where

$$L_{(s)}\psi_{(s)}\equiv\left\{-\left[\frac{(r^2+a^2)^2}{\Delta}-a^2\sin^2\theta\right]{\partial_t}^2-\frac{4Mar}{\Delta}\partial_t\partial_\phi-\left(\frac{a^2}{\Delta}-\frac{1}{\sin^2\theta}\right){\partial_\phi}^2\right.$$
$$+\Delta^{-s}\partial_r(\Delta^{s+1}\partial_r)+\frac{1}{\sin\theta}\partial_\theta(\sin\theta\partial_\theta)+2s\left[\frac{a(r-M)}{\Delta}+\frac{i\cos\theta}{\sin^2\theta}\right]\partial_\phi$$
$$\left.+2s\left[\frac{M(r^2-a^2)}{\Delta}-r-ia\cos\theta\right]\partial_t-(s^2\cot^2\theta-s)\right\}\psi_{(s)}. \quad (2.32)$$

The equation can be separated as

$$\psi_{(s)}=\sum_{l,m}^{\infty}\int_{-\infty}^{\infty}\mathrm{d}\omega R^{(s)}_{lm\omega}(r)\ {}_sS^{a\omega}_{lm}(\theta)e^{im\phi}e^{-i\omega t}, \quad (2.33)$$

where ${}_sS^{a\omega}_{lm}(\theta)$ is the spin-weighted spheroidal harmonics. called spin-weighted spheroidal function (Teukolsky 1973).

The separated equations for radial and angular part are

$$\Delta^{-s}\frac{\mathrm{d}}{\mathrm{d}r}\left(\Delta^{s+1}\frac{\mathrm{d}}{\mathrm{d}r}\right)R^{(s)}_{lm\omega}+\left[\frac{K^2-2is(r-M)K}{\Delta}+4is\omega r-\lambda\right]R^{(s)}_{lm\omega}=-8\pi T^{(s)}_{lm\omega}, \quad (2.34)$$

$$\csc\theta\frac{\mathrm{d}}{\mathrm{d}\theta}\left(\sin\theta\frac{\mathrm{d}}{\mathrm{d}\theta}\right){}_sS^{a\omega}_{lm}+(-a^2\omega^2\sin^2\theta+2a\omega m-2a\omega s\cos\theta){}_sS^{a\omega}_{lm}$$
$$+\left(-\frac{2ms\cos\theta}{\sin^2\theta}-\frac{m^2}{\sin^2\theta}-s^2\cot^2\theta+s+\lambda\right){}_sS^{a\omega}_{lm}=0, \quad (2.35)$$

where $K = (r^2 + a^2)\omega - am$, and λ is the separation constant. When $a\omega = 0$, it follows $\lambda = (l - s)(l + s + 1)$ and the spin-weighted spheroidal harmonics become the spin-weighted spherical harmonics ${}_sY_{lm}(\theta, \phi) = {}_sS^0_{lm}(\theta)e^{im\phi}$. For fixed s, m, and $a\omega$, the minimum of l is $l_{\min} = \max(|m|, |s|)$. The separated ordinal differential equation for the radial part Eq. (2.34) is the Teukolsky equation. The source term $T^{(s)}_{lm\omega}$ is defined as

$$T^{(s)}_{lm\omega} \equiv \frac{1}{2\pi}\int_{-\infty}^{\infty} \mathrm{d}t \int_0^{\pi} \mathrm{d}\theta \int_0^{2\pi} \mathrm{d}\phi \sin\theta \; {}_sS^{a\omega}_{lm} e^{-im\phi} e^{i\omega t} T_{(s)}. \tag{2.36}$$

2.6 Summary of this chapter

We reviewed the Newman-Penrose formalism. A complex null tetrad (l^a, n^a, m^a, $\overline{m}^a$) is used, and the Weyl scalars (ψ_0, ψ_1, ψ_2, ψ_3, and ψ_4) are defined as tetrad components of the Weyl tensor, which is the trace-free part of the Riemann curvature tensor. The five complex Weyl scalars are defined such that they are the 10 independent components of the Weyl tensor.

The first order perturbation equations for ψ_0 and ψ_4 are separated using the spin-weighted spheroidal harmonics ${}_sS^{a\omega}_{lm}(\theta)$. The two Weyl scalars are decomposed as Eq. (2.33). The separated equations, the Teukolsky equations Eq. (2.34) are second order ordinary differential equations. The ψ_0 and ψ_4 represent the ingoing and outgoing gravitational radiation field, respectively. When we consider vacuum perturbation ($T_{ab} = 0$, only radiation), it is known that the real part and imaginary part of ψ_0 or ψ_4 have complete information (the two degrees of freedom of gravitational radiation) to specify the perturbed space-time. However, we are interested in non-vacuum perturbation because we want to consider a particle orbiting around the black hole around the Kerr black hole. The source term is constructed as Eq. (2.36) with Eqs. (2.28) and (2.29) from the energy-momentum tensor T_{ab}.

Chapter 3

CCK formalism

The Hertz potential (Hertzian potential) was introduced as a super potential in electromagnetism by Hertz (1889), and the general theory was developed by Nisbet (1955). The frequently used scalar and vector potentials, ϕ and $\boldsymbol{A}$ are related with the electric and magnetic field as $\boldsymbol{E} = -\boldsymbol{\nabla}\phi - \dot{\boldsymbol{A}}$, $\boldsymbol{B} = \boldsymbol{\nabla} \times \boldsymbol{A}$, where $\dot{\boldsymbol{A}} \equiv \partial \boldsymbol{A}/\partial t$. Further, the Hertzian potentials $\boldsymbol{\Pi}_e$ and $\boldsymbol{\Pi}_m$ are introduced as potentials for ϕ and $\boldsymbol{A}$. The potentials ϕ and $\boldsymbol{A}$ are expressed as $\phi = -\boldsymbol{\nabla}\cdot\boldsymbol{\Pi}_e$, $\boldsymbol{A} = \dot{\boldsymbol{\Pi}}_e + \boldsymbol{\nabla} \times \boldsymbol{\Pi}_m$. For a given electromagnetic field, the Hertzian potentials are not unique. By investigating gauge transformations, Nisbet showed that the Hertzian potentials $\boldsymbol{\Pi}_e$ and $\boldsymbol{\Pi}_m$ can be reduced to only two scalar functions and each function obey a second order wave equation.

Cohen and Kegeles extended this and presented a new method to compute electromagnetic fields in curved space-time (Cohen & Kegeles 1974). This method was further extended by Chrzanowski, Cohen, and Kegeles. They devised a procedure to construct neutrino, electromagnetic, and gravitational perturbation of the Kerr black hole space-time (Chrzanowski 1975; Cohen & Kegeles 1975; Kegeles & Cohen 1979). Hence their formalism is called the CCK formalism. Wald (1978) and Stewart (1979) also developed the formalism further, and made it more rigorous.

In the CCK formalism, a radiation gauge is used. In that gauge, the first order perturbation

of the space-time metric can be expressed in terms of second derivatives of the Hertz potential. The Hertz potential obeys the Teukolsky equation with $T_{ab} = 0$ (vacuum). The metric perturbation in the ingoing radiation gauge ($h_{ab}l^b = h_a{}^a = 0$) is obtained from the Hertz potential which is a vacuum solution for $\psi_{(s=-2)}$. The metric perturbation in the outgoing radiation gauge ($h_{ab}n^b = h_a{}^a = 0$) is obtained from the Hertz potential which is a vacuum solution for $\psi_{(s=2)}$.

Though we have explicit formulae for computing the metric perturbation from the Hertz potential, obtaining the Hertz potential for a specific perturbation is another problem. Indeed, finding the Hertz potential is the most important and difficult problem in this method to construct the metric perturbation. We investigate this problem.

In the following sections below we assume that the unperturbed space-time is described by the Kerr metric.

3.1 Ingoing radiation gauge

The ingoing radiation gauge (IRG) is defined by the conditions $h_{ab}l^b = h^a{}_a = 0$. In this gauge, the perturbed metric h_{ab} is related to the Hertz potential as (Kegeles & Cohen 1979)

$$\begin{aligned} h_{ab} = -\Big[\Big\{ l_a l_b(\overline{\boldsymbol{\delta}} + 2\overline{\beta} + \varpi - \overline{\tau}) - \overline{m}_{(a}l_{b)}(\boldsymbol{D} + \rho - \overline{\rho})\Big\}(\overline{\boldsymbol{\delta}} + 4\overline{\beta} + 3\overline{\tau}) \\ + \Big\{ -l_{(a}\overline{m}_{b)}(\overline{\boldsymbol{\delta}} + 4\overline{\beta} - 2\varpi - \overline{\tau}) + \overline{m}_a\overline{m}_b(\boldsymbol{D} - \overline{\rho})\Big\}(\boldsymbol{D} + 3\overline{\rho})\Big]\overline{\Psi} + [\text{c.c.}] \ , \end{aligned} \tag{3.1}$$

where [c.c.] represents the complex conjugate of the first term. The Hertz potential Ψ in the IRG satisfies the source-free perturbation equation for $\psi_{(s=-2)} = \rho^{-4}\psi_4$, Eq. (2.25):

$$[(\boldsymbol{\Delta} + 4\mu + \overline{\mu} + 3\gamma - \overline{\gamma})(\boldsymbol{D} - \rho) - (\overline{\boldsymbol{\delta}} + \overline{\beta} + 3\alpha - \overline{\tau} + 4\varpi)(\boldsymbol{\delta} + 4\beta - \tau) - 3\Psi_2]\rho^4\Psi = 0. \tag{3.2}$$

By using commutation relations in Appendix B.1, we obtain

$$-(\boldsymbol{\Delta} + \mu + 2\gamma)(\boldsymbol{D} + 3\rho)\Psi + 3\Psi_2\Psi + (\overline{\boldsymbol{\delta}} + 2\alpha + \varpi - \overline{\tau})(\boldsymbol{\delta} + 4\beta + 3\tau)\Psi = 0. \tag{3.3}$$

or equivalently,

$$(\boldsymbol{\Delta} - 2\mu + 2\gamma)\boldsymbol{D}\Psi + 3\rho\partial_t\Psi = (\overline{\boldsymbol{\delta}} - 2\overline{\beta} - \overline{\tau})(\boldsymbol{\delta} + 4\beta)\Psi, \tag{3.4}$$

3.2 Outgoing radiation gauge

The outgoing radiation gauge (ORG) is defined by the conditions $h_{ab}n^b = h^a{}_a = 0$. In this gauge, the perturbed metric h_{ab} is related to the Hertz potential as

$$\begin{aligned}\rho^4\Delta^2 h_{ab} = -\Bigg[&\left\{n_a n_b\frac{\overline{\rho}^2}{\rho^2}(\overline{\tilde{\boldsymbol{\delta}}} + 2\overline{\beta} + \varpi - \overline{\tau}) - m_{(a}n_{b)}\frac{\overline{\rho}}{\rho}\frac{-\Delta}{2\Sigma}(\tilde{\boldsymbol{D}} + \rho - \overline{\rho})\right\}(\overline{\tilde{\boldsymbol{\delta}}} + 4\overline{\beta} + 3\overline{\tau}) \\ &+\left\{-n_{(a}m_{b)}\frac{-\Delta}{2\Sigma}\frac{\overline{\rho}}{\rho}(\overline{\tilde{\boldsymbol{\delta}}} + 4\overline{\beta} - 2\varpi - \overline{\tau}) + m_a m_b\frac{\Delta^2}{4\Sigma^2}(\tilde{\boldsymbol{D}} - \overline{\rho})\right\}(\tilde{\boldsymbol{D}} + 3\overline{\rho})\Bigg]\Delta^2\overline{\Psi} + [\text{c.c.}]\ ,\end{aligned} \tag{3.5}$$

where $\tilde{\boldsymbol{D}}$ etc., are the auxiliary symbols which are defined in Sec. 2. The symmetry between Eqs. (3.1) and (3.5) is clear when we use them. The Hertz potential Ψ in ORG satisfies the source-free perturbation equation for $\psi_{(s=2)} = \psi_0$ (Eq. (2.26)):

$$-(\boldsymbol{D} - 4\rho - \overline{\rho})(\boldsymbol{\Delta} + \mu - 4\gamma)\Psi + 3\Psi_2\Psi + (\boldsymbol{\delta} - 2\beta - 4\tau)(\overline{\boldsymbol{\delta}} - 4\alpha + \varpi)\Psi = 0, \tag{3.6}$$

or, using the auxiliary symbols,

$$-(\tilde{\boldsymbol{\Delta}} + \mu + 2\gamma)(\tilde{\boldsymbol{D}} + 3\rho)\Delta^2\Psi + 3\Psi_2\Delta^2\Psi + (\overline{\tilde{\boldsymbol{\delta}}} + 2\alpha + \varpi - \overline{\tau})(\tilde{\boldsymbol{\delta}} + 4\beta + 3\tau)\Delta^2\Psi = 0. \tag{3.7}$$

The symmetry between Eqs. (3.3) and (3.7) is clear. Below we use the IRG. We can also obtain results in the ORG in the analogous way to the IRG case.

3.3 Relations between the Weyl scalars and the Hertz potential

In this section we present the reduced expressions for the perturbed Weyl scalars in terms of the Hertz potential in the IRG. Each expressions are obtained by calculating derivatives of

Eq. (3.5). See Appendix for detail. One can obtain ψ_0 to ψ_2 as

$$2\psi_0 = \boldsymbol{D}\boldsymbol{D}\boldsymbol{D}\boldsymbol{D}\overline{\Psi}, \tag{3.8a}$$

$$2\psi_1 = \boldsymbol{D}\boldsymbol{D}\boldsymbol{D}(\overline{\boldsymbol{\delta}} + 4\overline{\beta})\overline{\Psi} - 3\varpi\boldsymbol{D}(\boldsymbol{D} + 2\rho)\boldsymbol{D}\overline{\Psi}, \tag{3.8b}$$

$$2\psi_2 = \boldsymbol{D}\boldsymbol{D}\rho(\overline{\boldsymbol{\delta}} + 2\overline{\beta})\frac{1}{\rho}(\overline{\boldsymbol{\delta}} + 4\overline{\beta})\overline{\Psi} - 4\varpi(\boldsymbol{D} + \rho)\boldsymbol{D}(\overline{\boldsymbol{\delta}} + 4\overline{\beta})\overline{\Psi} + 6\varpi\boldsymbol{D}\varpi\boldsymbol{D}\overline{\Psi}. \tag{3.8c}$$

On the other hand, ψ_3 and ψ_4 are much more complicated. They are obtained as follows in terms of the metric perturbation $h_{\mu\nu}$:

$$\begin{aligned} 2\psi_3 = &-\boldsymbol{D}(\overline{\boldsymbol{\delta}} + \varpi - \overline{\tau})h_{22} + (\boldsymbol{\Delta} + \mu + \overline{\mu})(\boldsymbol{D} + \rho)h_{24} \\ &- 2(\overline{\tau} - \overline{\varpi})(\overline{\boldsymbol{\delta}} - 2\overline{\beta} + \varpi)h_{24} - \tau(\boldsymbol{\delta} + 2\beta + 3\overline{\tau})h_{24} - (\rho - \overline{\rho})\overline{\rho}h_{24} \\ &- 2\varpi^2 h_{23} - (\tau - 2\varpi)(\overline{\boldsymbol{\delta}} + 2\overline{\beta} + \tau)h_{23} - (2\tau + \overline{\varpi})(\boldsymbol{\Delta} + \mu - \overline{\mu})h_{44}, \end{aligned} \tag{3.9}$$

$$\begin{aligned} 2\psi_4 = &-(\overline{\boldsymbol{\delta}} + 3\alpha + \overline{\beta} - \overline{\tau})(\overline{\boldsymbol{\delta}} + 2\alpha + 2\overline{\beta} - \overline{\tau})h_{22} - (\boldsymbol{\Delta} + \mu + 2\gamma)(\boldsymbol{\Delta} + 2\mu - \overline{\mu})h_{44} \\ &+ (\boldsymbol{\Delta} + \mu + 2\gamma)(\overline{\boldsymbol{\delta}} + 2\alpha - 2\overline{\tau})h_{24} + (\overline{\boldsymbol{\delta}} + 3\alpha + \overline{\beta} - \overline{\tau})(\boldsymbol{\Delta} + 2\overline{\mu} + 2\gamma)h_{24}. \end{aligned} \tag{3.10}$$

In the Schwarzschild case, many terms vanish because $\varpi = \tau = 0$ and $\rho = \overline{\rho}$. Further, after we use Eq. (3.3) for ψ_3 and ψ_4, we obtain

$$2\psi_0 = \boldsymbol{D}\boldsymbol{D}\boldsymbol{D}\boldsymbol{D}\overline{\Psi}, \tag{3.11a}$$

$$2\psi_1 = \boldsymbol{D}\boldsymbol{D}\boldsymbol{D}(\overline{\boldsymbol{\delta}} + 4\overline{\beta})\overline{\Psi}, \tag{3.11b}$$

$$2\psi_2 = \boldsymbol{D}\boldsymbol{D}(\overline{\boldsymbol{\delta}} + 2\overline{\beta})(\overline{\boldsymbol{\delta}} + 4\overline{\beta})\overline{\Psi}, \tag{3.11c}$$

$$2\psi_3 = \boldsymbol{D}\overline{\boldsymbol{\delta}}(\overline{\boldsymbol{\delta}} + 2\overline{\beta})(\overline{\boldsymbol{\delta}} + 4\overline{\beta})\overline{\Psi} + 6\gamma\boldsymbol{D}\rho(\boldsymbol{\delta} + 4\beta)\Psi, \tag{3.11d}$$

$$2\psi_4 = (\overline{\boldsymbol{\delta}} - 2\overline{\beta})\overline{\boldsymbol{\delta}}(\overline{\boldsymbol{\delta}} + 2\overline{\beta})(\overline{\boldsymbol{\delta}} + 4\overline{\beta})\overline{\Psi} - 6\gamma\rho^2\partial_t\Psi. \tag{3.11e}$$

3.4 Summary of this chapter and discussion

By using the CCK formalism, the metric perturbation h_{ab} can be calculated from the Hertz potential. Contrary to the Regge-Wheeler-Zerilli formalism, the CCK formalism can be applied

to the Kerr metric. The Hertz potential is a complex scalar potential that satisfies the vacuum perturbation equation for $\psi_{(s=\pm 2)}$. A radiation gauge is used, and the components of h_{ab} and the perturbed Weyl scalars are expressed in terms of second order derivatives and fourth order derivatives of the Hertz potential, respectively. Then, finding the Hertz potential becomes the core of the problem of constructing the perturbed gravitational field in this method.

We can use two equations (3.8a) and (3.10) for finding the Hertz potential. Since ψ_0 and ψ_4 can be obtained by solving the Teukolsky equation, Eqs. (3.8a) and (3.10) can be regarded as two differential equations for the Hertz potential. General theory about solving these equations is discussed by Ori (2003). In the case of vacuum perturbation ($T_{ab} = 0$), the Hertz potential can be obtained as

$$\overline{\Psi} = \sum_{l,m}^{\infty} \int_{-\infty}^{\infty} \mathrm{d}\omega \overline{R^{\Psi}_{lm\omega}}(r)\, {}_2S^{a\omega}_{lm}(\theta) e^{im\phi} e^{-i\omega t}, \tag{3.12}$$

where each mode $R^{\Psi}_{lm\omega}$ is given as fourth order differential derivative of $R^{(2)}_{lm\omega}$, the radial part of ψ_0. Based on the analysis by Wald (1978), this solution is proven to be the unique solution that satisfies Eqs. (3.3), (3.8a), and (3.10). In the following chapters, we discuss the case of non-vacuum perturbation, by considering the perturbation induced by a rotating ring.

Chapter 4

Metric reconstruction

In this chapter we construct the metric perturbation in the ingoing radiation gauge for specific cases. In the method by CCK, we start from two Weyl scalars ψ_0 and ψ_4 and recover the metric perturbation, via the Hertz potential. While each Weyl scalar is second derivative of the metric, this construction method is called metric reconstruction (Ori 2003; Poisson, Pound, & Vega 2011).

As a previous work, Keidl, Friedman, & Wiseman (2007) calculated the perturbation of the Schwarzschild space-time by a particle at rest. They analytically constructed the metric perturbation in the radiation gauge and made analyses about the lower mode contribution by the Hertz potential to the space-time. This model is very special and simple. Later, they considered cases of a particle in a circular orbit around the Schwarzschild black hole and the Kerr black hole (Keidl *et al.* 2010; Shah *et al.* 2011; Shah, Friedman, & Keidl 2012). However, in these study they included the lower modes in other gauge, not in the radiation gauge. We consider obtaining the metric perturbation in the radiation gauge, for the case of a rotating ring around a black hole. The ring is circular, and is on the equatorial plane (Fig. 4.1). Since the perturbed space-time is stationary and axisymmetric, the calculation is much simpler than the orbiting particle case. However, because the ring is rotating, we can consider the both of the mass perturbation and angular momentum perturbation of the space-time in the radiation

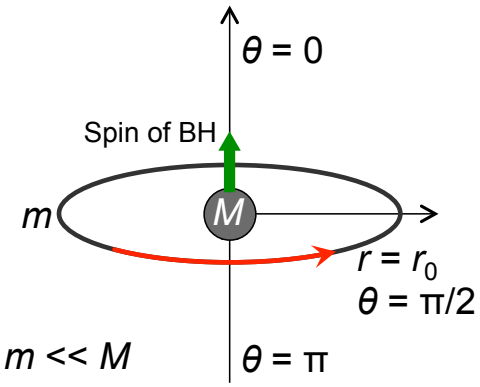

Figure 4.1: The system of a rotating ring and a black hole. The mass of the black hole is denoted by M. The mass and radius of the ring are $m \ll M$ and r_0, respectively. The ring is on the equatorial plane $\theta = \pi/2$. The perturbed space-time is stationary and axisymmetric.

gauge. We also consider the perturbation of the Kerr space-time by a particle at rest, which is the Kerr version of Keidl, Friedman, & Wiseman (2007).

4.1 Solving the Teukolsky equation

The first step is to obtain the perturbed Weyl scalars ψ_0 and ψ_4 by solving the Teukolsky equations.

4.1.1 Stationary and axisymmetric solution

Since we consider a rotating ring and a particle at rest on the axis, the energy-momentum tensor does not depend on t nor ϕ. In that case, Eq. (2.36) becomes

$$\begin{aligned} T^{(s)}_{lm\omega} &= \delta(\omega) \int_0^{\pi} \mathrm{d}\theta \int_0^{2\pi} \mathrm{d}\phi \sin\theta \; {}_sS^0_{lm} e^{-im\phi} T_{(s)} \\ &= \delta(\omega)\delta_{0m} \times T^{(s)}_l, \end{aligned} \tag{4.1}$$

where

$$\begin{aligned} T_l^{(s)} &\equiv 2\pi \int_0^\pi \mathrm{d}\theta \sin\theta \ {}_sY_l(\theta)\ T_{(s)}(r,\theta) \\ &= 2\pi \int_{-1}^1 \mathrm{d}(\cos\theta)\ {}_sY_l(\theta)\ T_{(s)}(r,\theta), \end{aligned} \tag{4.2}$$

$${}_sY_l(\theta) \equiv {}_sY_{l0}(\theta, 0). \tag{4.3}$$

Therefore the $m \neq 0$ modes and $\omega \neq 0$ modes of the Teukolsky equation are source-free equation. We solve the source-coupled modes only. It is sufficient to consider $(m, \omega) = (0, 0)$ modes. By substituting $R^{(s)}_{lm\omega} = \delta(\omega)\delta_{0m}R^{(s)}_l$ into Eq. (2.33), we have

$$\psi_{(s)} = \sum_{l=|s|}^{\infty} R_l^{(s)}(r)\ {}_sY_l(\theta). \tag{4.4}$$

The Teukolsky equation (2.34) becomes

$$\left[\frac{\mathrm{d}}{\mathrm{d}r}\left(\Delta^{s+1}\frac{\mathrm{d}}{\mathrm{d}r}\right) - \Delta^s(l-2)(l+3)\right] R_l^{(s)} = -8\pi\Delta^s T_l^{(s)}. \tag{4.5}$$

This equation can be solved using the Green's function. The Green's function is found as

$$G_l^{(s)}(r,r') = \frac{(\Delta\Delta')^{-s/2}\ P_l^2(x'_<)Q_l^2(x'_>)}{\sqrt{M^2-a^2}(l+2)(l+1)l(l-1)}, \tag{4.6}$$

where P_l^2 and Q_l^2 are the associated Legendre functions, and we define $\Delta' = r'^2 - 2Mr' + a^2$ and

$$x'_< \equiv \frac{\min(r,r') - M}{\sqrt{M^2-a^2}}, \quad x'_> \equiv \frac{\max(r,r') - M}{\sqrt{M^2-a^2}}. \tag{4.7}$$

A simple relation $(\Delta\Delta')^2 G_l^{(2)}(r,r') = G_l^{(-2)}(r,r')$ holds . The radial function $R_l^{(s)}(r)$ is obtained as

$$R_l^{(s)}(r) = \int \mathrm{d}r' \left[G_l^{(s)}(r,r')\left(8\pi\Delta'^s T_l^{(s)}(r')\right)\right]. \tag{4.8}$$

$R_l^{(2)}$ and $R_l^{(-2)}$ are the radial parts of ψ_0 and $\rho^{-4}\psi_4$, respectively. First we focus on ψ_0 ($s = 2$). After we solve ψ_0, we show that ψ_4 can be obtained from ψ_0 in the stationary and axisymmetric case.

The source term $T_l^{(s)}(r)$ is defined in Eq. (4.2). Before integrating $T_{(2)}$ to get $T_l^{(2)}(r)$, we split $T_{(2)}$ into three groups of terms in accordance with order of derivatives by $\cos\theta$:

$$T_{(2)} = T_{(2)}^{[2]} + T_{(2)}^{[1]} + T_{(2)}^{[0]}, \tag{4.9}$$

where

$$T_{(2)}^{[2]} \equiv -\frac{1}{\overline{\rho}}(\boldsymbol{\delta} - 2\beta)\frac{1}{\overline{\rho}}\boldsymbol{\delta}\frac{\overline{\rho}}{\rho}T_{11}, \tag{4.10a}$$

$$T_{(2)}^{[1]} \equiv \frac{1}{\overline{\rho}}(\boldsymbol{\delta} - 2\beta)\frac{2\tau}{\rho}T_{11} + \frac{2}{\overline{\rho}}\,(\boldsymbol{\delta} - 2\beta)\,\frac{1}{\rho}(\boldsymbol{D} - 2\rho - \overline{\rho})T_{13}, \tag{4.10b}$$

$$T_{(2)}^{[0]} \equiv \frac{2}{\rho\overline{\rho}}(\overline{\varpi} - \tau)(\boldsymbol{D} + \overline{\rho})T_{13} - \frac{1}{\rho\overline{\rho}}(\boldsymbol{D} - 4\rho - \overline{\rho})(\boldsymbol{D} - \overline{\rho})T_{33}. \tag{4.10c}$$

By integrating $T_{(2)}$ according to Eq. (4.2), $T_l^{(2)}$ is obtained. We perform partial integrations for ${T_l^{(2)}}_{[2]}$ and ${T_l^{(2)}}_{[1]}$. After that, we use Eq. (2.19):

$${T_l^{(2)}}_{[2]} = -\pi\int_{-1}^{1}\mathrm{d}(\cos\theta)\;\frac{\overline{\rho}}{\rho}T_{11}\sqrt{(l+2)(l-1)(l+1)l}\;{}_0Y_l(\theta), \tag{4.11a}$$

$${T_l^{(2)}}_{[1]} = +\sqrt{2}\pi\int_{-1}^{1}\mathrm{d}(\cos\theta)\;\frac{2}{\rho}\left[\tau T_{11} + (\boldsymbol{D} - 2\rho - \overline{\rho})T_{13}\right]\sqrt{(l+2)(l-1)}\;{}_1Y_l(\theta), \tag{4.11b}$$

$${T_l^{(2)}}_{[0]} = 2\pi\int_{-1}^{1}\mathrm{d}(\cos\theta)\;\frac{1}{\rho\overline{\rho}}\left[2(\overline{\varpi} - \tau)(\boldsymbol{D} + \overline{\rho})T_{13} - (\boldsymbol{D} - 4\rho - \overline{\rho})(\boldsymbol{D} - \overline{\rho})T_{33}\right]\;{}_2Y_l(\theta). \tag{4.11c}$$

4.1.2 Source term

We construct the energy-momentum tensor T^{ab} of a rotating circular ring and a particle at rest. The ring is composed by a set of mass particles in a circular, geodesic orbit on the equatorial plane. Both are stationary and axisymmetric. First, we show the energy-momentum tensor

for a particle:

$$\begin{aligned} T^{ab}_{\text{par.}} &= \int \mathrm{d}\tau\ u^a u^b m \delta^4(x, x_0(\tau)) \\ &= \int \mathrm{d}\tau\ u^a u^b m \frac{\delta^4(x - x_0(\tau))}{\sqrt{-g}} \\ &= \int \mathrm{d}t'\ \frac{u^a u^b}{\mathrm{d}t'/\mathrm{d}\tau} m \delta(t - t') \frac{\delta^3(x - x_0(t'))}{\sqrt{-g}} \\ &= \left[\frac{u^a u^b}{u^t}\right]_t m \frac{\delta^3(x - x_0(t))}{\sqrt{-g}}, \end{aligned} \tag{4.12}$$

where u^a and m are, respectively the four-velocity and the rest mass of the particle. The tensor field is evaluated at coordinate x $(= (t,\ r,\ \theta,\ \phi))$. The coordinate of the particle is denoted by $x_0(\tau)$, as a four-component function of the proper time τ. And $\delta^4(x, x_0)$ is the covariant Dirac distribution (delta function), g is determinant of the unperturbed Kerr metric. When we use the Boyer-Lindquist coordinates, $g = -\Sigma^2 \sin^2\theta$. Note that the four-velocity u^a is defined only at the position of the particle x_0. Next, we integrate the expression above with respect to ϕ_0 and divide it by 2π to obtain stationary and axisymmetric energy-momentum tensor for the matter at $(r_0,\ \theta_0)$:

$$\begin{aligned} T^{ab} &= \frac{1}{2\pi} \int_0^{2\pi} \mathrm{d}\phi_0 \frac{u^a u^b}{u^t} m \frac{\delta^3(x - x_0)}{\sqrt{-g}} \\ &= \frac{u^a u^b}{u^t} \frac{m}{2\pi} \frac{\delta(r - r_0)\delta(\theta - \theta_0)}{\Sigma \sin\theta} \\ &= \frac{u^a u^b}{u^t \Sigma_0} \frac{m}{2\pi} \delta(r - r_0)\delta(\cos\theta - \cos\theta_0), \end{aligned} \tag{4.13}$$

where $\Sigma_0 = {r_0}^2 + a^2 \cos^2\theta_0$. The total rest mass of the matter is m. We denote the coefficients of the delta function by $\hat{T}_{\mu\nu}$:

$$T_{ab}(e_\mu)^a (e_\nu)^b = T_{\mu\nu} = \hat{T}_{\mu\nu} \delta(r - r_0)\delta(\cos\theta - \cos\theta_0). \tag{4.14}$$

When we set $\theta_0 = \pi/2$ and $u^a = u^t((\partial_t)^a + \Omega(\partial_\phi)^a)$, T_{ab} becomes the energy-momentum tensor of a rotating mass ring on the equatorial plane. When we set $\theta_0 = 0$ and $u^a = u^t(\partial_t)^a$, T_{ab} becomes that of a mass particle at rest on the axis of symmetry. Recall that $(\partial_t)^a$ and $(\partial_\phi)^a$

are the coordinate basis vectors. The angular velocity $\Omega = \Omega(M, a, r_0)$ of the ring is fixed by the geodesic equation. The u^t is fixed by the normalization condition $u_a u^a = -1$.

We can write ${T_l^{(2)}}_{[2]}$, ${T_l^{(2)}}_{[1]}$, and ${T_l^{(2)}}_{[0]}$ as

$$ {T_l^{(2)}}_{[2]} = \pi\sqrt{(l+2)(l-1)(l+1)l}\ {}_0Y_l(\theta_0) \times \left[-\frac{\overline{\rho}}{\rho}\hat{T}_{11}\right]_{\theta_0} \delta(r-r_0), \tag{4.15a} $$

$$ {T_l^{(2)}}_{[1]} = \sqrt{2}\pi\sqrt{(l+2)(l-1)}\ {}_1Y_l(\theta_0) \times 2\left[\frac{\tau}{\rho}\hat{T}_{11} + \rho\overline{\rho}\frac{\mathrm{d}}{\mathrm{d}r}\frac{1}{\rho^2\overline{\rho}}\hat{T}_{13}\right]_{\theta_0} \delta(r-r_0), \tag{4.15b} $$

$$ {T_l^{(2)}}_{[0]} = 2\pi\ {}_2Y_l(\theta_0) \times \left[2\frac{\overline{\varpi}-\tau}{\rho\overline{\rho}^2}\frac{\mathrm{d}}{\mathrm{d}r}\overline{\rho}\hat{T}_{13} - \rho^3\frac{\mathrm{d}}{\mathrm{d}r}\frac{1}{\rho^4}\frac{\mathrm{d}}{\mathrm{d}r}\frac{1}{\overline{\rho}}\hat{T}_{33}\right]_{\theta_0} \delta(r-r_0). \tag{4.15c} $$

Here, $[\ ]_{\theta_0}$ means value at $\theta = \theta_0$. Note that the delta function $\delta(r-r_0)$ which is written at the right of $\frac{\mathrm{d}}{\mathrm{d}r}$ is differentiated by r. For example,

$$ \left[\frac{\tau}{\rho}\hat{T}_{11} + \rho\overline{\rho}\frac{\mathrm{d}}{\mathrm{d}r}\frac{1}{\rho^2\overline{\rho}}\hat{T}_{13}\right]_{\theta_0}\delta(r-r_0) = \left[\frac{\tau}{\rho}\hat{T}_{11}\delta(r-r_0) + \rho\overline{\rho}\frac{\mathrm{d}}{\mathrm{d}r}\left(\frac{1}{\rho^2\overline{\rho}}\hat{T}_{13}\delta(r-r_0)\right)\right]_{\theta_0}. \tag{4.16} $$

4.1.3 Solution

We perform integration with respect to r' to obtain $R_l^{(2)}(r)$, Eq. (4.8). Partial integration is done for terms of $\hat{T}_{13}$ and $\hat{T}_{33}$:

$$ \int \mathrm{d}r' G_l^{(2)}(r,r')\left(8\pi\Delta'^2\left[-\frac{\overline{\rho}}{\rho}\hat{T}_{11}\right]_{(r',\theta_0)}\delta(r'-r_0)\right) = 8\pi\left[-\hat{T}_{11}\frac{\overline{\rho}}{\rho}\right]_0 {\Delta_0}^2 G_l^{(2)}(r,r_0), \tag{4.17} $$

$$ \begin{aligned} &\int \mathrm{d}r' G_l^{(2)}(r,r')\left(16\pi\Delta'^2\left[\frac{\tau}{\rho}\hat{T}_{11} + \rho\overline{\rho}\frac{\mathrm{d}}{\mathrm{d}r}\frac{1}{\rho^2\overline{\rho}}\hat{T}_{13}\right]_{(r',\theta_0)}\delta(r'-r_0)\right) \\ &\quad = 16\pi\int \mathrm{d}r'\delta(r'-r_0)\left[\hat{T}_{11}\frac{\tau}{\rho} - \hat{T}_{13}\frac{1}{\rho^2\overline{\rho}}\frac{\mathrm{d}}{\mathrm{d}r}\rho\overline{\rho}\right]_{(r',\theta_0)}\Delta'^2 G_l^{(2)}(r,r') \\ &\quad = 16\pi\left[\hat{T}_{11}\frac{\tau}{\rho} - \hat{T}_{13}\frac{1}{\rho^2\overline{\rho}}\frac{\mathrm{d}}{\mathrm{d}r}\rho\overline{\rho}\right]_0 {\Delta_0}^2 G_l^{(2)}(r,r_0), \end{aligned} \tag{4.18} $$

$$ \begin{aligned} &\int \mathrm{d}r' G_l^{(2)}(r,r')\left(8\pi\Delta'^2\left[2\frac{\overline{\varpi}-\tau}{\rho\overline{\rho}^2}\frac{\mathrm{d}}{\mathrm{d}r}\overline{\rho}\hat{T}_{13} - \rho^3\frac{\mathrm{d}}{\mathrm{d}r}\frac{1}{\rho^4}\frac{\mathrm{d}}{\mathrm{d}r}\frac{1}{\overline{\rho}}\hat{T}_{33}\right]_{(r',\theta_0)}\delta(r'-r_0)\right) \\ &\quad = 8\pi\int \mathrm{d}r'\delta(r'-r_0)\left[-2\hat{T}_{13}\overline{\rho}\frac{\mathrm{d}}{\mathrm{d}r}\frac{\overline{\varpi}-\tau}{\rho\overline{\rho}^2} - \hat{T}_{33}\frac{1}{\overline{\rho}}\frac{\mathrm{d}}{\mathrm{d}r}\frac{1}{\rho^4}\frac{\mathrm{d}}{\mathrm{d}r}\rho^3\right]_{(r',\theta_0)}\Delta'^2 G_l^{(2)}(r,r') \\ &\quad = 8\pi\left[-2\hat{T}_{13}\overline{\rho}\frac{\mathrm{d}}{\mathrm{d}r}\frac{\overline{\varpi}-\tau}{\rho\overline{\rho}^2} - \hat{T}_{33}\frac{1}{\overline{\rho}}\frac{\mathrm{d}}{\mathrm{d}r}\frac{1}{\rho^4}\frac{\mathrm{d}}{\mathrm{d}r}\rho^3\right]_0 {\Delta_0}^2 G_l^{(2)}(r,r_0). \end{aligned} \tag{4.19} $$

Note that ${\Delta_0}^2 G_l^{(2)}(r, r_0)$ which is written at the right of $[\frac{\mathrm{d}}{\mathrm{d}r}]_0$ is differentiated by r_0.

As a result, the radial function $R_l^{(2)}(r)$ of the Weyl scalar ψ_0 is

$$R_l^{(2)} = {R_l^{(2)}}_{[2]} + {R_l^{(2)}}_{[1]} + {R_l^{(2)}}_{[0]}, \tag{4.20}$$

where

$${R_l^{(2)}}_{[2]} = 8\pi^2 \sqrt{(l+2)(l-1)(l+1)l}\ {}_0Y_l(\theta_0) \left[-\hat{T}_{11}\frac{\overline{\rho}}{\rho}\right]_0 {\Delta_0}^2 G_l^{(2)}(r, r_0), \tag{4.21a}$$

$${R_l^{(2)}}_{[1]} = 16\sqrt{2}\pi^2 \sqrt{(l+2)(l-1)}\ {}_1Y_l(\theta_0) \left[\hat{T}_{11}\frac{\tau}{\rho} - \hat{T}_{13}\frac{1}{\rho^2\overline{\rho}}\frac{\mathrm{d}}{\mathrm{d}r}\rho\overline{\rho}\right]_0 {\Delta_0}^2 G_l^{(2)}(r, r_0), \tag{4.21b}$$

$${R_l^{(2)}}_{[0]} = 16\pi^2\ {}_2Y_l(\theta_0) \left[-2\hat{T}_{13}\overline{\rho}\frac{\mathrm{d}}{\mathrm{d}r}\frac{\overline{\varpi} - \tau}{\rho\overline{\rho}^2} - \hat{T}_{33}\frac{1}{\overline{\rho}}\frac{\mathrm{d}}{\mathrm{d}r}\frac{1}{\rho^4}\frac{\mathrm{d}}{\mathrm{d}r}\rho^3\right]_0 {\Delta_0}^2 G_l^{(2)}(r, r_0). \tag{4.21c}$$

The Weyl scalar ψ_0 is obtained as

$$\psi_0 = \sum_{l=2}^{\infty} R_l^{(2)}(r)\ {}_2Y_l(\theta). \tag{4.22}$$

Next, we show that the Teukolsky equation with $s = -2$ can be reduced to the equation with $s = 2$. The coordinate components of the four-velocity have to satisfy $u^r = u^\theta = 0$ so that the matter distribution is stationary. Because of these conditions,

$$\frac{4\Sigma^2}{\Delta^2}T_{22} = T_{11}, \quad \frac{2\Sigma}{-\Delta}\frac{\overline{\rho}}{\rho}T_{24} = T_{13}, \quad \frac{\overline{\rho}^2}{\rho^2}T_{44} = T_{33} \tag{4.23}$$

hold. Further, because we are assuming $\partial_t T_{\mu\nu} = \partial_\phi T_{\mu\nu} = 0$, in Eqs. (2.27) and (2.29) we can replace $\tilde{\boldsymbol{D}}$ by $\boldsymbol{D}$, and so on. That means

$$[(\boldsymbol{D} - 4\rho - \overline{\rho})(\boldsymbol{\Delta} + \mu - 4\gamma) - (\boldsymbol{\delta} - 2\beta - 4\tau)(\overline{\boldsymbol{\delta}} - 4\alpha + \varpi) - 3\Psi_2]\frac{4}{\Delta^2}\psi_{(-2)} = 4\pi\frac{4}{\Delta^2}\frac{T_{(-2)}}{\Sigma}, \tag{4.24}$$

$$\begin{aligned}\frac{4}{\Delta^2}\frac{T_{(-2)}}{\Sigma} = &-(\boldsymbol{\delta} - 2\beta - 4\tau)(\boldsymbol{\delta} - \overline{\varpi})\frac{4\Sigma^2}{\Delta^2}T_{22} + (\boldsymbol{\delta} - 2\beta - 4\tau)(\boldsymbol{D} - 2\overline{\rho})\frac{2\Sigma}{-\Delta}\frac{\overline{\rho}}{\rho}T_{24} \\ &+ (\boldsymbol{D} - 4\rho - \overline{\rho})(\boldsymbol{\delta} + 2\overline{\alpha})\frac{2\Sigma}{-\Delta}\frac{\overline{\rho}}{\rho}T_{24} - (\boldsymbol{D} - 4\rho - \overline{\rho})(\boldsymbol{D} - \overline{\rho})\frac{\overline{\rho}^2}{\rho^2}T_{44}.\end{aligned} \tag{4.25}$$

The derivative operations become the same as the ones in Eqs. (2.26) and (2.28). By substituting Eq. (4.23) into Eq. (4.25), we obtain

$$\frac{4}{\Delta^2}\psi_{(-2)} = \psi_{(2)}, \tag{4.26}$$

or

$$\frac{4\rho^{-4}}{\Delta^2}\psi_4 = \psi_0. \tag{4.27}$$

Finally, because ${}_{-2}Y_l(\theta) = {}_2Y_l(\theta)$, we have

$$\frac{4}{\Delta^2}R_l^{(-2)}(r) = R_l^{(2)}(r). \tag{4.28}$$

Rotating ring

We consider the perturbation of the Kerr metric induced by a rotating ring which is composed of a set of point masses in a circular, geodesic orbit on the equatorial plane. The four-velocity is

$$u^a = u^t((\partial_t)^a + \Omega(\partial_\phi)^a), \tag{4.29}$$

where (Shah, Friedman, & Keidl 2012)

$$u^t = \frac{{r_0}^{3/2} \pm M^{1/2}a}{\sqrt{{r_0}^3 - 3M{r_0}^2 \pm 2aM^{1/2}{r_0}^{3/2}}}, \quad \Omega = \frac{\pm M^{1/2}}{{r_0}^{3/2} \pm aM^{1/2}}. \tag{4.30}$$

The upper sign is for the prograde rotation and the lower sign is for the retrograde rotation. We choose the prograde rotation below. The tetrad components u_1 and u_3 of the four-velocity are

$$u_1 = u_a l^a = u^t\left[(g_{tt} + \Omega g_{t\phi})l^t + (g_{t\phi} + \Omega g_{\phi\phi})l^\phi\right]_0 = \mathrm{Re}(u_1), \tag{4.31a}$$

$$u_3 = u_a m^a = u^t\left[(g_{tt} + \Omega g_{t\phi})m^t + (g_{t\phi} + \Omega g_{\phi\phi})m^\phi\right]_0 = i\mathrm{Im}(u_3). \tag{4.31b}$$

The constant part of the energy-momentum tensor in terms of u_1 and u_3 are as follows:

$$\hat{T}_{\mu\nu} = \frac{u_\mu u_\nu}{u^t \Sigma_0}\frac{m}{2\pi}. \tag{4.32}$$

Because $\cos\theta_0 = 0$, we have $[\rho]_0 = [\overline{\rho}]_0 = -1/r$ and thus $[\tau]_0 = [\overline{\varpi}]_0$. As a result, we obtain

$$R_l^{(2)}{}_{[2]} = 8\pi^2\sqrt{(l+2)(l-1)(l+1)l}\ {}_0Y_l(\pi/2)\left(-\hat{T}_{11}\right)\Delta_0{}^2G_l^{(2)}(r,r_0), \tag{4.33a}$$

$$R_l^{(2)}{}_{[1]} = 16\sqrt{2}\pi^2\sqrt{(l+2)(l-1)}\ {}_1Y_l(\pi/2)\left[\hat{T}_{11}\frac{ia}{\sqrt{2}r} + \hat{T}_{13}r^3\frac{\mathrm{d}}{\mathrm{d}r}\frac{1}{r^2}\right]_0\Delta_0{}^2G_l^{(2)}(r,r_0), \tag{4.33b}$$

$$R_l^{(2)}{}_{[0]} = 16\pi^2\ {}_2Y_l(\pi/2)\left[-\hat{T}_{33}r\frac{\mathrm{d}}{\mathrm{d}r}r^4\frac{\mathrm{d}}{\mathrm{d}r}\frac{1}{r^3}\right]_0\Delta_0{}^2G_l^{(2)}(r,r_0). \tag{4.33c}$$

The real and imaginary parts of $R_l^{(2)}$ are respectively

$$\mathrm{Re}(R_l^{(2)}) = R_l^{(2)}{}_{[2]} + R_l^{(2)}{}_{[0]}, \quad i\mathrm{Im}(R_l^{(2)}) = R_l^{(2)}{}_{[1]}. \tag{4.34}$$

We obtain ψ_0 and ψ_4 by Eqs. (4.22) and (4.27).

The radial dependence of ψ_0 and ψ_4 are shown in Fig. 4.2 (Sano & Tagoshi 2015). The solid lines are for the Kerr case $a = 0.99M$ and the dashed lines are for the Schwarzschild case $a = 0$. In the Schwarzschild case, because $\rho^{-1} = -r$, Eq. (4.27) becomes $(4r^4/\Delta^2)\psi_4 = \psi_0$, where $\Delta = r^2 - 2Mr$. Therefore, at a point (r,θ) such that $(4r^4/\Delta^2) \neq 0$ and $\mathrm{Re}(\psi_4) = 0$, $\mathrm{Re}(\psi_0)$ vanishes too. It is the same for $\mathrm{Im}(\psi_4)$ and $\mathrm{Im}(\psi_0)$. On the other hand, it is not the case when $a \neq 0$. In the Kerr case, because $\rho^{-1} = -(r - ia\cos\theta)$, we have

$$\frac{4}{\Delta^2}\left(\mathrm{Re}(\rho^{-4}) + i\mathrm{Im}(\rho^{-4})\right)\cdot(\mathrm{Re}(\psi_4) + i\mathrm{Im}(\psi_4)) = \mathrm{Re}(\psi_0) + \mathrm{Im}(\psi_0). \tag{4.35}$$

That is why $\mathrm{Re}(\psi_0)$ and $\mathrm{Re}(\psi_4)$ (or $\mathrm{Im}(\psi_0)$ and $\mathrm{Im}(\psi_4)$) vanish at different points in Fig. 4.2 (solid lines).

Particle at rest

We also consider the perturbed Kerr metric induced by a point mass at rest. The particle is assumed to be (unphysically) kept at $(r,\theta) = (r_0, \theta_0 = 0)$. This model is the Kerr version of Keidl, Friedman, & Wiseman (2007). The four-velocity in this case is

$$u^a = u^t(\partial_t)^a = \sqrt{\frac{\Sigma_0}{\Delta_0}}(\partial_t)^a. \tag{4.36}$$

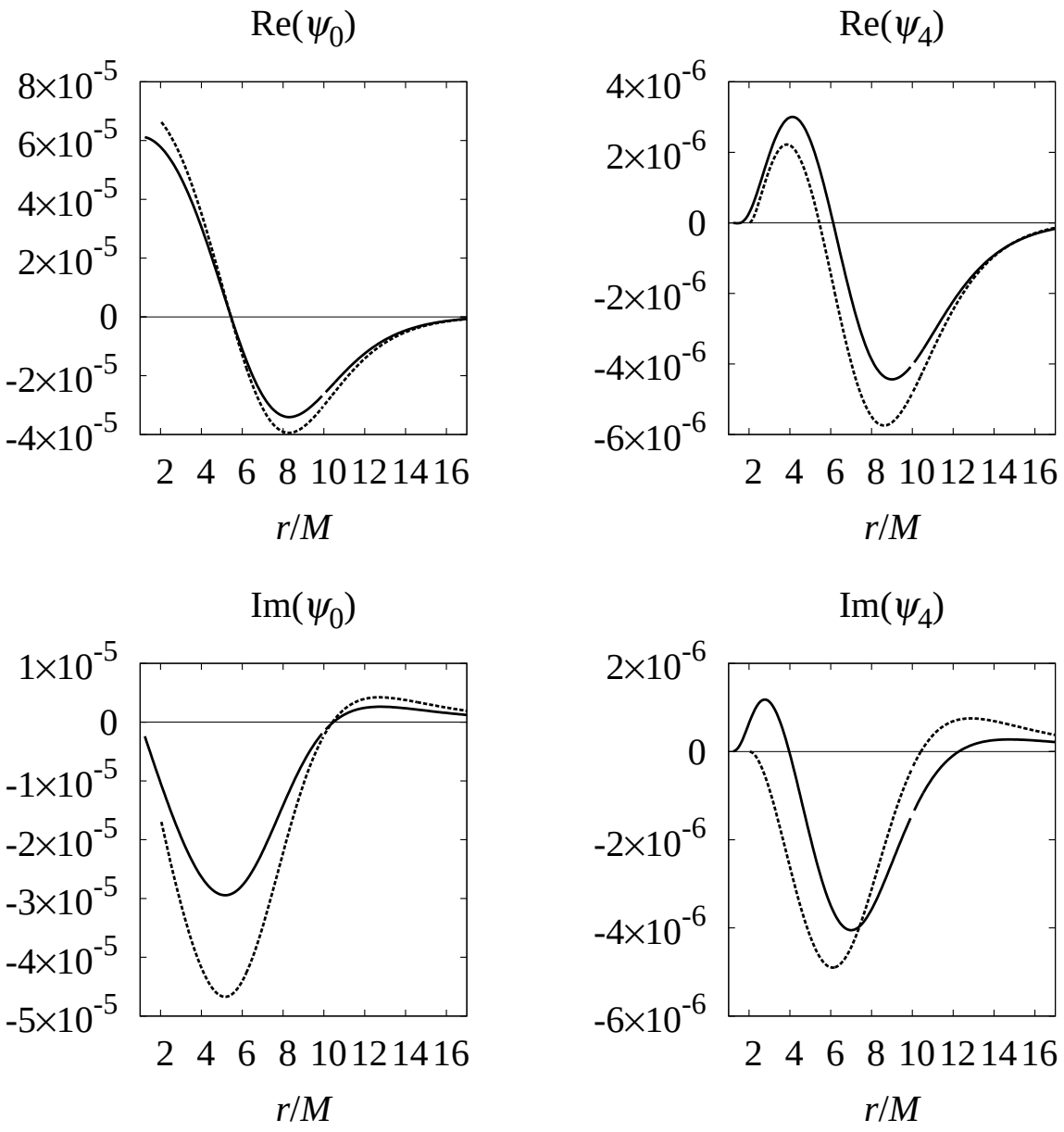

Figure 4.2: The radial dependence of the Weyl scalars ψ_0 and ψ_4, at $\theta = \pi/4$. The perturbation of the Kerr space-time by a rotating ring at $(10M, \pi/2)$ is considered. The solid line is for $a = 0.99M$, and the dashed line is for $a = 0$. The radius and the mass of the ring are $r_0 = 10M$, $m = 2\pi \times 10^{-2}M$, respectively. The event horizon is at $r = M + \sqrt{M^2 - a^2}$. The field is smooth at $r = r_0$, while the each l mode $R_l^{(\pm 2)}(r)$ is not. Reprinted figures from Y. Sano, and H. Tagoshi, (2015) (submitted).

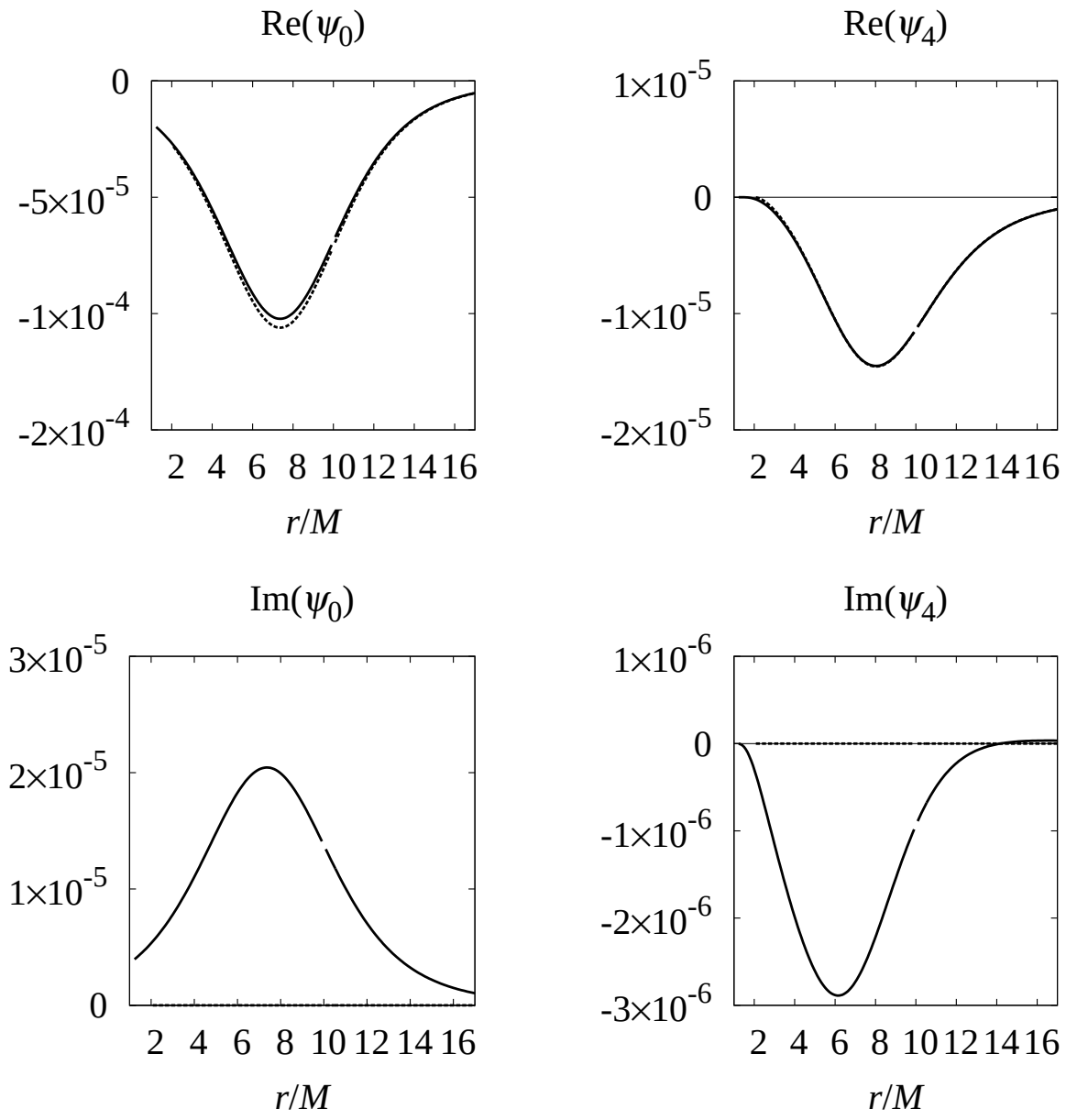

Figure 4.3: The radial dependence of the Weyl scalars ψ_0 and ψ_4, at $\theta = \pi/4$. The perturbation of the Kerr space-time by the particle at $(10M, 0)$ is considered. The solid line is for $a = 0.99M$, and the dashed line is for $a = 0$. The radius and the mass of the ring are $r_0 = 10M$, $m = 2\pi \times 10^{-2}M$, respectively. The event horizon is at $r = M + \sqrt{M^2 - a^2}$. The field is smooth at $r = r_0$, while the each l mode $R_l^{(\pm 2)}(r)$ is not. In the Schwarzschild case, $\mathrm{Im}(\psi_0) = \mathrm{Im}(\psi_4) = 0$.

Because $\sin\theta_0 = 0$, we have $[g_{t\phi}]_0 = -2Mar_0\sin^2\theta_0/\Sigma_0 = 0$, $[m^t]_0 = [-\overline{\rho}(ia\sin\theta)]_0 = 0$, and $[\varpi]_0 = [\tau]_0 = 0$. Thus the constant part of the energy-momentum tensor is

$$\hat{T}_{11} = \frac{m/(2\pi)}{\sqrt{\Delta_0\Sigma_0}}, \quad \hat{T}_{13} = \hat{T}_{33} = 0. \tag{4.37}$$

As a result, ${R_l^{(2)}}_{[1]} = {R_l^{(2)}}_{[0]} = 0$. Therefore we obtain

$$R_l^{(2)} = 8\pi^2\sqrt{(l+2)(l-1)(l+1)l}\ {}_0Y_l(0)\left(-\hat{T}_{11}\frac{{r_0}^2 - a^2 - 2ir_0a}{{r_0}^2 + a^2}{\Delta_0}^2 G_l^{(2)}(r, r_0)\right). \tag{4.38}$$

We obtain ψ_0 and ψ_4 by Eqs. (4.22) and (4.27).

The radial dependence of ψ_0 and ψ_4 are shown in Fig. 4.3. In the Schwarzschild case, $\mathrm{Im}(\psi_0) = \mathrm{Im}(\psi_4) = 0$.

4.2 Hertz potential without lower modes

The second step is to obtain the Hertz potential from the perturbed Weyl scalars ψ_0 and ψ_4, that are obtained in the previous section, Sec. 4.1. Since the Hertz potential is obtained by solving differential equations, degrees of freedom that correspond to the integral constant remain. In other words, because ψ_0 and ψ_4 are spin-weight $s = \pm 2$ quantities, they cannot specify the lower modes, $l = 0$ and $l = 1$. The Hertz potential without these lower modes is obtained in this section. The remaining part is determined in the next section, as the third step.

In the IRG (ingoing radiation gauge, Eq. (3.5)), when the perturbed space-time is stationary and axisymmetric, we have

$$\psi_0 = \frac{1}{2}\left(\frac{\partial}{\partial r}\right)^4 \overline{\Psi}, \tag{4.39}$$

$$4\rho^{-4}\psi_4 = \frac{1}{2}\sin^2\theta\left(\frac{\partial}{\partial\cos\theta}\right)^4 \sin^2\theta\overline{\Psi}, \tag{4.40}$$

where $\overline{\Psi}$ is complex conjugate of the Hertz potential Ψ. As we mentioned in Chapter 3, the Hertz potential in IRG must satisfy the source-free perturbation equation for $\psi_{(s=-2)}$. In the

case of stationary perturbed space-time, Eq. (3.4) becomes

$$\Delta^2 \frac{\partial}{\partial r}\frac{1}{\Delta}\frac{\partial}{\partial r}\overline{\Psi} + \sin^2\theta \frac{\partial}{\partial \cos\theta}\frac{1}{\sin^2\theta}\frac{\partial}{\partial \cos\theta}\sin^2\theta\overline{\Psi} = 0. \tag{4.41}$$

Our task is to find Hertz potential which satisfies Eqs. (4.39), (4.40) and (4.41). (See Sec. 4.3 for discussions about what the Hertz potential should be.) First, by substituting the solution of the Teukolsky equation ψ_4 into Eq. (4.40), we obtain

$$\sum_{l=2}^{\infty} 8R_l^{(-2)}(r)\frac{{}_{-2}Y_l(\theta)}{\sin^2\theta} = \left(\frac{\partial}{\partial \cos\theta}\right)^4 \sin^2\theta\overline{\Psi}. \tag{4.42}$$

From Eq. (2.19b), we can obtain the following relation:

$$\frac{{}_{-2}Y_l(\theta)}{\sin^2\theta} = \frac{1}{(l+2)(l-1)(l+1)l}\left(\frac{\partial}{\partial \cos\theta}\right)^4 \sin^2\theta\ {}_2Y_l(\theta). \tag{4.43}$$

By using this relation, Ψ can be integrated as

$$\overline{\Psi}(r,\theta) = \overline{\Psi_{\rm P}} + \overline{\Psi_{\rm H}}, \tag{4.44}$$

where

$$\overline{\Psi_{\rm P}} = \sum_{l=2}^{\infty}\overline{R_l^{\rm P}}(r)\ {}_2Y_l(\theta) \equiv \sum_{l=2}^{\infty}\frac{8R_l^{(-2)}(r)\ {}_2Y_l(\theta)}{(l+2)(l-1)(l+1)l}, \tag{4.45}$$

$$\overline{\Psi_{\rm H}} = \frac{2A}{\sin^2\theta}\left(\frac{a(r)}{6}\cos^3\theta + \frac{b(r)}{2}\cos^2\theta + c(r)\cos\theta + d(r)\right), \tag{4.46}$$

where A is a constant defined as $A \equiv m/(r_0\sqrt{\Delta_0})$. $\Psi_{\rm P}$ is the particular solution of the differential equations and has modes of $l \geq 2$. $\Psi_{\rm H}$ is the homogeneous solution and is what we called the remaining part in the beginning of this section.

The particular solution $\Psi_{\rm P}$ satisfies Eqs. (4.39) and (4.41) in the region $r \neq r_0$. The reason is as follows. From the Teukolsky-Starobinsky relation (Chandrasekhar 1983), we obtain

$$\left(\frac{\partial}{\partial r}\right)^4 \frac{R_l^{(-2)}(r)}{(l+2)(l-1)(l+1)l} = \frac{1}{4}R_l^{(2)}(r) \quad (r \neq r_0). \tag{4.47}$$

By using this, we can obtain ψ_0 by substituting $\Psi_{\rm P}$ into Eq. (4.39). Further, since $R_l^{(-2)}(r)$ is the solution of the radial Teukolsky equation with the source term at $r = r_0$ and ${}_2Y_l(\theta) = {}_{-2}Y_l(\theta)$,

$\overline{R^{\rm P}}(r)_2Y_l(\theta)$ satisfies the source-free perturbation equation for $\psi_{(s=-2)}$ at $r \neq r_0$. Thus, it is clear that the particular solution $\Psi_{\rm P}$ of the form Eq. (4.45) satisfies Eq. (4.41) in region $r \neq r_0$. It is now shown that $\Psi_{\rm P}$ is a Hertz potential that satisfies Eqs. (4.39), (4.40), and (4.41) everywhere except on the sphere of surface at $r = r_0$.

We discuss the regularity on $r = r_0$. The radial part $R_l^{\rm P}(r)$ of the Hertz potential $\Psi_{\rm P}$ is proportional to the radial part $R_l^{(-2)}(r)$ of the ψ_4, for each mode of l. This radial function $R_l^{(-2)}(r)$ is not smooth at $r = r_0$, that originates with the Green's function Eq. (4.6). After the l mode summation, while ψ_4 has smooth radial dependence (for $\theta \neq \pi/2$), $\Psi_{\rm P}$ does not. In fact, $\mathrm{Re}(\Psi_{\rm P})$ is continuous but not smooth, and $\mathrm{Im}(\Psi_{\rm P})$ is discontinuous, at $r = r_0$ (Fig. 4.4). This is because the radial function $\overline{R_l^{\rm P}}(r)$ is multiplied by $[(l+2)(l-1)(l+1)l]^{-1}$. If, as it was done by Keidl, Friedman, & Wiseman (2007), one could obtain $\Psi_{\rm P}$ by angular integration of the closed-form expression of $\psi_4(r,\theta)$ directly (not mode by mode), then the $\Psi_{\rm P}$ becomes smooth at $r = r_0$ because ψ_4 is so. However, we do not expect that we can find closed-form expression for ψ_4 (and ψ_0) for general cases. Thus we use $\Psi_{\rm P}$ in Eq. (4.45). The metric perturbation and the perturbed Weyl scalars derived from this $\Psi_{\rm P}$ has discontinuity on surface $r = r_0$.

The homogeneous solution $\Psi_{\rm H}$ contains four arbitrary functions of r: $a(r)$, $b(r)$, $c(r)$, and $d(r)$. In order for $\Psi_{\rm H}$ to satisfy Eq. (4.39), it is readily found that those functions have to be at most 3rd order of r. Further, $\Psi_{\rm H}$ has to satisfy Eq. (4.41). It is shown that the equation is satisfied when

$$a(r) = a_1 r^2(r - 3M) + 3a_1 a^2 r + a_2, \tag{4.48a}$$

$$b(r) = b_1(r^2 - a^2) + b_2(r - M), \tag{4.48b}$$

$$c(r) = -\frac{a_1}{2}(r^2 + 4M^2)(r - M) - \frac{a_2}{2} - \left(c_1 + \frac{a_1}{2}M\right)a^2 + c_1 r^2 + c_2(r - M), \tag{4.48c}$$

$$d(r) = \frac{b_1}{2}r^2 + \frac{b_2}{2}r + d_1(r^3 - 3Mr^2 + 3a^2 r) + d_2. \tag{4.48d}$$

Here a_1, a_2, etc. are arbitrary constants, and a is the Kerr parameter. When $a = 0$, these equations reduce to the equations in TABLE III in Keidl, Friedman, & Wiseman (2007). Since parameters a_1, a_2, b_1, ..., d_2 can be complex, the undermined degrees of freedom in $\Psi_{\rm H}$ is 16.

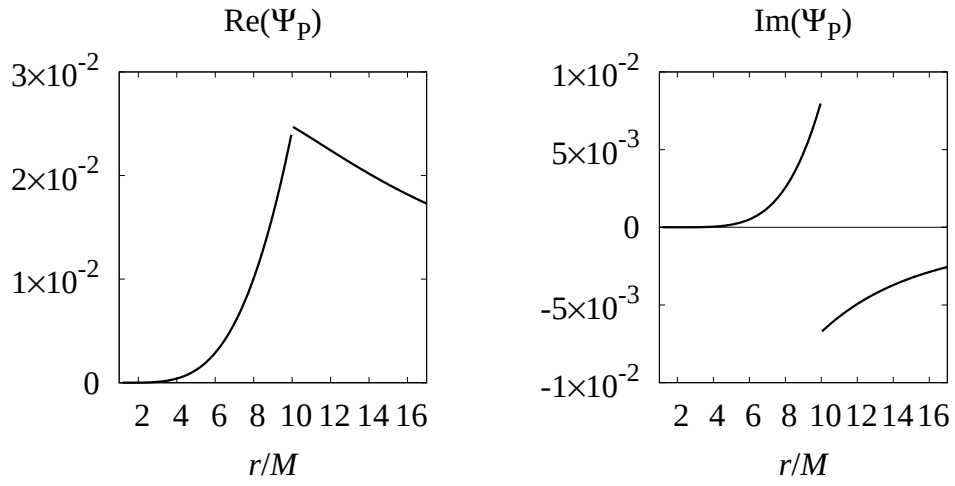

Figure 4.4: The radial dependence of the particular solution part of the Hertz potential $\Psi_{\rm P}$ obtained by Eq. (4.45). Angular coordinate is fixed at $\theta = \pi/4$. The Kerr parameter is $a = 0.99M$. The radius and the mass of the ring are $r_0 = 10M$, $m = 2\pi \times 10^{-2}M$, respectively. The event horizon is at $r = M + \sqrt{M^2 - a^2}$.

4.3 Completion of the Hertz potential

We move on to the third step. Because $\Psi_{\rm P}$ does not include $l = 0$ and $l = 1$ modes, we are motivated to complete it by adding $\Psi_{\rm H}$. The first attempt was done by Keidl, Friedman, & Wiseman (2007). In their case (Schwarzschild black hole and a particle at rest), the Weyl scalars ψ_0 and ψ_4 can be obtained as closed-form expressions. So they could obtain a particular solution $\Psi_{\rm P}$ by integrating Eq. (4.40) with respect to θ, and it can be shown that the solution satisfies Eq. (4.39). Note that their $\Psi_{\rm P}$ is not the same as Eq. (4.45), and it diverges at $\sin^2\theta = 0$. About $\Psi_{\rm H}$, they determined it by considering the finiteness of the metric perturbation on the axis $\theta = 0,\ \pi$. The resultant Hertz potential has a singularity along a radial line from the particle to infinity (Fig. 4.5) or to the horizon of the black hole.

In fact, as previously reported (Barack & Ori 2001), it is impossible to obtain globally regular solution in a radiation gauge, for non-vacuum perturbation with $T_{ab} \neq 0$. In the

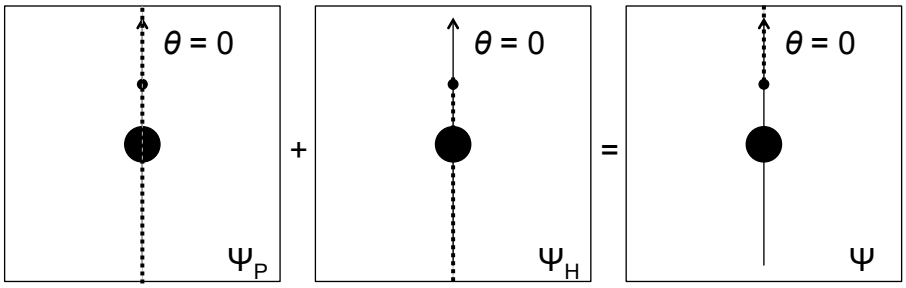

Figure 4.5: Singular regions of the Hertz potential are depicted by dotted lines. Because the system is axisymmetric, we show the slice at $\sin\phi = 0$. The vertical arrow is the axis of the symmetry. The black circle is the black hole and the small black dot is the particle at $(r = r_0, \theta = 0)$. Particular solution $\Psi_{\rm P}$ which was obtained by Keidl, Friedman, & Wiseman (2007) diverges at $\sin^2\theta = 0$. It is possible to cancel the singularity of regions $(r < r_0, \theta = 0)$ and $(\theta = \pi)$ by adding homogeneous solution $\Psi_{\rm H}$. The resultant Hertz potential $\Psi = \Psi_{\rm P} + \Psi_{\rm H}$ is singular on a line $(r > r_0, \theta = 0)$.

subsequent sections, we present solutions which are completed by $\Psi_{\rm H}$ and have a singular region. In other words, the condition of the radiation gauge breaks there. Such a gauge is called completed radiation gauge in Pound, Merlin, & Barack (2014). Despite of this inevitable singularity, the reason why we proceed with this method is as follows.

The standard method to calculate the self-force relies on the Lorenz gauge $h_{ab;c} - \frac{1}{2} g_{ab} (h_d{}^d)_{;c} = 0$. The relation between the reconstructed metric using a radiation gauge and the self-force is studied in detail by Pound, Merlin, & Barack (2014). And they found the prescription for the calculation of the self-force using the metric perturbation which is constructed in a completed radiation gauge.

4.3.1 Contribution of the remaining part of the Hertz potential

For the Schwarzschild case $a = 0$, Keidl, Friedman, & Wiseman (2007) investigated the contribution of each parameters a_1, a_2, etc. in $\Psi_{\rm H}$ to the gravitational field, using gauge transformations. They found that the metric perturbation $h^{\rm H}_{ab}$ induced by parameters except for $\mathrm{Re}(b_1)$,

$\mathrm{Re}(b_2)$, and $\mathrm{Im}(a_2)$ can be cancelled by a certain gauge transformation: $h^{\mathrm{H}}_{ab} + \mathcal{L}_\xi g^{\mathrm{Schw.}}_{ab} = 0$. Here, h^{H}_{ab} is calculated by substituting Ψ_{H} Eq. (4.46) into the CCK formula of h_{ab} Eq. (3.1) with $\mathrm{Re}(b_1) = \mathrm{Re}(b_2) = \mathrm{Im}(a_2) = 0$, and ξ^a is the gauge vector. Then we can say that the difference between h^{P}_{ab} and $h^{\mathrm{P}}_{ab} + h^{\mathrm{H}}_{ab}$ is just the choice of gauge. That means, parameters except for $\mathrm{Re}(b_1)$, $\mathrm{Re}(b_2)$, and $\mathrm{Im}(a_2)$ are not physical parameters.

On the other hand, the metric perturbation h^{H}_{ab} induced by $\mathrm{Re}(b_1)$ and $\mathrm{Re}(b_2)$ is found to be the change δM in the black hole mass M after a certain gauge transformation:

$$\begin{aligned} h^{\mathrm{H}}_{ab}(\mathrm{Re}(b_1), \mathrm{Re}(b_2)) + \mathcal{L}_\xi g_{ab} &= \frac{2\delta M}{r}(\mathrm{d}t)_a(\mathrm{d}t)_b + \left(g^{\mathrm{Schw.}}_{rr}\right)^2 \frac{2\delta M}{r}(\mathrm{d}r)_a(\mathrm{d}r)_b \\ &= \delta M \frac{\partial g^{\mathrm{Schw.}}_{ab}}{\partial M}. \end{aligned} \tag{4.49}$$

In the right-hand side, δM is given by $\mathrm{Re}(b_1)$ and $\mathrm{Re}(b_2)$. These two parameters correspond to the $l = 0$ mode perturbation. Similarly, the metric perturbation h^{H}_{ab} induced by $\mathrm{Im}(a_2)$ is found to be the first order perturbation from the Schwarzschild metric to the Kerr metric (in the Boyer-Lindquist coordinates), namely the addition of small angular momentum:

$$\begin{aligned} h^{\mathrm{H}}_{ab}(\mathrm{Im}(a_2)) + \mathcal{L}_\xi g_{ab} &= -\frac{4\delta J}{r}\sin^2\theta(\mathrm{d}t)_{(a}(\mathrm{d}\phi)_{b)} \\ &= \frac{\delta J}{M}\left[\frac{\partial g^{\mathrm{Kerr}}_{ab}}{\partial a}\right]_{a=0}, \end{aligned} \tag{4.50}$$

where $a = J/M$ is the Kerr parameter. The δJ is given by $\mathrm{Im}(a_2)$. This is the $l = 1$ mode perturbation. The specific gauge vectors of Eqs. (4.49) and (4.50) are given in Keidl, Friedman, & Wiseman (2007). (There are some typos about $\mathrm{Im}(a_2)$ in that paper. See Sano & Tagoshi (2014) for correct equations. Note that the conventions of the metric signature are different between the two papers.) After all, the contribution by the three physical parameters are found to be

$$\delta M = -A(3M\mathrm{Re}(b_1) + \mathrm{Re}(b_2)), \quad \delta J = -A\mathrm{Im}(a_2), \tag{4.51}$$

where $A = m/(r_0\sqrt{\Delta_0})$ is a fixed constant in Eq. (4.46).

4.3.2 Rotating ring

First, we consider the perturbation induced by a rotating ring around the Schwarzschild black hole ($a = 0$). In order to cancel the discontinuity of $h^{\rm P}_{ab}$ and corresponding Weyl scalars on surface of sphere at $r = r_0$, $\Psi_{\rm H}$ must not be smooth on the surface $r = r_0$. Namely, the parameters in $\Psi_{\rm H}$ have to be different values inside ($2M < r < r_0$) and outside ($r > r_0$) of the surface of sphere. The event horizon of the Schwarzschild black hole is at $r = 2M$.

Interestingly, we found that the jumps of $\mathrm{Im}(\psi_1^{\rm P})$, $\mathrm{Im}(\psi_2^{\rm P})$, and $\mathrm{Im}(\psi_3^{\rm P})$ disappear when we choose

$$\mathrm{Im}(a_2) = \begin{cases} 0, & (2M < r < r_0) \\ -\frac{J_{\rm ring}}{A}, & (r > r_0) \end{cases}, \tag{4.52}$$

using Eq. (4.51) and the angular momentum of the rotating ring $J_{\rm ring}$,

$$J_{\rm ring} = m u_a (\partial_\phi)^a = m\sqrt{\frac{M {r_0}^2}{r_0 - 3M}}. \tag{4.53}$$

Other parameters are set to be zero. Radial dependences of $\mathrm{Im}(\psi_1)$, $\mathrm{Im}(\psi_2)$, and $\mathrm{Im}(\psi_3)$ are shown in Fig. 4.6 (Sano & Tagoshi 2014). They become continuous and smooth, after adding the contribution by $\mathrm{Im}(a_2)$. We explain more about the canceling of discontinuity, by taking $\mathrm{Im}(\psi_2)$ as an example. Fig. 4.7 shows the angular dependence of the jump of $\psi_2^{\rm P}$ at $r = r_0$,

$$[\psi_2^{\rm P}]_{r_0} \equiv \lim_{r \to r_0^+} \psi_2^{\rm P}(r,\theta) - \lim_{r \to r_0^-} \psi_2^{\rm P}(r,\theta). \tag{4.54}$$

On the other hand, $\psi_2^{\rm H}$ derived from $\Psi_{\rm H}$ (Schwarzschild case) is

$$\psi_2^{\rm H} = \frac{A}{r^4}\left[(r - 3M) b_2 + 3 a_2 \cos\theta\right]. \tag{4.55}$$

Only a_2 and b_2 contribute to ψ_2. Because $\mathrm{Im}(a_2)$ is determined by Eq. (4.52) and other parameters are set to be zero, the jump of $\mathrm{Im}(\psi_2^{\rm H})$ becomes $[\mathrm{Im}(\psi_2^{\rm H})]_{r_0} = 3A\mathrm{Im}(a_2)/{r_0}^4 \cos\theta$. Therefore, this θ dependence ($\cos\theta$) perfectly match the θ dependence of $[\mathrm{Im}(\psi_2^{\rm P})]_{r_0}$ in the right panel of Fig. 4.7 (Sano & Tagoshi 2014). Both the value of the parameter and angular dependence derived from $\Psi_{\rm H}$ are important to cancel the discontinuity on the surface $r = r_0$.

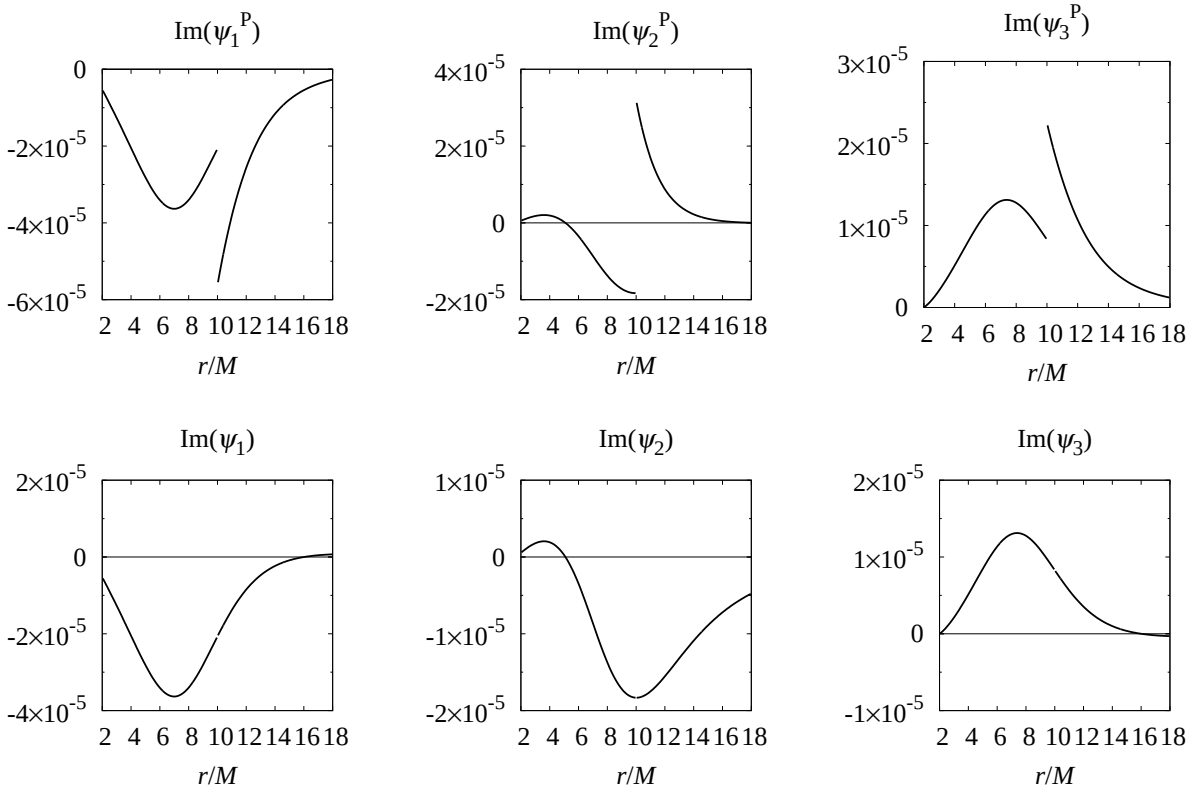

Figure 4.6: The radial dependence of the imaginary part of Weyl scalars ψ_1, ψ_2, and ψ_3, at $\theta = \pi/4$. The Kerr parameter is $a = 0$. The radius and the mass of the ring are $r_0 = 10M$, $m = 2\pi \times 10^{-2}M$, respectively. The event horizon is at $r = 2M$. The top row is for the Weyl scalars which are derived from $\Psi_{\rm P}$. All of them have jump at $r = r_0$. The bottom row is for the Weyl scalars which are derived from $\Psi_{\rm P} + \Psi_{\rm H}$, with Im($a_2$) of Eq. (4.52). Other parameters are 0. In this case, the radial dependence is smooth for any $\theta \neq \pi/2$. Reprinted figures from Y. Sano, and H. Tagoshi, Phys. Rev. D 90, 044043 (2014). Copyright (2014) by The American Physical Society.

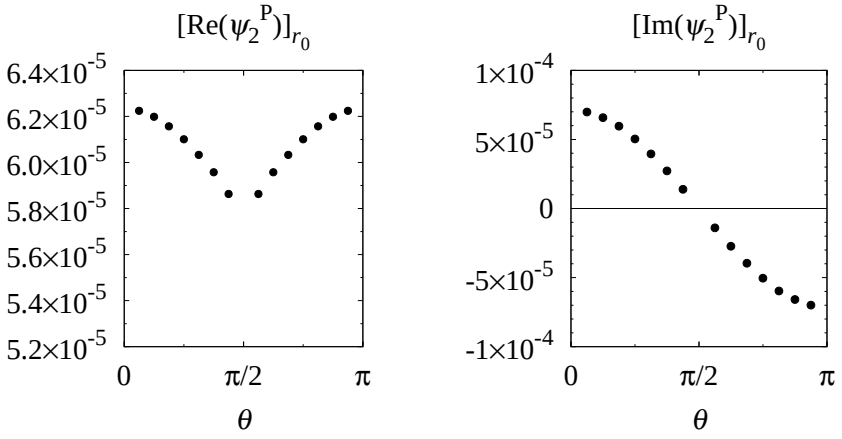

Figure 4.7: Angular dependence of the jump of $\psi_2^{\rm P}$ at $r = r_0$. The left panel is the real part and the right panel is the imaginary part of $[\psi_2^{\rm P}(r,\theta)]_{r_0}$. Reprinted figures from Y. Sano, and H. Tagoshi, Phys. Rev. D 90, 044043 (2014). Copyright (2014) by The American Physical Society.

From the result above, one might expect that the jumps of $\mathrm{Re}(\psi_1^{\rm P})$, $\mathrm{Re}(\psi_2^{\rm P})$, and $\mathrm{Re}(\psi_3^{\rm P})$ disappear when we determine $\mathrm{Re}(b_1)$ and $\mathrm{Re}(b_2)$ using Eq. (4.51) and the mass or energy of the rotating ring. However, there are two problems. The first one is the number of equations. Because we have only one equation involving $\mathrm{Re}(b_1)$ and $\mathrm{Re}(b_2)$ and mass perturbation δM, we cannot determine the two parameters. The second is the angular dependence of $[\mathrm{Re}(\psi_2^{\rm P})]_{r_0}$, which is shown in the left panel of Fig. 4.7. It is clear that this jump does not disappear by adding $\psi_2^{\rm H}$ of Eq. (4.55), unless we allow $\mathrm{Re}(a_2)$ to have different sign between in the northern half ($r > r_0, 0 \le \theta < \pi/2$) and the southern half ($r > r_0, \pi/2 < \theta \le \pi$).

Therefore, we change the strategy. We do allow the parameters to be different value between ($r > r_0, 0 \le \theta < \pi/2$) and the southern half ($r > r_0, \pi/2 < \theta \le \pi$), and determine them using the continuity conditions of gravitational fields on surface of sphere at $r = r_0$. By this method, we find that we can cancel discontinuities of all Weyl scalars, metric perturbation, and the Hertz potential. We do not use Eq. (4.51) to determine the parameters in this method. Below, we explain our method in detail. The discussion does not depend on the Kerr parameter a

anymore.

First, before we consider the continuity conditions on $r = r_0$, we obtain four conditions by demanding that the metric perturbation and the Weyl scalars should not diverge at $\theta = 0$ and $\theta = \pi$. It is achieved when the Hertz potential Ψ does not diverge on the axis. Because $\Psi_{\rm P}$ does not diverge on the axis, we demand that $\Psi_{\rm H}$ does not diverge at $\theta = 0$ and $\theta = \pi$. By the Taylor expansion of $\sin^2\theta\Psi_{\rm H}$ with respect to θ and $\pi - \theta$, respectively, we obtain the conditions for the parameters:

$$\pm c_1 = \pm M a_1 - b_1, \tag{4.56a}$$

$$\pm c_2 = \pm \left(2M^2 - \frac{3a^2}{2}\right) a_1 - b_2, \tag{4.56b}$$

$$3d_1 = \pm a_1, \tag{4.56c}$$

$$6d_2 = \pm 2a_2 - 3a^2 b_1 - 3M b_2. \tag{4.56d}$$

The upper sign is for the condition at $\theta = 0$. The lower sign is for the condition at $\theta = \pi$. These sets of conditions are simultaneously satisfied if and only if $a_1 = a_2 = b_1 = b_2 = c_1 = c_2 = d_1 = d_2 = 0$, i.e. $\Psi_{\rm H} = 0$. This means that we cannot have the contribution from the mass and the angular momentum perturbation. This also implies that we cannot obtain the regular solution globally. Then we divide the space into three regions: $(M + \sqrt{M^2 - a^2} < r < r_0)$, $(r > r_0,\ 0 \leq \theta < \pi/2)$, and $(r > r_0,\ \pi/2 < \theta \leq \pi)$. We denote each region by I, N, and S, respectively (Fig. 4.8). Following the study of determination of $\mathrm{Im}(a_2)$ above, we add $\Psi_{\rm H}$ only in N and S, i.e. $\Psi_{\rm H}(r < r_0) = 0$. We look for set of parameters that satisfy Eq. (4.56) in each of regions N and S. Since these are four equations among eight unknown parameters, the number of remaining parameters we have to determine is four.

Here, we note the symmetry of $\Psi_{\rm P}$. From Eq. (4.45), we find that, just like ψ_0 and ψ_4, the real and imaginary part of $\Psi_{\rm P}$ are symmetric and antisymmetric about the equatorial plane, respectively. In order to eliminate the jump of $\Psi_{\rm P}$ at $r = r_0$, $\Psi_{\rm H}$ at $r > r_0$ must have the same

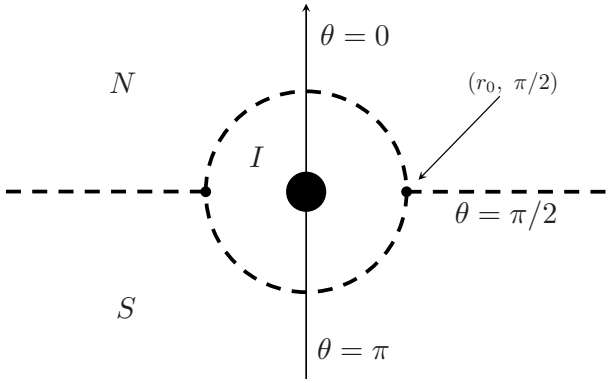

Figure 4.8: The slice at $\sin\phi = 0$ is shown. The vertical arrow is the axis of the symmetry. The three regions are divided by dashed lines. The filled black circle at the center is the region within the event horizon of the black hole. The two black dots represent the position of the ring. Reprinted figure from Y. Sano, and H. Tagoshi, Phys. Rev. D 90, 044043 (2014). Copyright (2014) by The American Physical Society.

symmetry about the equatorial plane. Therefore we get

$$\begin{aligned} a_N(r) &= -\overline{a_S}(r), \qquad b_N(r) = \overline{b_S}(r), \\ c_N(r) &= -\overline{c_S}(r), \qquad d_N(r) = \overline{d_S}(r). \end{aligned} \tag{4.57}$$

Here, $a_N(r)$ means $a(r)$ in N, and $a_S(r)$ means $a(r)$ in S, etc. Because we know this symmetry above, it is sufficient if we determine four complex parameters only in the region N or S. From Eq. (4.56), we adopt a_1, a_2, b_1 and b_2 of $\Psi_{\rm H}$ in region N as independent parameters. When the parameters satisfy Eq. (4.56), the fields corresponding to $\Psi_{\rm H}$ and $\Psi_{\rm H}$ can be written as they include only a_1, a_2, b_1 and b_2. We need four complex equations for determining these parameters. We choose the continuity conditions for ψ_1, ψ_2, h_{33}, and Ψ. The reasons are as follows: (1) The expression for ψ_3 in a radiation gauge is more complicated than others. (2) By definition, h_{22} is pure real thus gives only one equation. (3) In the Schwarzschild case, b_1 does not contribute to $h^{\rm H}_{23}$.

The continuity conditions we impose are $[F_{\rm P}(r,\theta)+F_{\rm H}(r,\theta)]_{r_0}=0$, where

$$[F(r,\theta)]_{r_0} \equiv \lim_{r\to {r_0}^+} F(r,\theta) - \lim_{r\to {r_0}^-} F(r,\theta) \tag{4.58}$$

for $F=\psi_1,\ \psi_2,\ h_{33},\ \Psi$. Because $\Psi_{\rm H}(r<r_0)=0$, the equation of continuity condition becomes

$$[F_{\rm P}(r,\theta)]_{r_0} + F_{\rm H}(r_0,\theta)=0. \tag{4.59}$$

The $[F_{\rm P}(r,\theta)]_{r_0}$ term in the each continuity condition is calculated from $\Psi_{\rm P}$. See Appendixes C and D for explicit expressions and the numerical evaluation of l mode summation, respectively. The $F_{\rm H}(r_0,\theta)$ term is analytically derived from $\Psi_{\rm H}$. Then the continuity conditions are solved simultaneously for the parameters a_1, a_2, b_1, and b_2, at an arbitrary θ. The resultant values are shown in Sec. 4.5.1. The plots of completed gravitational fields are shown in Sec. 4.4.

Fig. 4.9 shows singular regions of $\Psi_{\rm P}$, $\Psi_{\rm H}$, and $\Psi=\Psi_{\rm P}+\Psi_{\rm H}$. Because the outside region are divided into N and S, Ψ has new discontinuity surface on the equatorial plane outside the ring. Although both $\Psi_{\rm P}$ and Ψ have discontinuous regions, Ψ includes lower modes of $l=0$ and $l=1$. We discuss more about these modes in Sec. 4.5.1.

4.3.3 Particle at rest

The procedure is the same as in the ring case. The difference is how we divide the space. When the particle is on the axis $\theta=0$, we find that we can complete the Hertz potential as it has singularity at $(r>r_0, \theta=0)$. Below we explain how we divide the space.

Due to the presence of the particle on the northern axis $\theta=0$, we demand the regularity condition only of the southern axis $\theta=\pi$. Then we divide the space into two regions, I and $S=(r>r_0, 0<\theta\leq\pi)$. When we do so, we can find parameters that eliminate the discontinuities on the surface of sphere at $r=r_0$.

Fig. 4.11 shows singular regions of $\Psi_{\rm P}$, $\Psi_{\rm H}$, and $\Psi=\Psi_{\rm P}+\Psi_{\rm H}$. Compared to Fig. 4.5 (result by Keidl, Friedman, & Wiseman (2007)), $\Psi_{\rm P}$ and $\Psi_{\rm H}$ are different respectively, but the singular region of Ψ is the same. Plots of the completed gravitational field and the Hertz

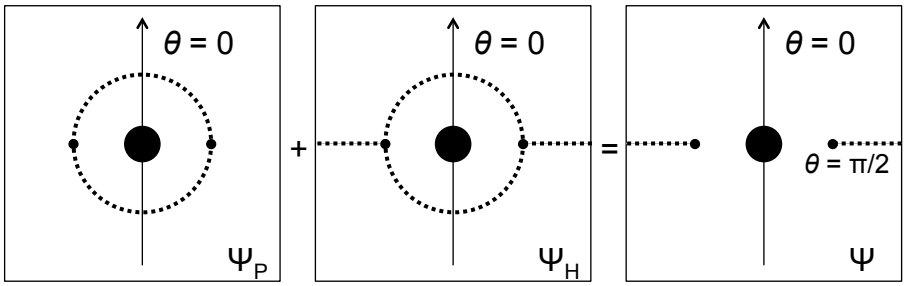

Figure 4.9: Singular regions of the Hertz potential are depicted by dotted lines. Because the system is axisymmetric, we show the slice at $\sin\phi = 0$. The vertical arrow is the axis of the symmetry. The black circle is the black hole and the small black dots represent the position of the ring $(r = r_0, \theta = \pi/2)$. Particular solution $\Psi_{\rm P}$ by Eq. (4.45) is not smooth on the surface of sphere at $r = r_0$ (dotted circle). It is possible to cancel the discontinuity by adding homogeneous solution $\Psi_{\rm H}$, which is not smooth on the surfaces $r = r_0$ and $(r > r_0, \theta = \pi/2)$. The completed Hertz potential $\Psi = \Psi_{\rm P} + \Psi_{\rm H}$ has a discontinuity on the equatorial plane outside the ring radius.

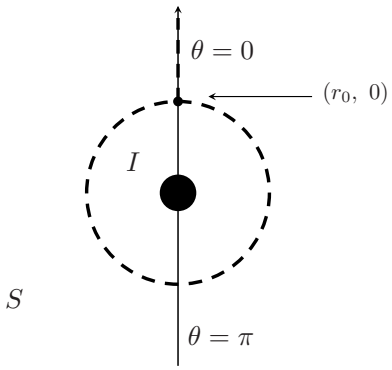

Figure 4.10: The slice at $\sin\phi = 0$ is shown. The vertical arrow is the axis of the symmetry. The two regions are divided by dashed lines. The filled black circle at the center is the region within the event horizon of the black hole. The black dot represent the position of the particle.

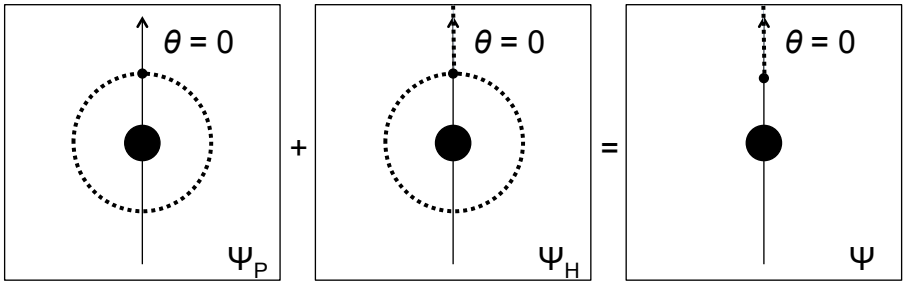

Figure 4.11: Singular regions of the Hertz potential are depicted by dotted lines. Because the system is axisymmetric, we show the slice at $\sin\phi = 0$. The vertical arrow is the axis of the symmetry. The black circle is the black hole and the small black dot is the particle at $(r = r_0, \theta = 0)$. Particular solution $\Psi_{\rm P}$ by Eq. (4.45) is not smooth on the surface of sphere at $r = r_0$ (dotted circle). It is possible to cancel the discontinuity by adding homogeneous solution $\Psi_{\rm H}$, which is not smooth on the surface $r = r_0$ and on the line $(r > r_0, \theta = 0)$. The completed Hertz potential $\Psi = \Psi_{\rm P} + \Psi_{\rm H}$ has a singular region on the axis outside the particle.

potential are shown in the next section. Radial dependences are continuous and smooth at $r = r_0$, after adding the contribution by $\Psi_{\rm H}$.

4.4 Completed gravitational fields

4.4.1 Completed Weyl tensor

The perturbed Weyl scalars for the case of a black hole and a rotating ring are shown in Fig. 4.12. The each Weyl scalar is derived from $\Psi = \Psi_{\rm P} + \Psi_{\rm H}$. The Schwarzschild case $a = 0$ and Kerr case $a = 0.99M$ are plotted for comparison.

The particle case is shown in Fig. 4.13. For the Schwarzschild case, the imaginary parts of the Weyl scalars are zero.

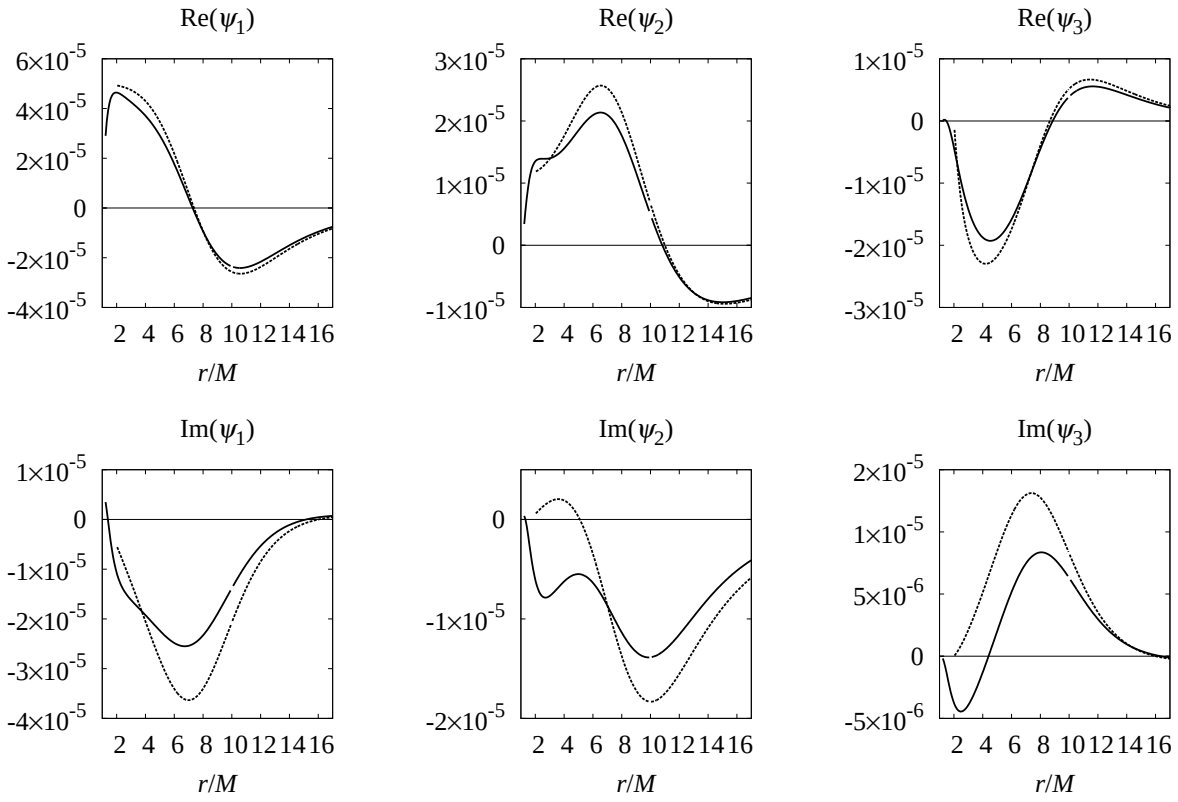

Figure 4.12: The radial dependence of the completed Weyl scalars ψ_1, ψ_2, and ψ_3, at $\theta = \pi/4$. The perturbation of the Kerr space-time by a rotating ring at $(10M, \pi/2)$ is considered. The solid line is for $a = 0.99M$, and the dashed line is for $a = 0$. The radius and the mass of the ring are $r_0 = 10M$, $m = 2\pi \times 10^{-2}M$, respectively. The event horizon is at $r = M + \sqrt{M^2 - a^2}$. All of ψ_1, ψ_2, and ψ_3 are smooth at $r = r_0$.

4.4.2 Completed metric perturbation

The completed metric perturbation which is derived from $\Psi_{\rm P} + \Psi_{\rm H}$ is shown in Fig. 4.14 for the ring case and Fig. 4.15 for the particle case. The metric perturbation h_{ab} does not vanish as $r \to \infty$ because the ingoing radiation gauge is used.

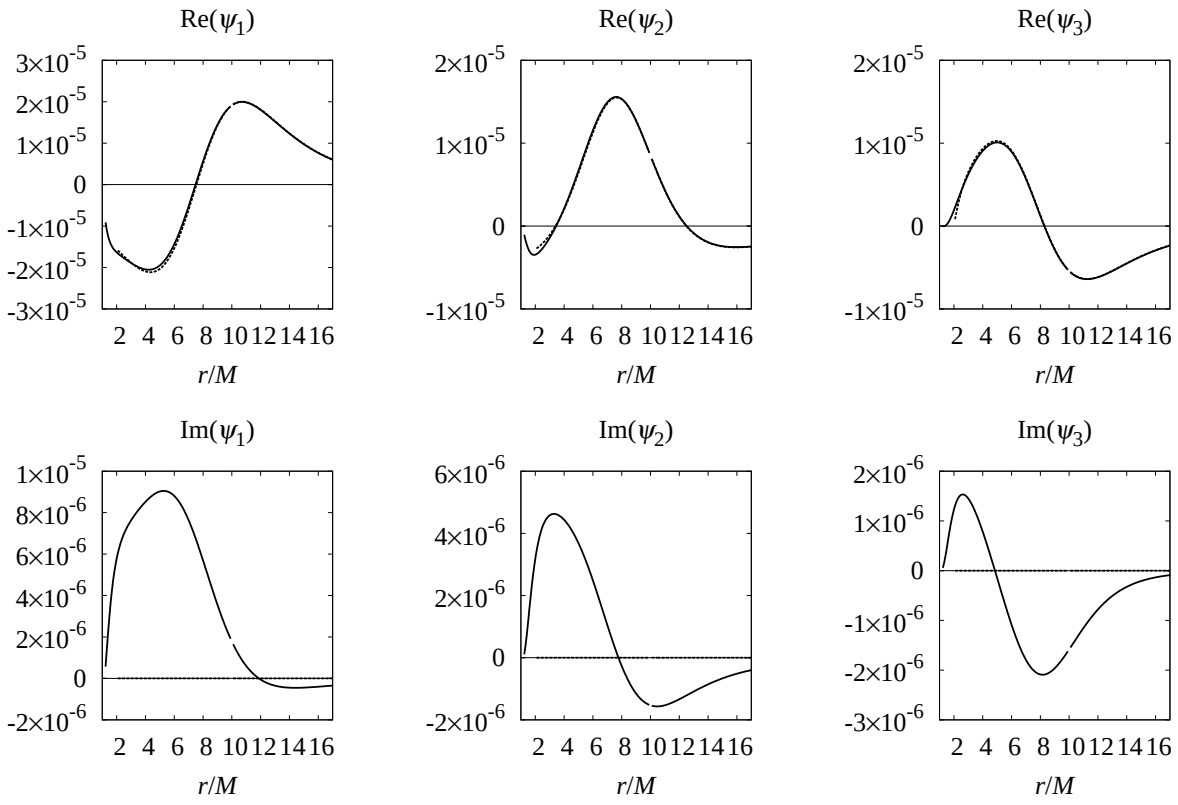

Figure 4.13: The radial dependence of the completed Weyl scalars ψ_1, ψ_2, and ψ_3, at $\theta = \pi/4$. The perturbation of the Kerr space-time by a particle at rest at $(10M, 0)$ is considered. The solid line is for $a = 0.99M$, and the dashed line is for $a = 0$. The distance and the mass of the particle is $r_0 = 10M$, $m = 10^{-2}M$, respectively. The event horizon is at $r = M + \sqrt{M^2 - a^2}$.

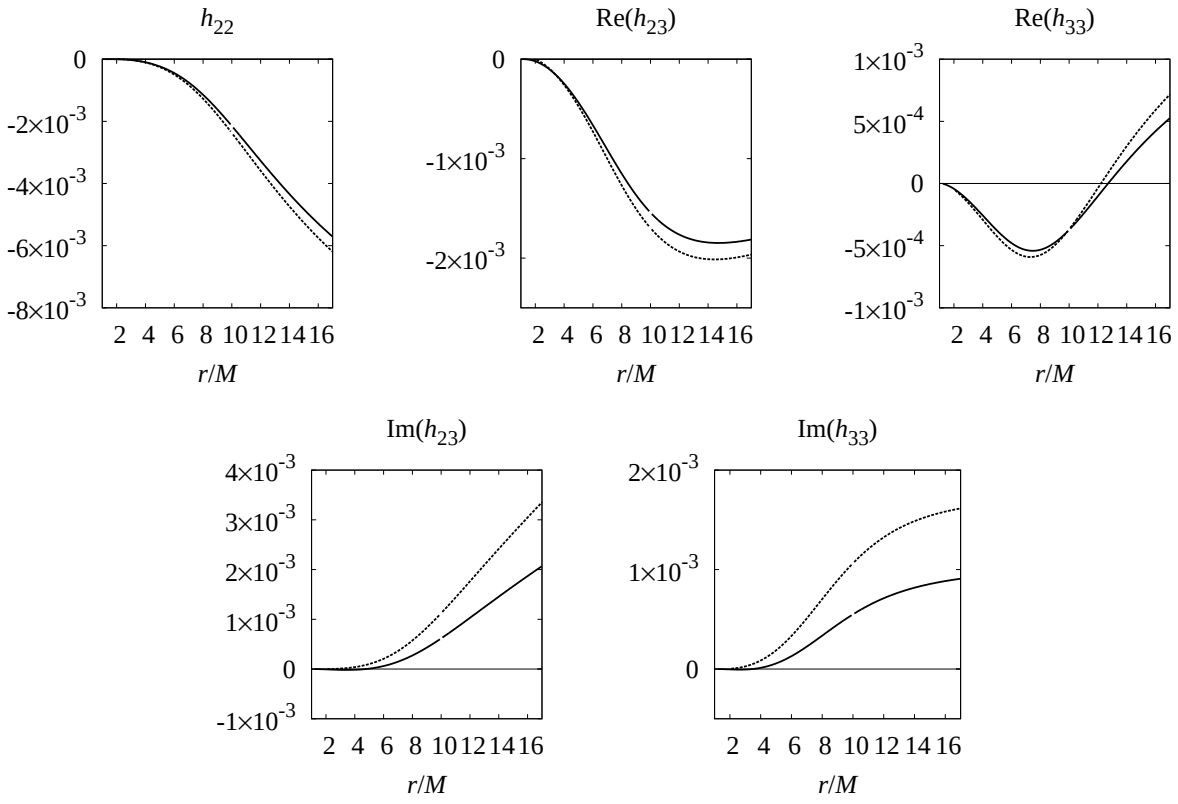

Figure 4.14: The radial dependence of the completed metric perturbation $h_{\mu\nu}$, at $\theta = \pi/4$. The perturbation of the Kerr space-time by a rotating ring at $(10M, \pi/2)$ is considered. The solid line is for $a = 0.99M$, and the dashed line is for $a = 0$. The radius and the mass of the ring are $r_0 = 10M$, $m = 2\pi \times 10^{-2}M$, respectively. The event horizon is at $r = M + \sqrt{M^2 - a^2}$. The differences by the Kerr parameter increase as r increases.

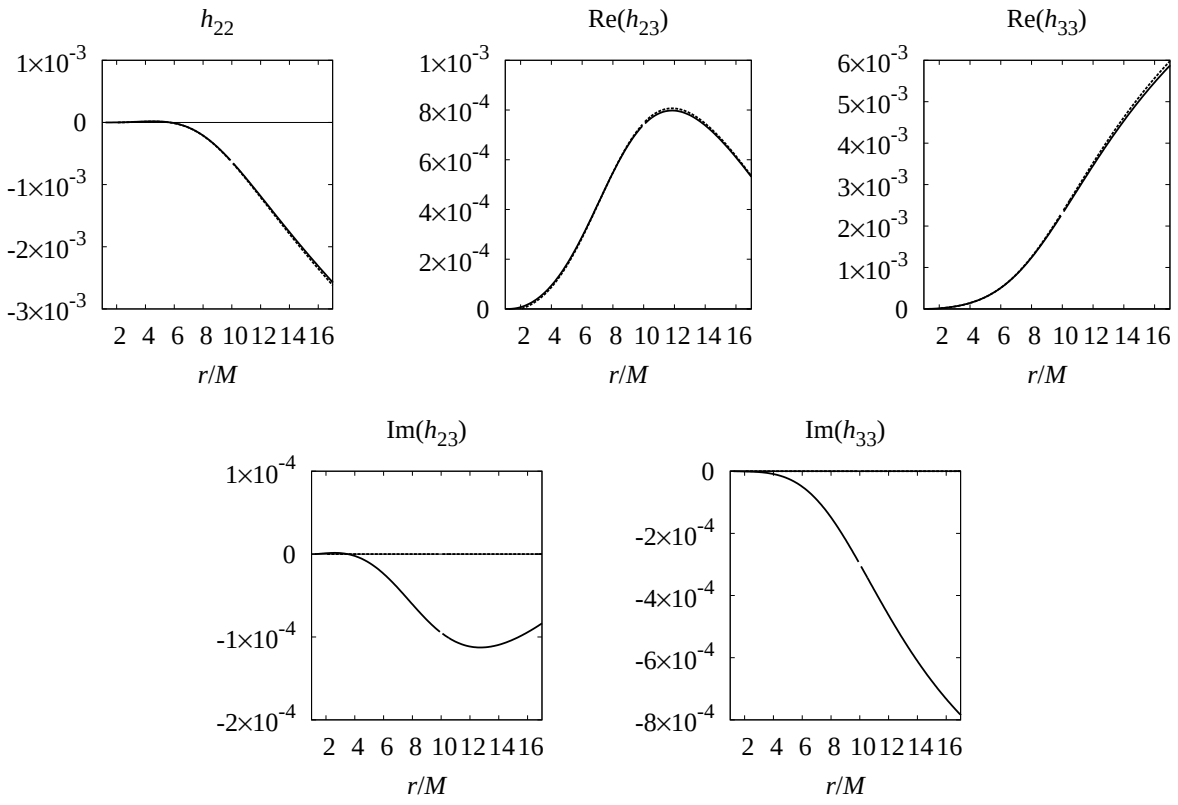

Figure 4.15: The radial dependence of the completed metric perturbation $h_{\mu\nu}$, at $\theta = \pi/4$. The perturbation of the Kerr space-time by a particle at rest at $(10M, 0)$ is considered. The solid line is for $a = 0.99M$, and the dashed line is for $a = 0$. The distance and the mass of the particle is $r_0 = 10M$, $m = 10^{-2}M$, respectively. The event horizon is at $r = M + \sqrt{M^2 - a^2}$.

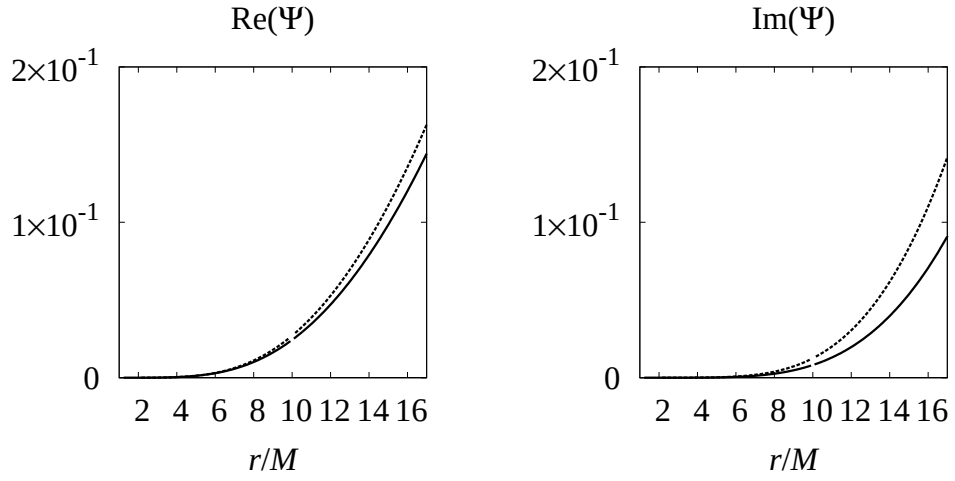

Figure 4.16: The radial dependence of the completed Hertz potential Ψ, at $\theta = \pi/4$. The perturbation of the Kerr space-time by a rotating ring at $(10M, \pi/2)$ is considered. The solid line is for $a = 0.99M$, and the dashed line is for $a = 0$. The radius and the mass of the ring are $r_0 = 10M$, $m = 2\pi \times 10^{-2}M$, respectively. The event horizon is at $r = M + \sqrt{M^2 - a^2}$.

4.4.3 Completed Hertz potential

The completed Hertz potential $\Psi = \Psi_{\rm P} + \Psi_{\rm H}$ is shown in Fig. 4.16 for the ring case and Fig. 4.17 for the particle case. For the both cases, the potential is radially monotonic and smooth.

In principle, the four parameters a_1, a_2, b_1, and b_2 can be determined using only $\Psi_{\rm P}$. Since $\psi_1^{\rm P}$, $\psi_2^{\rm P}$, and $h_{33}^{\rm P}$ are r derivatives of the Hertz potential $\Psi_{\rm P}$, the continuity conditions for them are equivalent to the condition for the differentiability of $\Psi_{\rm P}$ up to 3rd order (namely the continuity conditions for $\Psi_{\rm P}$, $\frac{\partial}{\partial r}\Psi_{\rm P}$, $\frac{\partial^2}{\partial r^2}\Psi_{\rm P}$, and $\frac{\partial^3}{\partial r^3}\Psi_{\rm P}$). However, since we already have expressions for $\psi_1^{\rm P}$, etc. in our cases, we do not expect any benefit from this alternative method.

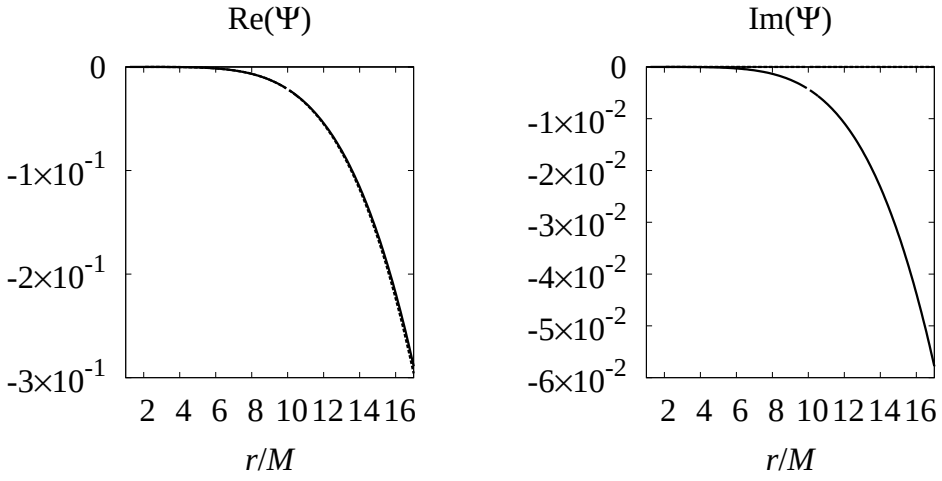

Figure 4.17: The radial dependence of the completed Hertz potential Ψ, at $\theta = \pi/4$. The perturbation of the Kerr space-time by a particle at rest at $(10M, 0)$ is considered. The solid line is for $a = 0.99M$, and the dashed line is for $a = 0$. The distance and the mass of the particle is $r_0 = 10M$, $m = 10^{-2}M$, respectively. The event horizon is at $r = M + \sqrt{M^2 - a^2}$. The imaginary part of the Hertz potential for the Schwarzschild case is $\mathrm{Im}(\Psi) = 0$.

4.5 Analyses of parameters

4.5.1 Mass and angular momentum perturbation

In the Schwarzschild case, using Eq. (4.51), we can calculate the changes in the mass and the angular momentum, δM and δJ, which are induced by physical parameters $\mathrm{Re}(b_1)$, $\mathrm{Re}(b_2)$, and $\mathrm{Im}(a_2)$. We consider the result of the perturbation by a rotating ring, and compare δM and δJ with the energy and angular momentum of the ring,

$$M_{\mathrm{ring}} \equiv -mu_a(\partial_t)^a, \quad J_{\mathrm{ring}} \equiv mu_a(\partial_\phi)^a. \tag{4.60}$$

Because of the symmetry between the regions N and S, Eq. (4.57), each of the physical parameters is constant in $(r > r_0, 0 \leq \theta \leq \pi)$.

Table 4.1: δM by a rotating ring

r_0/M	$\delta M/\mathrm{M}$	M_{ring}/M	$\lvert(M_{\mathrm{ring}} - \delta M)/M_{\mathrm{ring}}\rvert$
6	0.0592444	0.05923843916	$1.008027909 \times 10^{-4}$
10	0.0600781	0.06007874270	$1.005730101 \times 10^{-5}$
20	0.0613351	0.06133564195	$8.821135362 \times 10^{-6}$
50	0.0622144	0.06221386387	$7.995806223 \times 10^{-6}$
100	0.0625205	0.06252015946	$5.948001469 \times 10^{-6}$

Table 4.2: δJ by a rotating ring

r_0/M	$\delta J/M^2$	J_{ring}/M^2	$\lvert(J_{\mathrm{ring}} - \delta J)/J_{\mathrm{ring}}\rvert$
6	0.217649	0.2176559237	$3.301954698 \times 10^{-5}$
10	0.237451	0.2374820823	$1.308149216 \times 10^{-4}$
20	0.304774	0.3047792551	$1.758912364 \times 10^{-5}$
50	0.458263	0.4582483860	$3.190540426 \times 10^{-5}$
100	0.637962	0.6379608107	$1.972221458 \times 10^{-6}$

Interestingly, we see excellent agreement for both mass and angular momentum. It suggests the validity of our method and results. Results with various value of r_0 are shown in Tables 4.1 and 4.2 (Sano & Tagoshi 2014). This agreement is completely new result in the works for the metric reconstruction using a radiation gauge.

Now we discuss the relation between the agreement and the continuity conditions at $r = r_0$. Recall that the parameters in regions N and S are obtained using the continuity conditions, with $\Psi_{\mathrm{H}}(r < r_0) = 0$. It follows that $[\Psi_{\mathrm{H}}]_{r_0} = \Psi_{\mathrm{H}}(r_0)$. Alternatively, we can also find parameters so that they satisfy the continuity conditions with $\Psi_{\mathrm{H}}(r > r_0) = 0$. In that case, we shall divide space-time into different three regions: $N = (2M < r < r_0, 0 \leq \theta < \pi/2)$, $S = (2M < r < r_0, \pi/2 < \theta \leq \pi)$, and $O = (r > r_0)$. Then we have discontinuity on

Table 4.3: δM by a particle

r_0/M	$\delta M/\mathrm{M}$	M_{particle}/M
6	0.00714448	0.008164965809
10	0.00816313	0.008944271908

the equatorial plane inside the ring: $(2M < r < r_0, \theta = \pi/2)$. Equations for the continuity conditions are also affected. It follows that $[\Psi_{\mathrm{H}}]_{r_0} = -\Psi_{\mathrm{H}}(r_0)$ and the resultant parameters become different from the case of $\Psi_{\mathrm{H}}(r < r_0) = 0$. Though we can obtain gravitational field that is smooth at the radius of the sphere $r = r_0$, parameters $\mathrm{Re}(b_1)$ and $\mathrm{Re}(b_2)$, and $\mathrm{Im}(a_2)$ do not give the correct values of the energy and the angular momentum of the ring. They differs by the sign ($\delta M = -M_{\mathrm{ring}}$, $\delta J = -J_{\mathrm{ring}}$). Therefore, we conclude that, $\Psi_{\mathrm{H}}(r < r_0) = 0$ is the appropriate choice when we use the IRG. Probably, $\Psi_{\mathrm{H}}(r > r_0) = 0$ is appropriate when we use the ORG instead.

Next, we consider the result of the perturbation by a particle at rest. Though this is the same set-up as in Keidl, Friedman, & Wiseman (2007), The expressions for h_{23} and h_{33} are corrected in our study. Since they used these expressions for determining the parameters, we think their values of parameters are not correct. We obtain the mass perturbation induced by $\mathrm{Re}(b_1)$ and $\mathrm{Re}(b_2)$ using Eq. (4.51), and compare with the energy of the particle, $M_{\mathrm{particle}} = -mu_a(\partial_t)^a$. Results with $r_0 = 6M$ and $r_0 = 10M$ are shown in Table 4.3. Contrary to the ring case, δM and M_{particle} do not agree. It might be because the set-up is unphysical: the particle cannot be at rest in the gravitational field of the black hole.

4.6 Discussion

We discuss the singularities in the perturbed gravitational field for the ring case. The field derived from Ψ_{P} has a surface of discontinuity at $r = r_0$ and the completed field derived from

$\Psi = \Psi_{\rm P} + \Psi_{\rm H}$ has a surface of discontinuity on the plane $(r > r_0, \theta = \pi/2)$. Both have a singular region which originates from the choice of gauge. However, there are reasons why our choice of Ψ is preferred. First, the field from $\Psi_{\rm P}$ is incomplete because the mass and angular momentum perturbation are not included. As long as we include these perturbation in terms of parameters in $\Psi_{\rm H}$, we cannot avoid introducing new singular regions in the field, the axis or the equatorial plane. It is due to the (r, θ) dependence of $\Psi_{\rm H}$, Eqs. (4.46) and (4.48). It is possible to construct the field which has three singular regions at the same time: the sphere surface at $r = r_0$, the axis, and the equatorial plane. It is also possible to construct the perturbed field which has two singular regions, sphere surface and the axis or sphere surface and the equatorial plane. However, in each case of the above, the set of parameters is not uniquely determined. What we discovered here is that there is a unique choice of gauge parameters in $\Psi_{\rm H}$ so that the field has only one singular region. It is the equatorial plane outside the ring $(r > r_0, \theta = \pi/2)$.

4.7 Summary of this chapter

The Hertz potential Ψ is found using the solutions of the Teukolsky equation, ψ_0 and ψ_4, and the continuity conditions for the Weyl scalars ψ_1, ψ_2, and ψ_3, and the metric perturbation $h_{\mu\nu}$. However, it is impossible to find the globally regular Hertz potential in the case of non-vacuum perturbation $T_{ab} \neq 0$. We obtained the Hertz potential which has a singular region. In the case of a black hole and a rotating ring, it is a flat surface whose edge is at the ring. In the case of a black hole and a particle at rest, the singular region is a radial line from the particle.

By adding the homogenous solution $\Psi_{\rm H}$ of the Hertz potential, the discontinuity on the sphere surface $r = r_0$ is cancelled and the perturbations of the lower modes are included. In the case of the Schwarzschild black hole and a ring, we found an excellent agreement between δM and δJ by the numerically-determined parameters in $\Psi_{\rm H}$ and the analytical $M_{\rm ring}$ and $J_{\rm ring}$. It suggests the validity of our method and results.

Chapter 5

Visualization of space-time curvature

By using a visualization tool, it becomes possible to understand and analyze the constructed space-time more intuitively. We use tendex and vortex lines which were introduced by Nichols *et al.* (2011). According to their papers, this tool is suggested for finding new understanding of dynamics of the space-time which is obtained by numerical relativity simulations.

Dennison & Baumgarte (2012) considered approximate analytical space-time of a black hole binary. Their space-time becomes exact in the limit of small boost (velocities of black holes) or large binary separation.

On the other hand, we studied the construction of the perturbation of the black hole space-time by matter, in black hole perturbation theory. Perturbed space-time becomes exact in the limit of small mass ratio of the matter to the black hole. For the perturbed metric, we try the visualization by tendex and vortex lines. We obtain representations that are useful for understanding and explaining the construction method.

Further, we apply the visualization to the binary black hole space-time constructed by (Mundim *et al.* 2014). The metric was analytically constructed using the asymptotic matching technique.

This chapter is organized as follows. In Sec. 5.1 we introduce the visualization tool. Simple examples of the visualization are presented in Sec. 5.1.1. In Sec. 5.2 we visualize the

perturbed space-time curvature of a black hole and a particle at rest. In Sec. 5.3 we visualize the perturbed space-time curvature of a black hole and a rotating ring. In Sec. 5.4 we consider the binary black hole by Mundim *et al.* (2014).

5.1 Introduction to tendex and vortex line

We review the basics of the visualization tools (Nichols *et al.* 2011). Tidal effect and frame-drag effect of the space-time are expressed with trace-free, symmetric spatial tensors which are covariantly defined from the Weyl tensor C_{abcd}. The components of them are

$$\mathcal{E}_{ij} = C_{0i0j}, \quad \mathcal{B}_{ij} = -\frac{1}{2}\epsilon_{ipq}C_{0j}{}^{pq}, \tag{5.1}$$

where indices i, j, p, and q run over spatial components $(1, 2, 3)$. The ϵ_{ipq} is the anti-symmetric tensor. It is defined as $\epsilon_{ipq} = \epsilon_{0ipq} \equiv \sqrt{-g}[0\ i\ p\ q]$, where $[\alpha\ \beta\ \gamma\ \delta]$ equals to 1 (-1) if $\alpha\beta\gamma\delta$ is an even (odd) permutation of 0123 and vanishes otherwise. The time component (0) is along the four-velocity u^a of the observer. The space-like hypersurface is defined so that u^a is orthogonal to the surface.

The tidal field $\mathcal{E}_{ij}$ is the "electric part" of the Weyl tensor, and it represents the tidal force. Let $\Delta\xi^i$ be the infinitesimal relative position of two free-falling observers. Then the relative acceleration from each other (geodesic deviation) Δa^i is given as $\Delta a_i = -\mathcal{E}_{ij}\Delta\xi^j$. In general, there are three eigenvectors, which satisfy $\Delta a_i = -e\Delta\xi^i$, where e is the eigenvalue. Because $\mathcal{E}_{ij}$ is a symmetric tensor, these eigenvectors are orthogonal to each other. Because $\mathcal{E}_{ij}$ is trace-free, the sum of three eigenvalues is zero. The eigenvectors represent the principal directions of the tidal force. The tendex lines are field lines of the eigenvector field, which we call the tendex field. The lines are colored by blue for squeezing tidal force (positive eigenvalue) and by red for stretching tidal force (negative eigenvalue).

The frame-drag field $\mathcal{B}_{ij}$ is the "magnetic part" of the Weyl tensor, and it represents the differential frame-dragging. When there is differential frame-drag, two free-falling observers

can rotate relative to each other. To describe this, we introduce angular momentum vector σ^i for each observer. The each vector is defined not to change along the world line of the each observer. Then the relative angular velocity $\Delta\Omega_i$, namely, the change rate of difference of two angular momentum vectors is given as $\Delta\Omega_i = \mathcal{B}_{ij}\Delta\xi^j$. The eigenvectors represent directions such as $\Delta\Omega_i = b\Delta\xi^i$, where b is the eigenvalue. When the $\Delta\xi^i$ is an eigenvector, the two vectors σ^i precess with respect to ξ^i, with different angular velocities, and the direction of this resultant "twisting" effect corresponds to the sign of the eigenvalue b. Th vortex lines are field lines of the eigenvector field, which we call vortex field. The color code is the same as the tendex case: blue for positive and red for negative eigenvalue. The three eigenvectors are orthogonal to each other and the sum of the three eigenvalues is zero.

5.1.1 Rotating black hole

As a simple example, in this section we show the tendex field and vortex field of a Kerr black hole, which is considered in Appendix A of Zhang *et al.* (2012).

Here, we use the locally nonrotating frame. The orthonormal tetrad is given by

$$(e_{\hat{t}})^a = \sqrt{\frac{A}{\Sigma\Delta}}\left((\partial_t)^a + \frac{2Mar}{A}(\partial_\phi)^a\right), \tag{5.2a}$$

$$(e_{\hat{r}})^a = \sqrt{\frac{\Delta}{\Sigma}}(\partial_r)^a, \tag{5.2b}$$

$$(e_{\hat{\theta}})^a = \frac{1}{\sqrt{\Sigma}}(\partial_\theta)^a, \tag{5.2c}$$

$$(e_{\hat{\phi}})^a = \sqrt{\frac{\Sigma}{A}}\frac{1}{\sin\theta}(\partial_\phi)^a, \tag{5.2d}$$

where $A = (r^2+a^2)^2 - a^2\Delta\sin^2\theta$. The "space" is specified as the t constant hypersurface where $(e_{\hat{r}})^a$, $(e_{\hat{\theta}})^a$, and $(e_{\hat{\phi}})^a$ lie. In this basis, the tidal and frame-drag field are given by

$$\mathcal{E}_{\hat{r}\hat{r}} = \mathrm{Re}(\Psi_2)\frac{2+\xi}{1-\xi}, \qquad \mathcal{E}_{\hat{\theta}\hat{\theta}} = -\mathrm{Re}(\Psi_2)\frac{1+2\xi}{1-\xi}, \qquad \mathcal{E}_{\hat{\phi}\hat{\phi}} = -\mathrm{Re}(\Psi_2), \tag{5.3a}$$

$$\mathcal{E}_{\hat{r}\hat{\theta}} = -\mu\mathrm{Im}(\Psi_2), \qquad \mathcal{E}_{\hat{r}\hat{\phi}} = 0, \qquad \mathcal{E}_{\hat{\theta}\hat{\phi}} = 0, \tag{5.3b}$$

$$\mathcal{B}_{\hat{r}\hat{r}} = \mathrm{Im}(\Psi_2)\frac{2+\xi}{1-\xi}, \qquad \mathcal{B}_{\hat{\theta}\hat{\theta}} = -\mathrm{Im}(\Psi_2)\frac{1+2\xi}{1-\xi}, \qquad \mathcal{B}_{\hat{\phi}\hat{\phi}} = -\mathrm{Im}(\Psi_2), \tag{5.4a}$$

$$\mathcal{B}_{\hat{r}\hat{\theta}} = \mu\mathrm{Re}(\Psi_2), \qquad \mathcal{B}_{\hat{r}\hat{\phi}} = 0, \qquad \mathcal{B}_{\hat{\theta}\hat{\phi}} = 0, \tag{5.4b}$$

where

$$\xi = \frac{\Delta a^2 \sin^2\theta}{(r^2+a^2)^2}, \quad \mu = \frac{3\sqrt{\xi}}{1-\xi}, \tag{5.5}$$

and $\Psi_2 = -M/(r - ia\cos\theta)^3$ is the Weyl scalar. Note that μ in these equation is nothing to do with the spin coefficients.

In Fig. 5.1, we show tendex fields and vortex fields, for the Kerr space-time with $a = 0.99M$. On the t constant hypersurface, a Cartesian coordinate system is used: $x = r\sin\theta\cos\phi$, $y = r\sin\theta\sin\phi$, $z = r\cos\theta$. For each of tendex and vortex, there are three families of lines. The stretching red tendex lines are nearly radial from the black hole. Two families of squeezing blue tendex lines are concentric, and orthogonal to the red tendex lines. Near the event horizon, the red tendex lines acquire anisotropy. It is the effect of the spin of the black hole. On the other hand, for vortex fields, there is a symmetry about the equatorial plane, between blue (positive eigenvalue) lines and red (negative eigenvalue) vortex lines. There are two families of blue and red poloidal lines and one family of toroidal lines. This toroidal lines are blue in the northern hemisphere and red in the southern hemisphere. The intensity of color is varied in accordance with $|e|$ and $|b|$, where e and b is the tendicity and vorticity, the eigenvalues of $\mathcal{E}_{ij}$ and $\mathcal{B}_{ij}$, respectively.

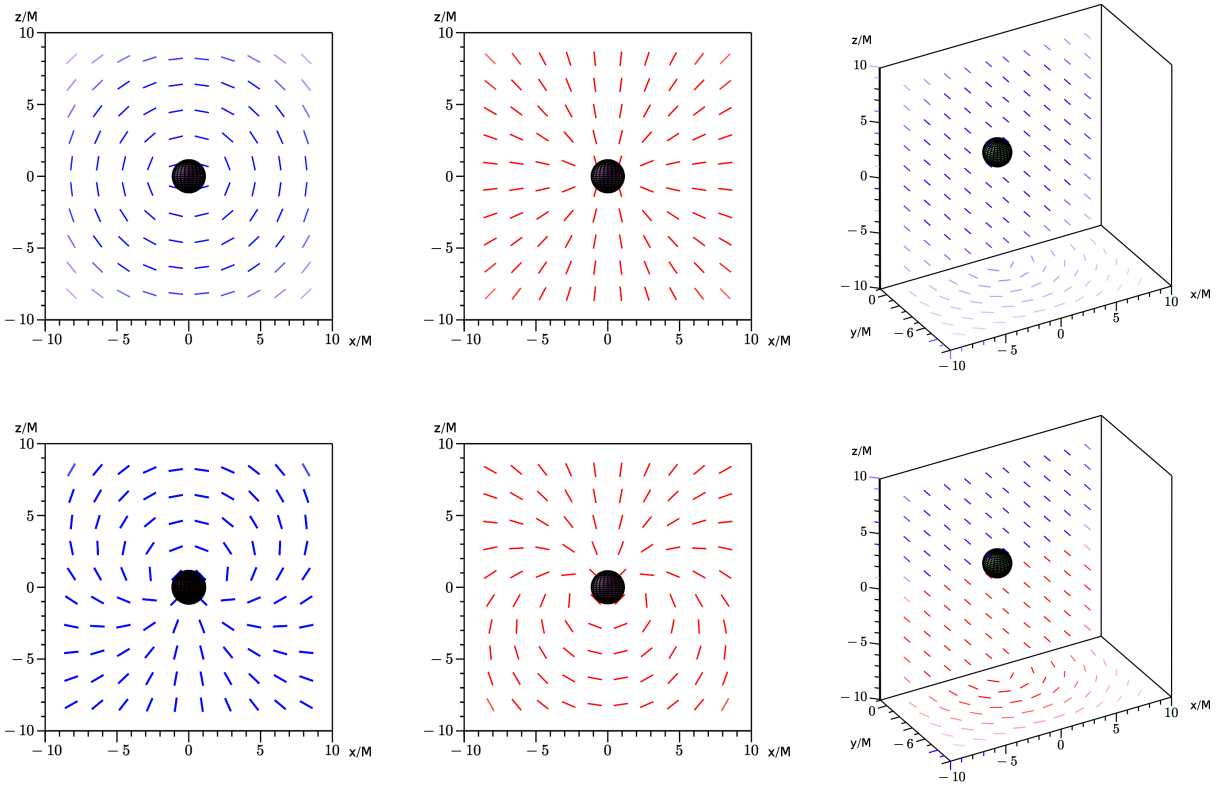

Figure 5.1: Tendex field (top row) and vortex fields (bottom row) for a Kerr space-time with $a = 0.99M$. The event horizon is the surface of sphere at $r = M + \sqrt{M^2 - a^2}$.

5.1.2 Expressions in terms of the Weyl scalars

In this section we consider the relation between the Weyl scalars and $\mathcal{E}_{ij}$, $\mathcal{B}_{ij}$. The Weyl scalars are the tetrad components of the Weyl tensor, and the tetrad is

$$(e_1)^a = l^a = \frac{r^2 + a^2}{\Delta}(\partial_t)^a + (\partial_r)^a + \frac{a}{\Delta}(\partial_\phi)^a, \tag{5.6a}$$

$$(e_2)^a = n^a = \frac{\Delta}{2\Sigma}\left[\frac{r^2 + a^2}{\Delta}(\partial_t)^a - (\partial_r)^a + \frac{a}{\Delta}(\partial_\phi)^a\right], \tag{5.6b}$$

$$(e_3)^a = m^a = \frac{-\overline{\rho}}{\sqrt{2}}\left[ia\sin\theta(\partial_t)^a + (\partial_\theta)^a + i\csc\theta(\partial_\phi)^a\right], \tag{5.6c}$$

$$(e_4)^a = \overline{m}^a = \frac{-\rho}{\sqrt{2}}\left[-ia\sin\theta(\partial_t)^a + (\partial_\theta)^a - i\csc\theta(\partial_\phi)^a\right]. \tag{5.6d}$$

We use a local Lorenz frame. We take the following orthonormal basis:

$$(e_{\hat{t}})^a = \frac{r^2+a^2}{\sqrt{\Delta\Sigma}}(\partial_t)^a + \frac{a}{\sqrt{\Delta\Sigma}}(\partial_\phi)^a, \tag{5.7a}$$

$$(e_{\hat{r}})^a = \sqrt{\frac{\Delta}{\Sigma}}(\partial_r)^a, \tag{5.7b}$$

$$(e_{\hat{\theta}})^a = \frac{1}{\sqrt{\Sigma}}(\partial_\theta)^a, \tag{5.7c}$$

$$(e_{\hat{\phi}})^a = \frac{a\sin\theta}{\sqrt{\Sigma}}(\partial_t)^a + \frac{\csc\theta}{\sqrt{\Sigma}}(\partial_\phi)^a. \tag{5.7d}$$

The reason why we take this basis is the simplicity that we see below. We consider the transformation from the component by the tetrad $(e_\mu)^a$ to the component by the orthonormal basis $(e_{\hat{\alpha}})^a$. In the case of a dual vector A_a, for instance, the transformation from A_μ to $A_{\hat{\alpha}}$ is written as

$$A_{\hat{\alpha}} = A_\mu (e^\mu)_a (e_{\hat{\alpha}})^a \equiv \frac{1}{\sqrt{2}} A_\mu \Lambda^\mu{}_{\hat{\alpha}}, \tag{5.8}$$

where $(e^\mu)_a$ $(\mu = 1, 2, 3, 4)$ is the dual basis for $(e_\mu)^a$:

$$(e^1)_a = -n^a, \quad (e^2)_a = -l^a, \quad (e^3)_a = \overline{m}^a, \quad (e^4)_a = m^a. \tag{5.9}$$

By choosing the basis as Eq. (5.7), $\Lambda^\mu{}_{\hat{\alpha}}$ becomes simple. The nonzero components are

$$\Lambda^1{}_{\hat{t}} = \sqrt{\frac{\Delta}{2\Sigma}}, \quad \Lambda^1{}_{\hat{r}} = \sqrt{\frac{\Delta}{2\Sigma}}, \quad \Lambda^2{}_{\hat{t}} = \sqrt{\frac{2\Sigma}{\Delta}}, \quad \Lambda^2{}_{\hat{r}} = -\sqrt{\frac{2\Sigma}{\Delta}}, \tag{5.10}$$

$$\Lambda^3{}_{\hat{\theta}} = -\rho\sqrt{\Sigma}, \quad \Lambda^3{}_{\hat{\phi}} = i\rho\sqrt{\Sigma}, \quad \Lambda^4{}_{\hat{\theta}} = -\overline{\rho}\sqrt{\Sigma}, \quad \Lambda^4{}_{\hat{\phi}} = -i\overline{\rho}\sqrt{\Sigma}. \tag{5.11}$$

Note $\Lambda^3{}_{\hat{\theta}}\Lambda^4{}_{\hat{\theta}} = 1$, and so on.

By performing this transformation, the components of tidal field tensor are obtained as

follows:

$$\mathcal{E}_{\hat{r}\hat{r}} = 2\mathrm{Re}(\Psi_2), \tag{5.12a}$$

$$\mathcal{E}_{\hat{\theta}\hat{\theta}} = \frac{1}{2}\left(\frac{\Delta}{2}\mathrm{Re}(\rho^2\Psi_0) - 2\mathrm{Re}(\Psi_2) + \frac{2}{\Delta}\mathrm{Re}(\rho^{-2}\Psi_4)\right), \tag{5.12b}$$

$$\mathcal{E}_{\hat{\phi}\hat{\phi}} = \frac{1}{2}\left(-\frac{\Delta}{2}\mathrm{Re}(\rho^2\Psi_0) - 2\mathrm{Re}(\Psi_2) - \frac{2}{\Delta}\mathrm{Re}(\rho^{-2}\Psi_4)\right), \tag{5.12c}$$

$$\mathcal{E}_{\hat{r}\hat{\theta}} = \sqrt{\frac{\Delta}{2}}\mathrm{Re}(\rho\Psi_1) - \sqrt{\frac{2}{\Delta}}\mathrm{Re}(\rho^{-1}\Psi_3), \tag{5.12d}$$

$$\mathcal{E}_{\hat{r}\hat{\phi}} = \sqrt{\frac{\Delta}{2}}\mathrm{Im}(\rho\Psi_1) + \sqrt{\frac{2}{\Delta}}\mathrm{Im}(\rho^{-1}\Psi_3), \tag{5.12e}$$

$$\mathcal{E}_{\hat{\theta}\hat{\phi}} = \frac{1}{2}\left(\frac{\Delta}{2}\mathrm{Im}(\rho^2\Psi_0) - \frac{2}{\Delta}\mathrm{Im}(\rho^{-2}\Psi_4)\right). \tag{5.12f}$$

Since the basis vectors are orthonormal, we can treat this tensor as a matrix. Then the trace-free condition is written as $\mathcal{E}_{\hat{r}\hat{r}} + \mathcal{E}_{\hat{\theta}\hat{\theta}} + \mathcal{E}_{\hat{\phi}\hat{\phi}} = 0$. In a similar manner, the components of the frame-drag field tensor are obtained:

$$\mathcal{B}_{\hat{r}\hat{r}} = 2\mathrm{Im}(\Psi_2), \tag{5.13a}$$

$$\mathcal{B}_{\hat{\theta}\hat{\theta}} = \frac{1}{2}\left(\frac{\Delta}{2}\mathrm{Im}(\rho^2\Psi_0) - 2\mathrm{Im}(\Psi_2) + \frac{2}{\Delta}\mathrm{Im}(\rho^{-2}\Psi_4)\right), \tag{5.13b}$$

$$\mathcal{B}_{\hat{\phi}\hat{\phi}} = \frac{1}{2}\left(-\frac{\Delta}{2}\mathrm{Im}(\rho^2\Psi_0) - 2\mathrm{Im}(\Psi_2) - \frac{2}{\Delta}\mathrm{Im}(\rho^{-2}\Psi_4)\right), \tag{5.13c}$$

$$\mathcal{B}_{\hat{r}\hat{\theta}} = \sqrt{\frac{\Delta}{2}}\mathrm{Im}(\rho\Psi_1) - \sqrt{\frac{2}{\Delta}}\mathrm{Im}(\rho^{-1}\Psi_3), \tag{5.13d}$$

$$\mathcal{B}_{\hat{r}\hat{\phi}} = -\sqrt{\frac{\Delta}{2}}\mathrm{Re}(\rho\Psi_1) - \sqrt{\frac{2}{\Delta}}\mathrm{Re}(\rho^{-1}\Psi_3), \tag{5.13e}$$

$$\mathcal{B}_{\hat{\theta}\hat{\phi}} = -\frac{1}{2}\left(\frac{\Delta}{2}\mathrm{Re}(\rho^2\Psi_0) - \frac{2}{\Delta}\mathrm{Re}(\rho^{-2}\Psi_4)\right). \tag{5.13f}$$

Thus, from the Weyl scalars we can calculate the tidal field $\mathcal{E}_{\hat{i}\hat{j}}$ and the frame-drag field $\mathcal{B}_{\hat{i}\hat{j}}$ in the local Lorenz frame.

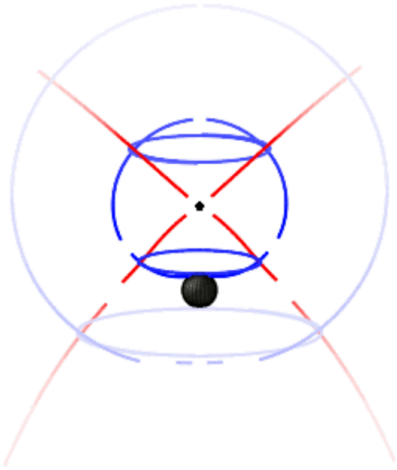

Figure 5.2: Squeezing (blue) and stretching (red) tendex lines for the perturbation by a particle at rest around the Schwarzschild black hole. Note that field for the unperturbed Schwarzschild metric is subtracted. Due to the cost of numerical computation, the regions near the surface $r = r_0$ and the axis $\theta = 0,\ \pi$ is omitted.

5.2 Black hole and a particle at rest

In this section we consider the perturbed gravitational field induced by a particle at rest on the z axis, in a black hole space-time (Sec 4.3.3). First, the tendex lines for the Schwarzschild case are displayed in Fig. 5.2. Only the perturbed part of the tidal field is used. The lines represent the tidal field by the particle at $(r_0 = 10M, \theta_0 = 0)$. The stretching red tendex lines are drawn radially from the particle. We see the red lines slightly bend, which is supposed to be the effect of the Schwarzschild background. There are two squeezing blue tendex lines orthogonal to the red line at each point of space. One is toroidal, circular lines. The other is poloidal, nearly circular lines on the ϕ-constant plane.

Next, we consider the vortex lines. We expect no frame-drag effect in the case of the

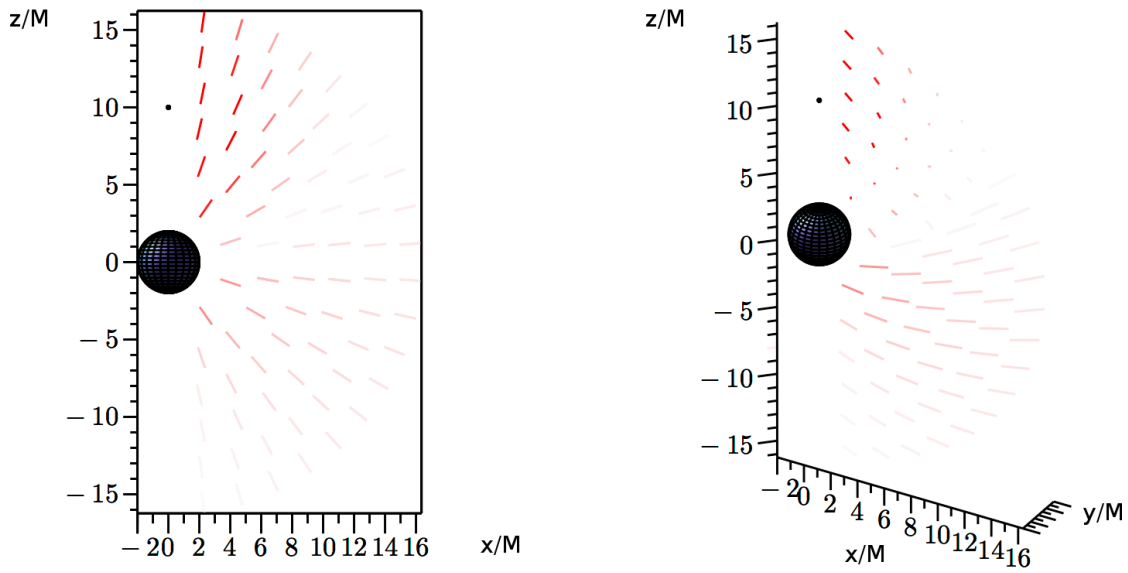

Figure 5.3: Red (negative eigenvalue) vortex field on the plane $(2M < r < 2(r_0 - 2M), 0 < \theta < \pi, \phi = 0)$ for the perturbation by a particle at rest around the Schwarzschild black hole. The left and right panel differs by the viewpoint.

Schwarzschild black hole and a particle at rest. From the fact that the imaginary part of all the Weyl scalars vanish in the Schwarzschild case, non-vanishing elements of the frame-drag field $\mathcal{B}_{\hat{i}\hat{j}}$ are $\mathcal{B}_{\hat{r}\hat{\phi}} = \mathcal{B}_{\hat{\phi}\hat{r}}$. Then the three eigenvalues are $b_0 = 0$ and $b_\pm = \pm\mathcal{B}_{\hat{r}\hat{\phi}}$, and the eigenvectors $\xi^{\hat{i}}_\pm$ for $\lambda_\pm$ are vectors such as $\xi^{\hat{r}}_\pm = \pm\xi^{\hat{\phi}}_\pm$. The vector field of $\xi^{\hat{i}}_-$ on plane $(2M < r < 2(r_0 - 2M), 0 < \theta < \pi, \phi = 0)$ is shown in Fig. 5.3. Note that the each vector (short line in the figure) has ϕ component, which is perpendicular to the plane. The magnitude of the eigenvalue is larger near the north pole $\theta = 0$ than other region. The vector field of $\xi^{\hat{i}}_+$ (blue vortex) is obtained by reversing $\phi \to -\phi$. The interpretation of these vortex fields is not clear. The possible reasons why such vortex fields appear are as follows: (1) The set-up is unphysical. A particle cannot be at rest in the gravitational field of the black hole. (2) The choice of space-like hypersurface is not good. The vortex field might qualitatively change when

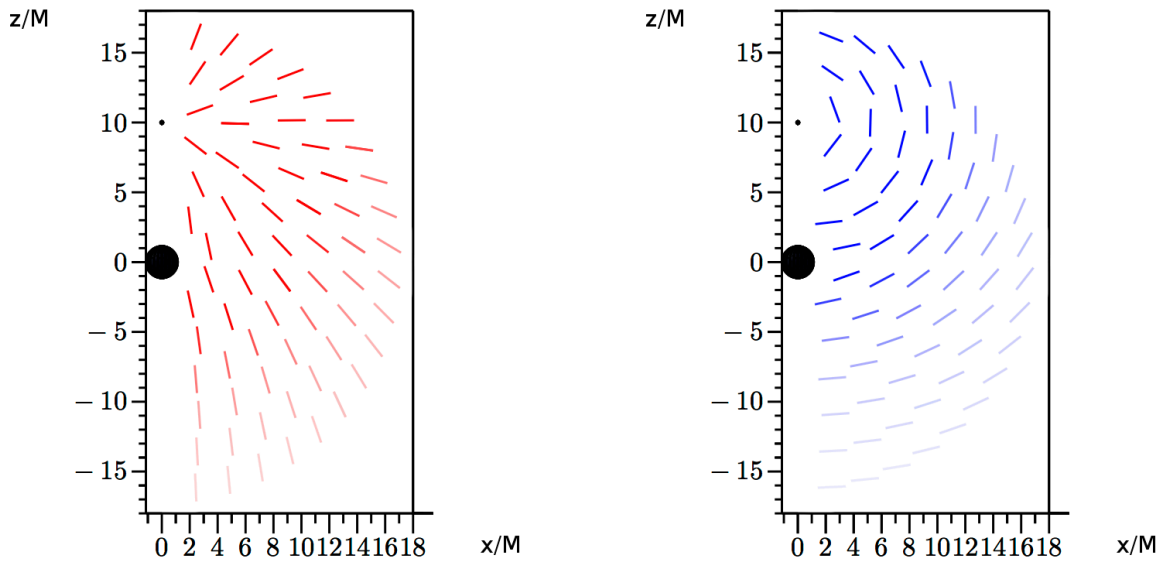

Figure 5.4: Tendex fields for perturbation by a particle at rest around the Kerr black hole ($a = 0.99M$). $\phi = 0$ plane (x-z plane) is shown. Left panel: Stretching red tendex field. Right panel: Squeezing blue tendex field.

we choose the hypersurface using Eq. (5.2). Investigating this problem is a future work.

The tendex field for the Kerr case is shown in Fig. 5.4. As in the Schwarzschild case, stretching red tendex lines are radial from the particle, and there are two families of blue tendex lines, which are orthogonal to the red lines. Fig. 5.4 shows two poloidal tendex fields on a ϕ constant plane.

5.3 Black hole and a rotating ring

In this section we consider the perturbed gravitational field induced by a rotating ring on the equatorial plane, in a black hole space-time (Sec 4.3.2).

First, we show the tendex and vortex lines for the Schwarzschild case in Fig. 5.5. There are

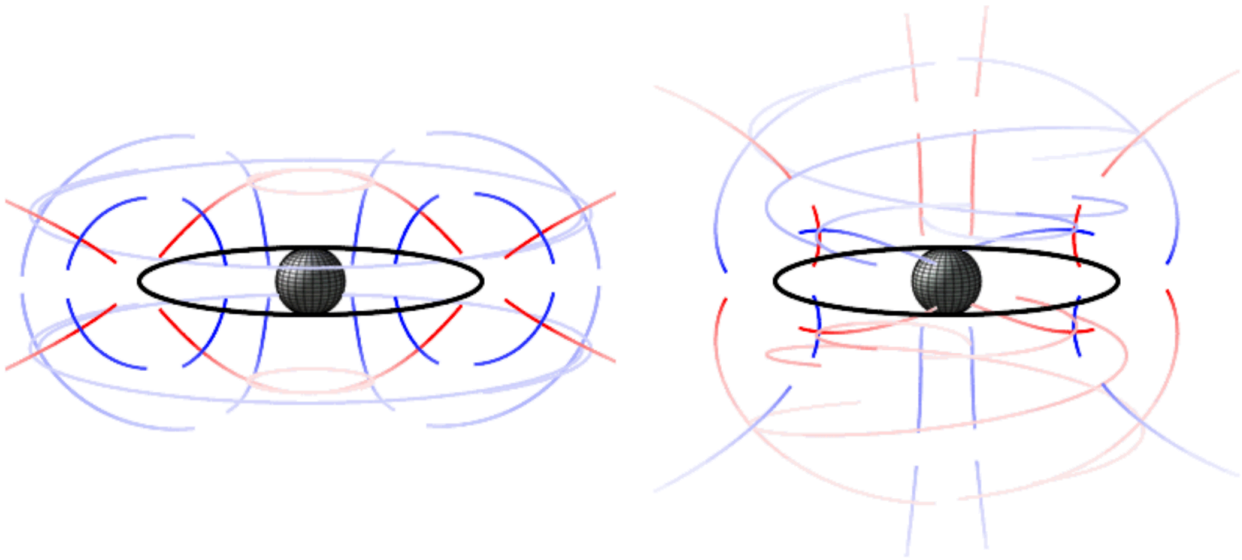

Figure 5.5: Tendex lines (left panel) and vortex lines (right panel) for the perturbation by a rotating ring around the Schwarzschild black hole. Note that the field for the unperturbed Schwarzschild metric is subtracted. Due to the numerical computation cost, the regions near the surface $r = r_0$ and the equatorial plane $\theta = \pi/2$ is omitted.

three families of tendex lines (the left panel). We see stretching red tendex lines that spreading from the ring, on ϕ constant planes. The red lines which approach the axis bend so that they cross the axis orthogonally. Around the axis, we see squeezing blue tendex lines along the axis. Off the axis, these blue lines become closed. These closed blue line is more circular, near the ring. The third family of tendex lines is r-θ constant circles. The lines are red inside the surface $r = r_0$ and blue outside it. The right panel of Fig. 5.5 shows the vortex lines. There are again three families of vortex lines. We see two families of poloidal vortex lines (blue and red). They are counterparts of each other, which are obtained by $(\theta \to \pi - \theta)$. They are orthogonal to each other. Near the axis, we see nearly parallel lines and orthogonal lines to the axis. The parallel ones can be understood simply: because the frame-drag effect is stronger

near the equatorial plane where the ring is, this differential dragging makes twisting along the axis. The direction of twisting (red and blue in color) is opposite between the northern side $\theta \sim 0$ and the southern side $\theta \sim \pi$. The lines which are orthogonal to the axis curl around the ring, as they approach the ring. This inspiraling feature becomes clearer when we plot only one family of lines denser. Another feature of these lines are seen near the event horizon of the black hole. The lines slightly gain toroidal component near the horizon. The third family of the vortex lines is more toroidal. Contrary to the toroidal tendex lines, these vortex lines are not closed circles. While the three families of lines cross orthogonally to each other, there are two families of blue lines and one family of red lines in the northern hemisphere, and there are two families of red lines and one family of blue lines in the southern hemisphere. On the equatorial plane, since the third family of lines vanish (the eigenvalue is zero), there are only two families of lines, blue and red.

The tendex fields for the Kerr case ($a = 0.99M$) are shown in Fig. 5.6. In order to compare with the field by $\Psi_{\rm P} + \Psi_{\rm H}$, the fields by $\Psi_{\rm P}$ are also shown in the top row. The gravitational field by $\Psi_{\rm P}$ has singularity (non-differentiability) on the surface $r = r_0 (= 10M)$ and lacks mass perturbation and angular momentum perturbation by the ring. The singularity is not very clear in the figures, but we see that the behavior in large $r > r_0$ is significantly different from the completed version in the bottom row. In the far region $r \gg r_0$, we expect that stretching red tendex lines are radial from the ring, and we indeed have such red lines for the completed field by Ψ. Finally, despite the completed Hertz potential and associating gravitational fields have singular plane on the equatorial plane outside the ring, $(r > r_0, \theta = \pi/2)$, we do not find any discontinuous behavior in the tendex field.

The vortex fields for the Kerr case ($a = 0.99M$) are shown in Fig. 5.7. The poloidal, blue vortex field is shown. Compared to the tendex field, the discontinuity on the surface $r = r_0$ by the $\Psi_{\rm P}$ is clearer (Top panels). Particularly, it is the clearest near the axis $(r = r_0, \theta \sim 0)$. This discontinuity is cancelled when the gravitational field is completed by $\Psi_{\rm H}$, which includes the lower mode perturbations. The completed version of vortex field is shown in the bottom panels

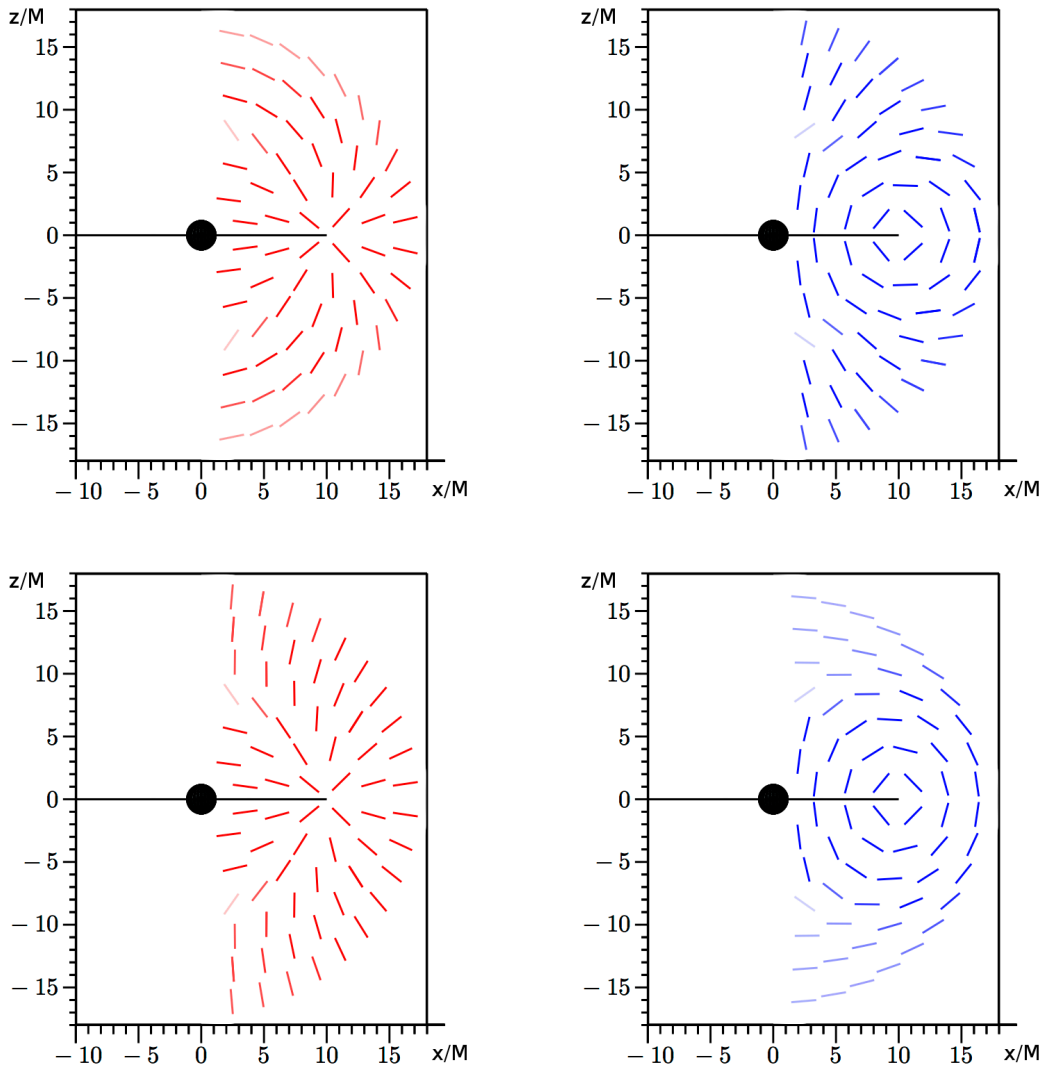

Figure 5.6: Tendex fields for the perturbation by a rotating ring around the Kerr black hole with $a = 0.99M$. The system is viewed edge-on. The ring with radius $r_0 = 10M$ is depicted as a horizontal line. The toroidal, two families (red and blue) of lines are shown. Note that field for the unperturbed Kerr space-time is subtracted. The fields are plotted on the plane $(r_h < r < 2(r_0 - r_h), 0 < \theta < \pi, \phi = 0)$, where $r_h = M + \sqrt{M^2 - a^2}$ is the (outer) event horizon. Left panels: Stretching red tendex field. Right panels: Squeezing blue tendex field. Top panels: Fields derived by $\Psi_{\rm P}$, without $l = 0,\ 1$ modes. Bottom panels: Fields derived by the completed Hertz potential Ψ. The discontinuity of the gravitational field is on the equatorial plane outside the ring, $(r > r_0, \theta = \pi/2)$. Interestingly, we do not see that discontinuity with tendex fields.

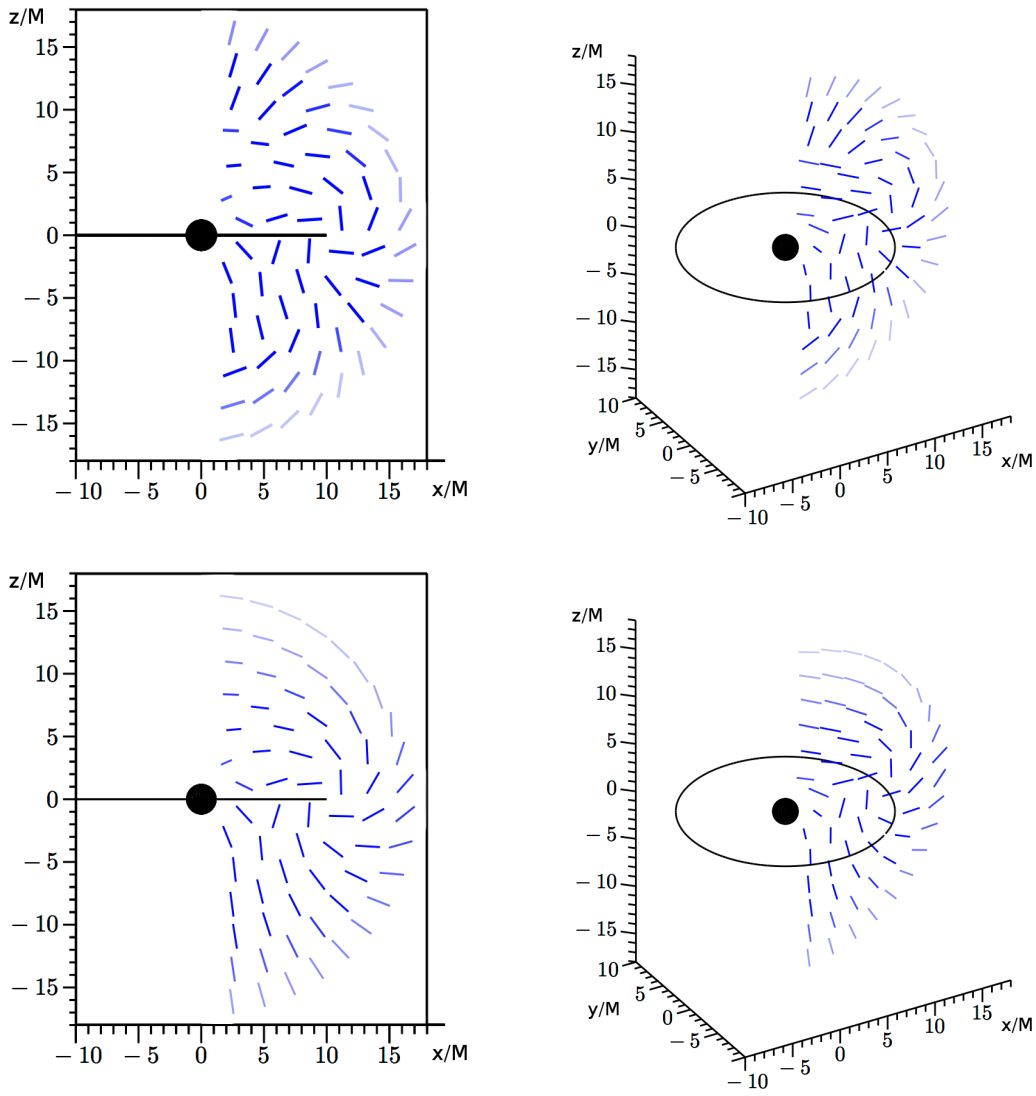

Figure 5.7: Vortex field for perturbation by a rotating ring around the Kerr black hole with $a = 0.99M$. Toroidal blue vortex field is shown. Note that field for the unperturbed Kerr space-time is subtracted. The fields are plotted on plane $(r_h < r < 2(r_0 - r_h), 0 < \theta < \pi, \phi = 0)$, where $r_h = M + \sqrt{M^2 - a^2}$ is the event horizon. The radius and the mass of the ring are $r_0 = 10M$, $m = 2\pi \times 10^{-2}M$. Top left panel: Field derived by the $\Psi_{\rm P}$, without $l = 0,\ 1$ modes. The system is viewed edge-on. Top right panel: Same as the top left panel, from a different viewpoint. Bottom left panel: Field derived field by the completed $\Psi_{\rm P} + \Psi_{\rm H}$. The system is viewed edge-on. Bottom right panel: Same as the bottom left panel, from a different viewpoint. The discontinuity of the gravitational field is on the equatorial plane outside the ring, $(r > r_0, \theta = \pi/2)$. Interestingly, we do not see that discontinuity with vortex fields.

in Fig. 5.7. The vectors near the northern axis continue to be nearly parallel to the axis, from the inside to the outside of $r = r_0$. The most characteristic feature we can observe is the spiral pattern around the ring ($r = r_0, \theta = \pi/2$). This blue spiral pattern in the figure indicates that the mass at ($r = r_0, \theta = \pi/2, \phi = 0$) has momentum and its direction is perpendicularly towards the back of the paper. Spiral pattern like this near the ring can be observed in the top panels, too. Therefore, we can say that local effect of frame-drag by the ring is already included in the uncompleted version of vortex field by $\Psi_{\rm P}$. However, the axis-aligned vector field far from the ring ($r > r_0$, to the far north for red and to the far south for blue) is not observed until the $\Psi_{\rm H}$ is added. When we add the $\Psi_{\rm H}$, the asymptotic behavior of the vortex field becomes similar to the vortex field of a rotating black hole (Fig. 5.1). Because the asymptotic behavior of the vortex field is determined by the angular momentum of the space-time, it means that the angular momentum perturbation (outside of $r = r_0$) is added when we add the $\Psi_{\rm H}$. There are two more families of vortex field. One red vortex field are obtained by ($\theta \to \pi - \theta$) reversing of the blue vortex field in Fig. 5.7. The third family of vortex field is the most toroidal one.

5.4 Black hole binary by Mundim *et al.*

The tendex and vortex lines could be used for visualizing various space-time. In this section, we consider the space-time of a black hole binary by Mundim *et al.* (2014). They constructed an analytic, non spinning black hole binary space-time via asymptotic matching. In the far zone where distance from the center of mass is sufficiently larger than the gravitational wave wavelength, the metric is solved using the multipolar post-Minkowskian expansion. In the near zone where distance from a black hole is sufficiently larger than the size of the black hole but sufficiently smaller than the wavelength, the metric is solved using the post-Newtonian expansion. In the inner zone where distance from a black hole is sufficiently smaller than the separation of the binary, the metric is solved as the perturbed black hole metric. Thus there

are two inner zones around each black hole. Marginal regions are called buffer zones, where the metric is described by superposition of metrics in the adjoining zones. Each metric is properly gauge-transformed so that they match well. These gauge transformations and the matching using carefully designed transition functions are the most important points in the construction of this space-time.

5.4.1 Set-up

Cartesian coordinates (x, y, z) are used. The origin $(0, 0, 0)$ is fixed at the center of mass of the binary. Since the black holes do not have spins, the binary's orbital plane is fixed. We set the x-y plane to be the orbital plane and $+z$ to be the direction of the binary's angular momentum. The black hole mass is denoted by m_1 and m_2, and the total mass is $M = m_1 + m_2$. The positions of black holes are denoted by $\vec{x}_1 = (x_1, y_1, z_1 = 0)$ and $\vec{x}_2 = (x_2, y_2, z_2 = 0)$. Coordinate distance from each black hole is denoted by $r_A = \sqrt{(x - x_A)^2 + (y - y_A)^2 + z^2}$, where $A = 1,\ 2$. The separation between the black holes is defined as $r_{12} = \sqrt{(x_1 - x_2)^2 + (y_1 - y_2)^2}$.

5.4.2 Inner zones

In this section, we show the tendex and vortex fields of the binary whose masses are $m_1 = M/6$ and $m_2 = 5M/6$. The separation is $r_{12} = 100M$. First, the tendex fields around black hole 1 are shown in Fig. 5.8. In this region, the metric is described by the inner zone metric $g_{\mu\nu}^{(\mathrm{IZ1})}$. The center of black hole 1 is at $(83.3M, 0, 0)$. There are two families of squeezing blue tendex lines and one family of stretching red tendex lines. As expected, stretching red field is radial from the black hole, and squeezing blue fields are concentric.

The vortex fields are shown in Fig. 5.9. The plotted region is the same as the tendex fields in Fig. 5.8. We show two families of vortex fields: blue and red. It is because the third eigenvalue is more than 10^4 times smaller than other two eigenvalues. On x-z plane, the blue vortex lines lie on the plane and we can see the spiral pattern, because the black hole's velocity

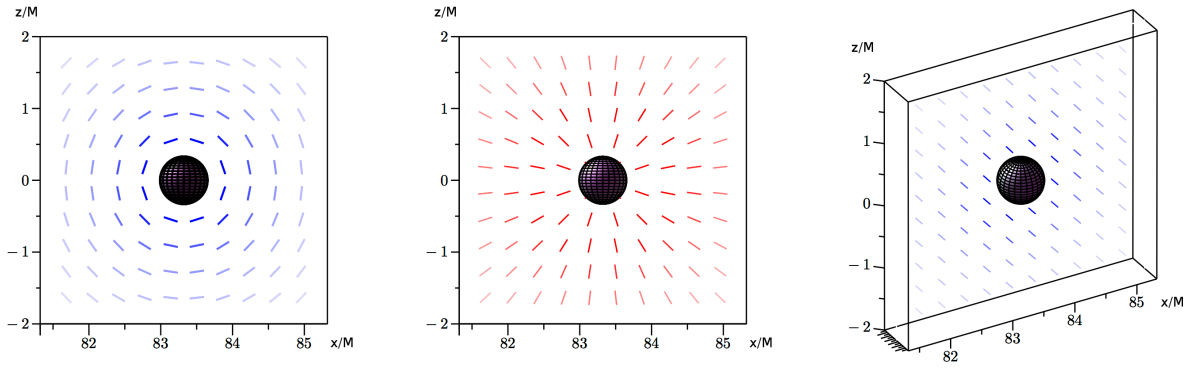

Figure 5.8: Tendex fields around black hole 1, which is at $(83.3M, 0, 0)$ and the mass is $m_1 = M/6$.

is $+y$ direction. Red vortex lines also lie on x-z plane and we see the spiral pattern of opposite direction to the blue one.

5.4.3 Near zone

In this section we show larger region. First, we present the tendex and vortex fields around black hole 1 where the metric can be described by superposition of $g_{\mu\nu}^{(\mathrm{IZ1})}$ and $g_{\mu\nu}^{(\mathrm{NZ})}$. Then we discuss the transition function between the inner zone and the near zone. After that, we present the tendex and vortex fields around two black holes where the metric can be described by superposition of $g_{\mu\nu}^{(\mathrm{IZ1})}$, $g_{\mu\nu}^{(\mathrm{IZ2})}$, and $g_{\mu\nu}^{(\mathrm{NZ})}$.

We consider region around black hole 1 where the metric is described by

$$g_{\mu\nu} = f_{\mathrm{inner},1} g_{\mu\nu}^{(\mathrm{NZ})} + (1 - f_{\mathrm{inner},1}) g_{\mu\nu}^{(\mathrm{IZ1})}. \tag{5.14}$$

The transition function is given as (Mundim *et al.* 2014)

$$f_{\mathrm{inner},A} = f(r_A, 0.256(m_A{}^3 r_{12}{}^5/M)^{1/7}, 3.17(M^2 r_{12}{}^5)^{1/7}, 0.2, r_{12}/M), \tag{5.15}$$

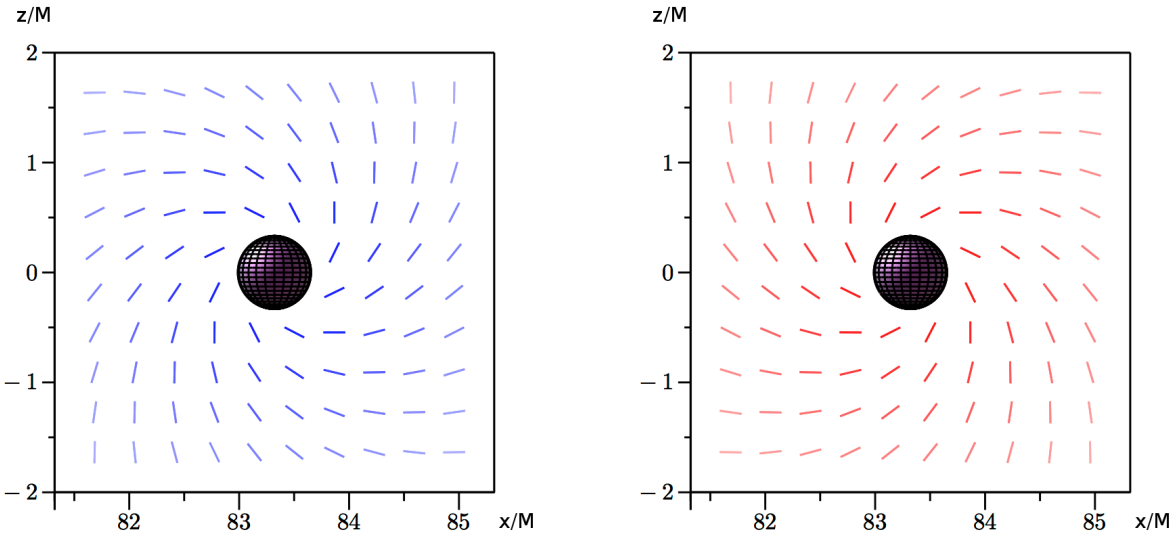

Figure 5.9: Vortex fields around black hole 1, which is at $(83.3M, 0, 0)$ and the mass is $m_1 = M/6$.

where

$$f(r, r_0, w, q, s) = \begin{cases} 0, & r \le r_0, \\ \frac{1}{2}\left\{1 + \tanh\left[\frac{s}{\pi}\left(\chi(r, r_0, w) - \frac{q^2}{\chi(r, r_0, w)}\right)\right]\right\}, & r_0 < r < r_0 + w \\ 1, & r \ge r_0 + w \end{cases} , \tag{5.16}$$

$$\chi(r, r_0, w) = \tan\left[\frac{\pi(r - r_0)}{2w}\right] . \tag{5.17}$$

We show the tendex and vortex field on the x-z plane in Fig. 5.10. Stretching red tendex field is shown in top-left panel. Blue vortex field is shown in top-right panel. In these figures, we find some points where plot is not seen. At such points, eigenvector does not lie on x-z plane or eigenvalue is too small (plotted color is too white) to be seen. When we plot the integrated tendex and vortex lines, these anomalies cause sudden breaks of the lines. We reported this problem to Nakano, who is a co-author of Mundim *et al.* (2014). Nakano re-examined the transition function and he improved it. According to him, the problem was not noticed when

Mundim *et al.* (2014) designed the transition function because they only check for the case of $m_1/m_2 = 1$, $r_{12} = 10M$. The improved transition function is different from the original function by one parameter, $s = 12$:

$$f_{\mathrm{inner},A} = f(r_A, 0.256({m_A}^3{r_{12}}^5/M)^{1/7}, 3.17(M^2{r_{12}}^5)^{1/7}, 0.2, 12). \tag{5.18}$$

The tendex and vortex field with the improved transition function are shown in bottom row in Fig. 5.10. Improved red tendex field is shown in bottom-left panel. Improved blue vortex field is shown in bottom-right panel. The improvement is significant. First, we no longer observe anomalies and the fields are smooth. Second, gradation of the intensity of color (gradient of eigenvalues) is smoother.

Next, we show the tendex and vortex fields around black hole 1 and 2, where the metric is given by (Mundim *et al.* 2014)

$$g_{\mu\nu} = f_{\mathrm{near}}\left[f_{\mathrm{inner},1}g^{(\mathrm{NZ})}_{\mu\nu} + (1 - f_{\mathrm{inner},1})g^{(\mathrm{IZ1})}_{\mu\nu}\right] + (1 - f_{\mathrm{near}})\left[f_{\mathrm{inner},2}g^{(\mathrm{NZ})}_{\mu\nu} + (1 - f_{\mathrm{inner},2})g^{(\mathrm{IZ2})}_{\mu\nu}\right], \tag{5.19}$$

where

$$f_{\mathrm{near}} = f(x', 2.2m_2 - m_1 r_{12}/M, r_{12} - 2.2M, 1, 1.4), \tag{5.20}$$

$$x' = \frac{1}{r_{12}}(\vec{x}_1 - \vec{x}_2) \cdot \vec{x}. \tag{5.21}$$

Tendex fields are displayed in the top row of Fig. 5.11. Black hole 1 is at $(83M, 0, 0)$ and black hole 2 is at $(-17M, 0, 0)$. Vortex fields are displayed in the bottom row of Fig. 5.11. The velocities of black holes are perpendicular to the paper. Black hole 1 is at $(83M, 0, 0)$ and its velocity is $+y$ direction, which is toward the back of the paper. Black hole 2 is at $(-17M, 0, 0)$ and its velocity is $-y$ direction, which is toward the reader. That is the reason why the two spiral patterns around the black holes are oppositely-directed to each other. Next, we note the symmetry about a x constant line in this figure. By an observation, the line passes through the midpoint of the binary: $((x_1, y_1) + (x_2, y_2))/2 = (33M, 0)$. With respect to the midpoint, the magnitudes of each angular momentum is equal. It is proved as follows. Because the origin

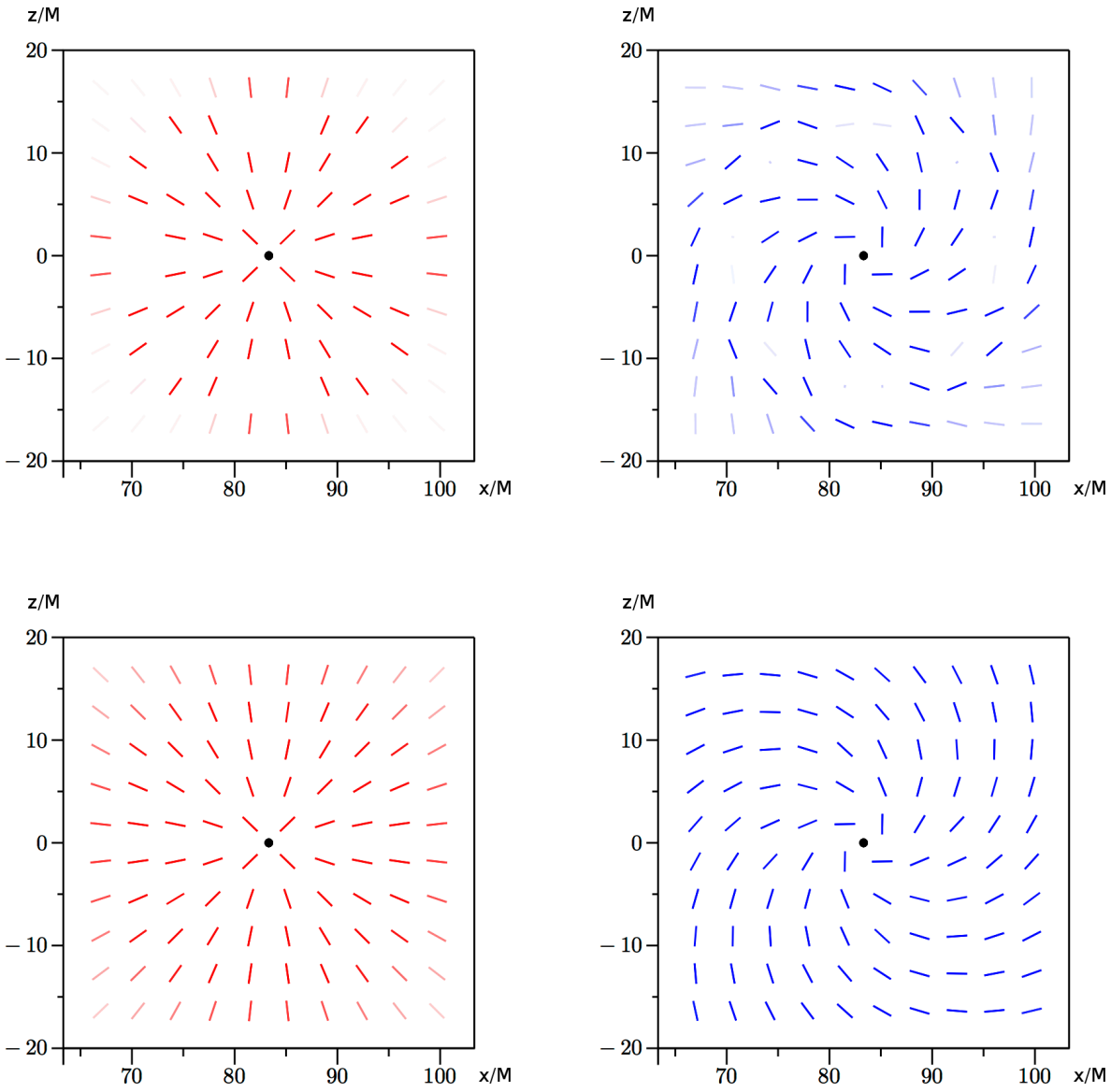

Figure 5.10: Left column: Red tendex field. Right column: Blue vortex field. Top row: Calculated with transition function Eq. (5.15). Bottom row: Calculated with improved transition function Eq. (5.18). The improvement of the matching is visualized.

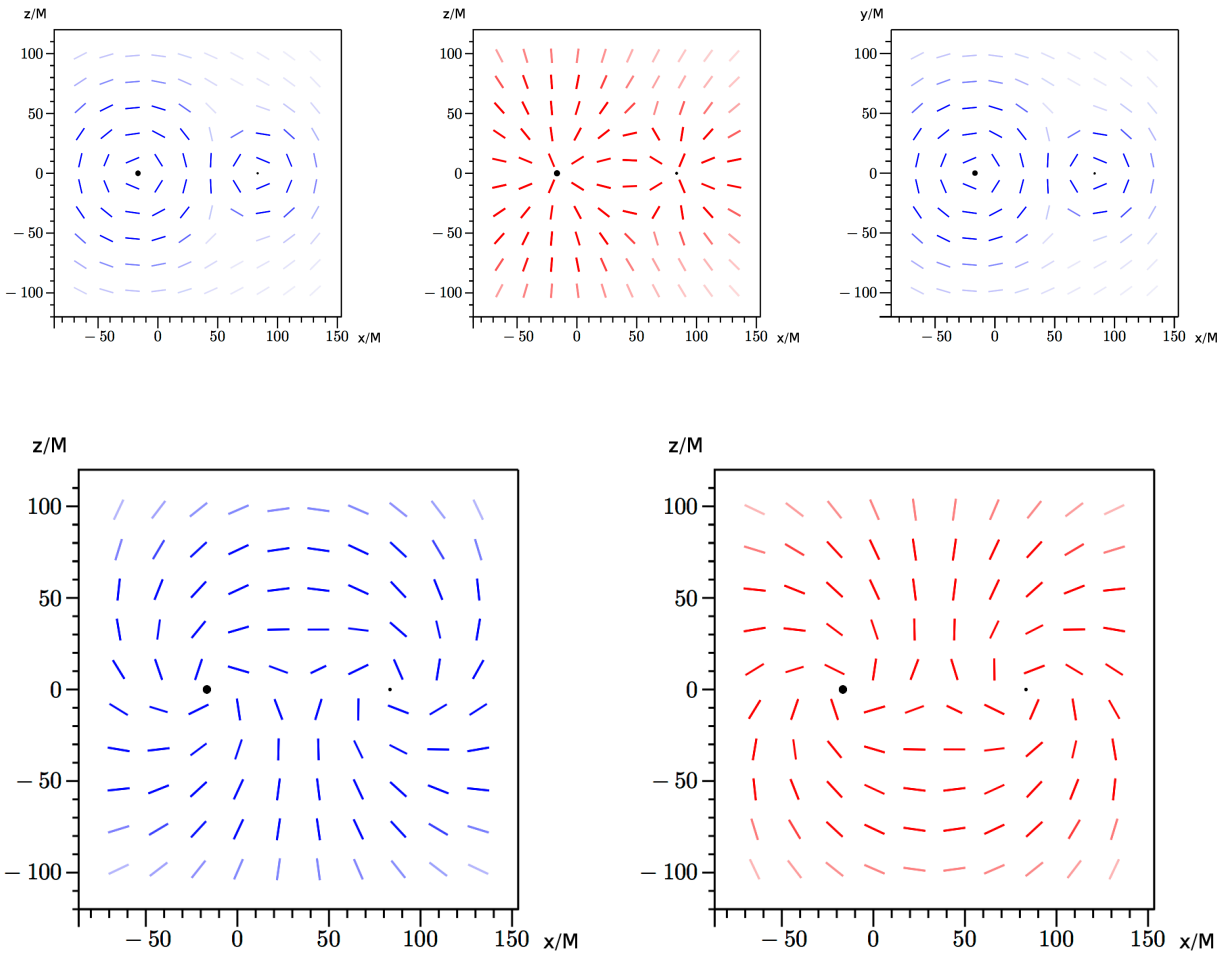

Figure 5.11: x-z plane. Top left panel: Squeezing blue tendex field. Top middle panel: Stretching red tendex field. Top right panel: Squeezing blue tendex field on the orbital plane. Bottom left panel: Blue (positive eigenvalue) vortex field. Bottom right panel: Red (negative eigenvalue) vortex field. On this plane, the vortex field looks roughly symmetric about a x constant line. The center of angular momentum $(x = (x_1 + x_2)/2, y = (y_1 + y_2)/2, 0)$ is on this line.

of the coordinates system is fixed at the center of mass of the binary, the ratio of magnitudes of velocities is the inverse of mass ratio. Then ratio of magnitudes of momenta is 1.

$$v_1/v_2 = m_2/m_1, \quad (m_1 v_1)/(m_2 v_2) = 1. \tag{5.22}$$

Therefore, when we choose the midpoint as the origin of rotation, the ratio of magnitudes of angular momenta becomes 1.

$$\frac{1}{2}\sqrt{(x_2 - x_1)^2 + (y_2 - y_1)^2} m_1 v_1 = \frac{1}{2}\sqrt{(x_1 - x_2)^2 + (y_1 - y_2)^2} m_2 v_2. \tag{5.23}$$

The pattern of vortex field in Fig. 5.11 is similar to Fig. 5.7, the case for a black hole and a rotating ring. However, while the ring case is axisymmetric, the binary's gravitational field is not. Only when we take a plane as a cross section so that velocities of mass (binary or ring) are perpendicular to the plane, the common pattern can be seen. The asymptotic behavior is similar to the vortex fields of a rotating black hole (bottom panels of 5.1).

5.4.4 Far zone

In this section we show the gravitational wave and its propagation in far zone. The metric is given by (Mundim *et al.* 2014)

$$\begin{aligned} g_{\mu\nu} = f_{\rm far} g^{\rm (FZ)}_{\mu\nu} + (1 - f_{\rm far}) \big\{ f_{\rm near} \left[f_{{\rm inner},1} g^{\rm (NZ)}_{\mu\nu} + (1 - f_{{\rm inner},1}) g^{\rm (IZ1)}_{\mu\nu} \right] \\ + (1 - f_{\rm near}) \left[f_{{\rm inner},2} g^{\rm (NZ)}_{\mu\nu} + (1 - f_{{\rm inner},2}) g^{\rm (IZ2)}_{\mu\nu} \right] \big\}, \end{aligned} \tag{5.24}$$

where

$$f_{\rm far} = f(r, \lambda/5, \lambda, 1, 2.5), \quad \lambda = \pi \sqrt{{r_{12}}^3/M}. \tag{5.25}$$

We show the tendex field on the orbital plane of the binary (x-y plane) because there are two families of tendex lines which lie on the plane. Figures in this section is plotted in different manner from the previous sections. We choose the "stronger" tendex line on the x-y plane to plot. The meaning is as follows. Recall that tendex line is the field line of each eigenvector field

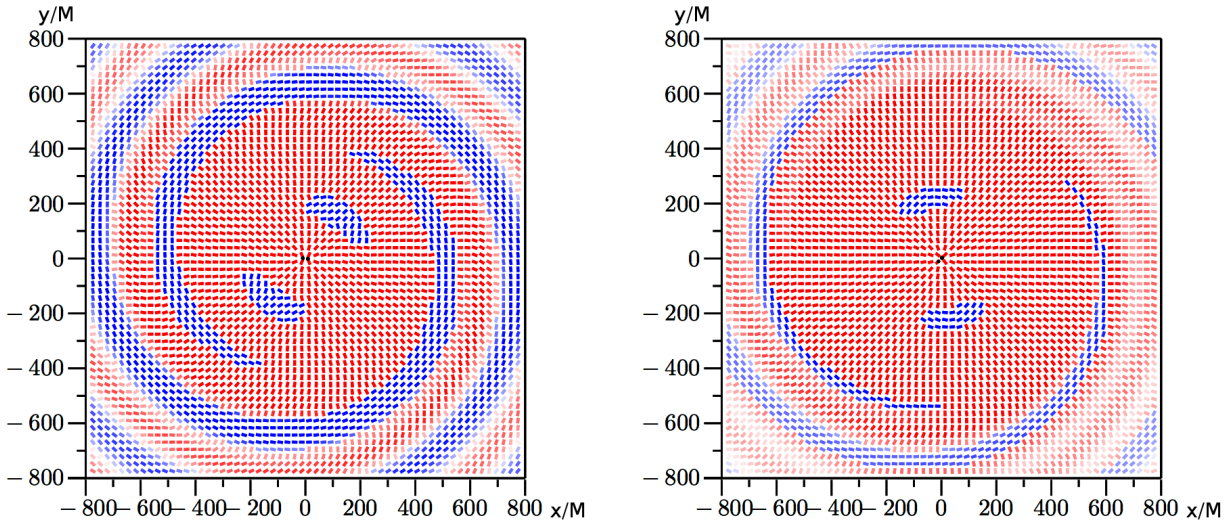

Figure 5.12: Tendex field on the orbital plane. Top-left panel: Mass ratio is 1. Separation is $r_{12} = 18.0M$. Top-right panel: Mass ratio is 5. Separation is $r_{12} = 18.9M$.

of $\mathcal{E}_{ij}$. At each point on the orbital plane, one vector among three eigenvectors is perpendicular to the plane. We do not plot the tendex field of this vector. The other two eigenvectors are on the plane. Let e_1 and e_2 to be the corresponding two eigenvalues. They are tendicities, and each of them represents the strength of tidal force in direction of corresponding eigenvector. Then we compare the magnitude of tendicities $|e_1|$ and $|e_2|$, and choose the larger one. Finally, the corresponding eigenvector is plotted on the x-y plane.

The tendex field to far zone is shown in Fig. 5.12. In the figure, the binary is rotating counter-clockwise. We can see blue and red arms, which are in-spiraling counter-clockwise. The difference between the left and right panel is the mass ratio of the binary. The left panel is for $m_1 = m_2 = M$. We see $(x, y) \leftrightarrow (-x, -y)$ symmetry due to the equal mass ratio. The widths of two blue arms look the same. The right panel is for $m_1 = M/6$, $m_2 = 5M/6$. In this case, the widths of two blue arms are different. Further, between blue arms we can see white

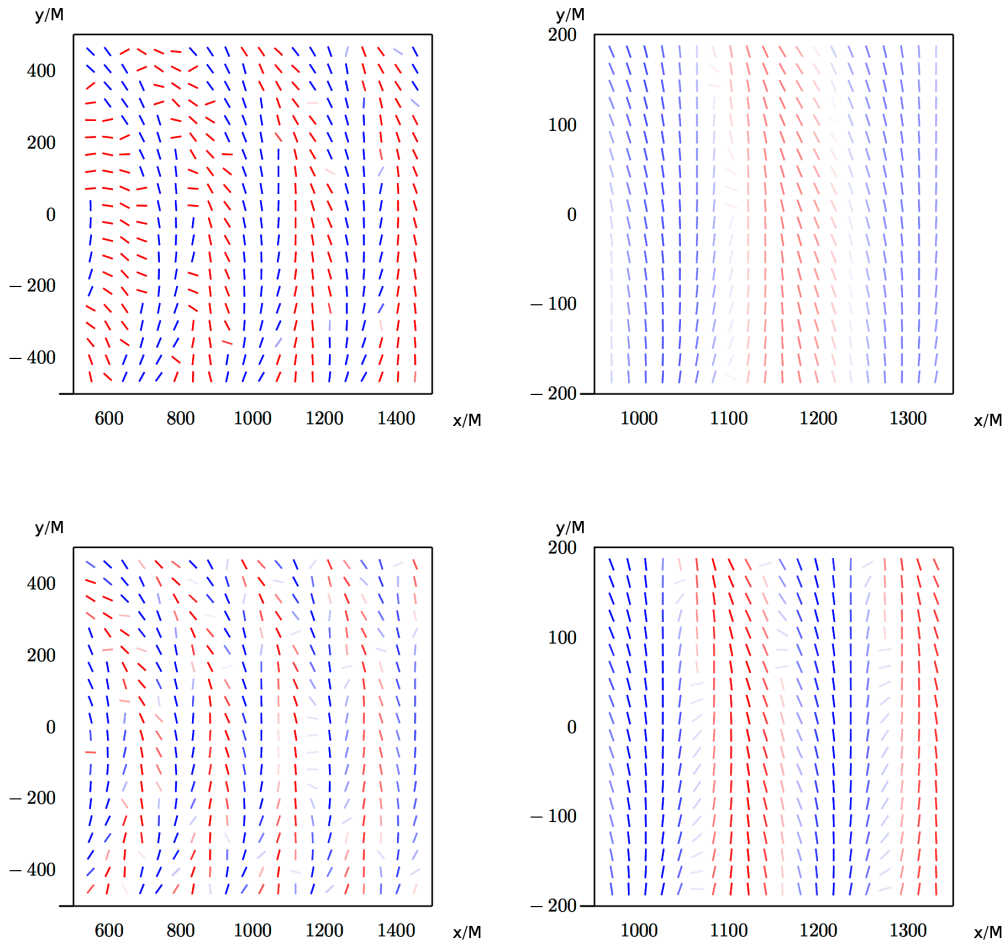

Figure 5.13: Tendex field on the orbital plane. The mass ratio is 1. Time t is different between the top panels and the bottom panels. Top panels: The time when the separation is $r_{12} = 18M$ ($t = 5000M$). Bottom panels: The time when the separation is $r_{12} = 15M$ ($t = 10000M$). In the right panels, nearly plane wave can be observed as a fringe pattern. It is clearly visualized that the wavelength becomes smaller as the black holes approach each other. Note that the relation between the intensity of color and the absolute value of eigenvalue (tendicity) is independently changed for each figure, so that we see the gradient of tendicity.

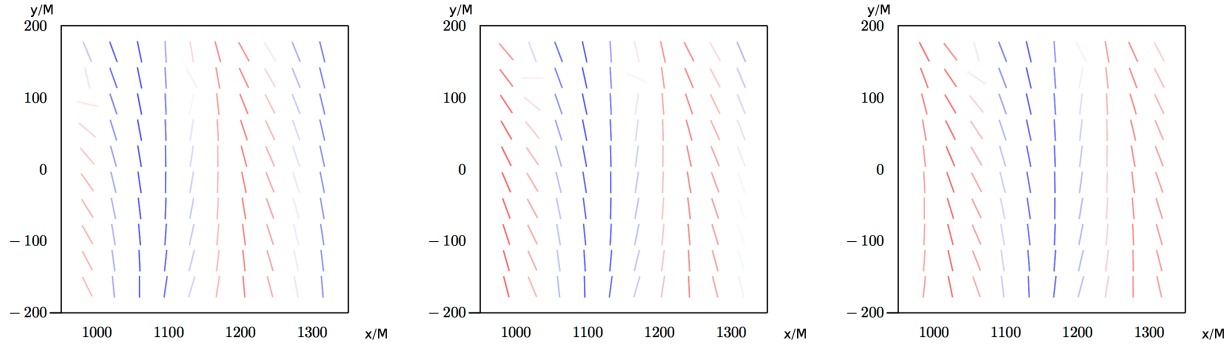

Figure 5.14: Vortex fields in a far region $r \gg r_{12}$. The mass ratio is 1. The left, middle, and right plane shows the orbital plane at $t = 5040M$, $t = 5080M$, and $t = 5120M$, respectively. The separation of the binary is $r_{12} = 18M$. The wavelength is estimated as $\lambda \sim \pi\sqrt{{r_{12}}^3/M} = 2.4 \times 10^2 M$. The wavelength estimated from the figure is $\lambda \sim 2.9 \times 10^2 M$. The propagation speed of the pattern which is estimated from the figures is $v \sim c = 1$.

(light red) streaks, where stretching red tendicity is relatively weak.

Fig. 5.13 show tendex fields in smaller and further regions, whose range is smaller compared to distance from the binary. We see a fringe pattern of blue and red streaks, which is the gravitational wave.

The time evolution of the fringe pattern is shown in Fig. 5.14. At time $t = 4040M$, the separation of the binary is $r_{12} = 18.4M$ and at $t = 5040M$, $r_{12} = 17.9M$. The wavelength can be estimated by $\lambda \sim \pi\sqrt{{r_{12}}^3/M}$ (Mundim *et al.* 2014). It is $\lambda_{4040} \sim 248M$ at $t = 4040M$, and $\lambda_{5040} \sim 239M$ at $t = 5040M$. Because the propagation speed of the gravitational wave is $c = 1$, we expect that the wavelength of wave at $t \sim 5040M$ and $(x \sim 1000M, y = 0, z = 0)$ is $\lambda \sim \lambda_{4040}$. However, the resolution of Fig. 5.14 is not enough to estimate the wavelength accurately. Estimated value is $\lambda \sim 2.9 \times 10^2 M$.

Fig. 5.15 shows squeezing blue tendex field on x-z plane. We see concentric shell-like regions where blue tendicity is relatively large. On each shell, change in tendicity is not

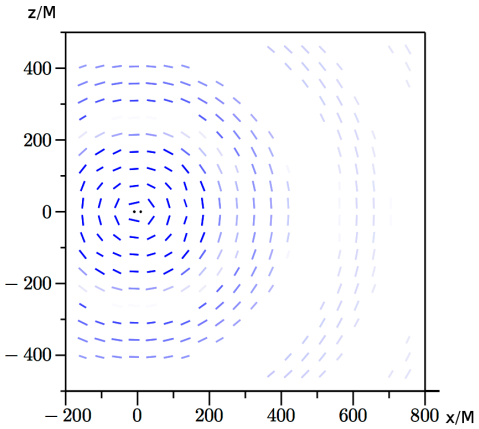

Figure 5.15: Squeezing blue tendex field on x-z plane. Two black dots represent the binary on $z = 0$ plane. Roughly concentric structure of region is observed, where blue (positive) tendicity is relatively strong. In this figure, the red tendex field is not shown.

observed clearly.

5.4.5 Discussion and summary

Before summarizing this chapter, we discuss the visual differences according to the plotting methods. In Fig. 5.16, integrated tendex lines on the orbital plane are shown. Two panels in the top row show stretching red tendex lines on the orbital plane, around black hole 1. The left panel is for the metric before the transition function f_{inner} is improved, and the right panel is for the improved version. The improvement of matching is significantly observed in these figure. The bottom-left panel shows tendex lines on the orbital plane, in inner zones to the near zone. In spite of their simple-looking, it costs more time and sensibility to design figures. For a presentation, integrated lines might be better because it's easier to recognize the changing of directions. However, in advance of making such a figure, we need to know well about the space-time and decide what we are going to tell with the figure. We need to note that impression of a figure strongly depends on which lines we plot.

On the other hand, figures such as Fig. 5.4 and 5.6 are more objective and can be made straightforwardly. A disadvantage of this method is that it is difficult to recognize three-dimensional structure of tendex and vortex lines.

We summarize this chapter. We discussed the properties of space-time of several systems by drawing tendex lines and vortex lines. The systems we considered in this chapter were (1) the Kerr black hole and a particle at rest, (2) the Kerr black hole and a rotating ring, and (3) a binary of non-spinning black holes. The visualization was useful for explaining and understanding the basic properties of the space-time. In addition, we found that the matching condition of the binary space-time was inaccurate. It appeared as unphysical distortions of the tendex and vortex fields. The matching condition was improved.

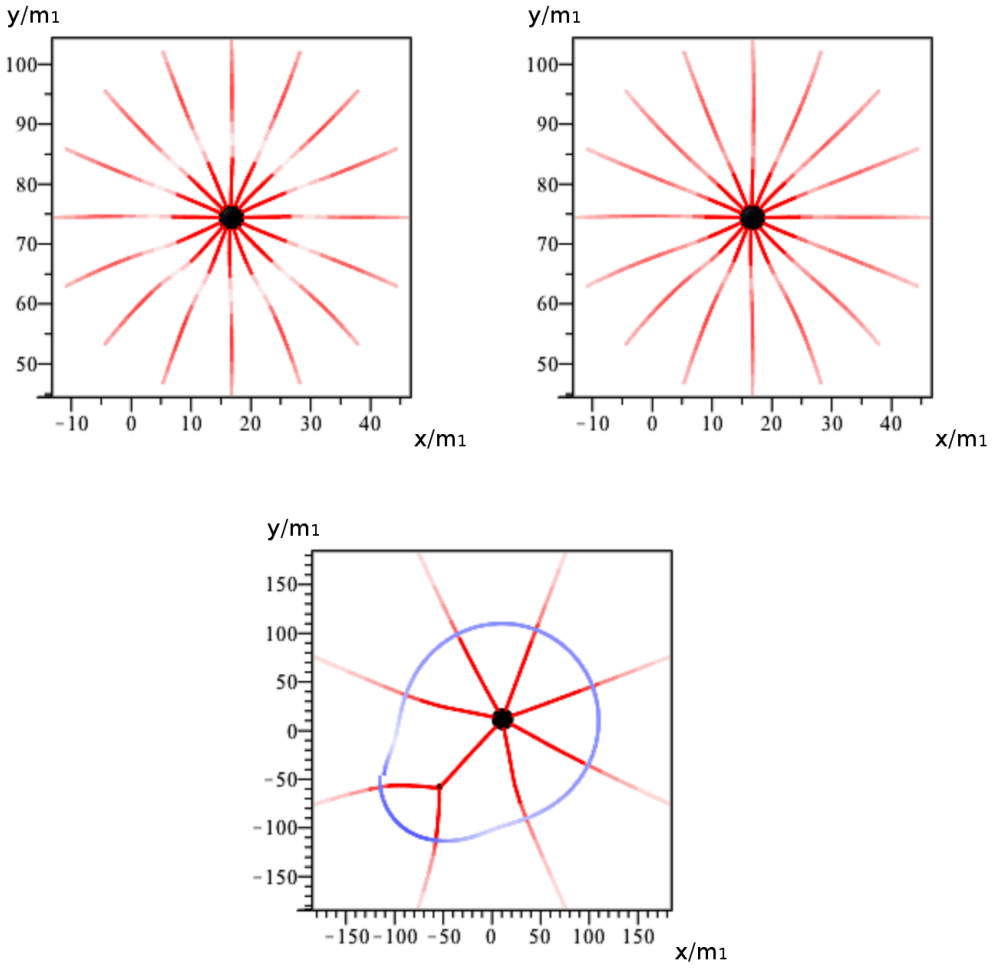

Figure 5.16: Integrated tendex lines on the orbital plane. Top-left panel: Near zone and inner zone around black hole 1 ($m_1 = M$). In this panel, the metric is calculated using transition function Eq. (5.15), which is given in Mundim *et al.* (2014). Circular region of weakened red tendicity (white circle) is observed because the transition between near zone and inner zone is not perfect. Top-right panel: Same as the top-left panel, with improved transition function Eq. (5.18). Improvement of transition is when we compare this figure to the top-left panel. Bottom-left panel: Mass ratio is $m_2/m_1 = 5$. We see two regions where squeezing blue tendicity is weak.

Chapter 6

Conclusion

6.1 Summary

In the first part of this thesis, we investigated a method to calculate first order perturbation of the Kerr metric. We used the Teukolsky equation to solve the Weyl scalar ψ_0 and ψ_4, and constructed the metric perturbation from them using the CCK formalism. In this method, it has been a problem that we cannot calculate the $l = 0$ and $l = 1$ modes of perturbation from ψ_0 and ψ_4. These modes are important because they correspond to the mass and angular momentum perturbation of the space-time. We tackled this problem by considering the perturbation induced by a rotating ring, and successfully calculated the metric perturbation including the lower modes.

In the CCK formalism, the metric perturbation is calculated in a radiation gauge, via the Hertz potential Ψ, which obeys fourth order differential equations with ψ_0 and ψ_4 as source terms. The particular solution for the Hertz potential, $\Psi_{\rm P}$ is obtained in terms of ψ_0 and ψ_4, and it has only $l \geq 2$ modes. Further, an unphysical singularity appeared in $\Psi_{\rm P}$ on the surface of sphere at the ring radius. Gravitational fields become discontinuous on the surface if we derive them from $\Psi_{\rm P}$. On the other hand, the homogeneous solution part $\Psi_{\rm H}$ should be added to include the lower modes. The degrees of freedom of $\Psi_{\rm H}$ reduces to eight complex

parameters. These parameters correspond to the information of $l = 0$ and $l = 1$ modes of perturbation and the gauge freedom. We found that we can determine the parameters by imposing the continuity condition for gravitational fields, and when we do so the gravitational fields become smooth at $r = r_0$. In order to do this, we divided the space into three regions: inside the ring radius r_0, the northern half outside r_0, and the southern half outside r_0. We obtained the perturbed gravitational field which is smooth at $r = r_0$. The parameters which correspond to the mass perturbation and angular momentum perturbation give the correct values of energy and angular momentum of the ring, respectively. This agreement is checked for the Schwarzschild case. This suggests the validity of the method and the results. The perturbation of the Kerr metric induced by a particle at rest is also obtained with the procedure we found. We obtained the perturbed gravitational field which is smooth at $r = r_0$.

In the second part of this thesis, we studied the visualization of space-time curvature with tendex and vortex lines. The tendex lines represent the effect of the tidal force, and the vortex lines represent the effect of the frame-dragging. These lines are drawn by evaluating the Weyl tensor on a space-like hypersurface. We visualized the perturbed black hole space-time described above. The visualization was useful for understanding the problem and for considering the method how to add $\Psi_{\rm H}$ for the lower-mode perturbations. We also applied the visualization to a space-time metric of a binary, which is constructed using asymptotic matching (Mundim *et al.* 2014). We analyzed the metric using the visualization and found unphysical distortions of the tendex and vortex fields. The distortions were due to the insufficient accuracy of the matching condition. The matching condition was improved.

6.2 Future works

First, we discuss the future works on the calculation of the metric perturbation. For the case of the Kerr black hole and a ring, we did not confirm the agreement between the physical parameters in $\Psi_{\rm H}$ and the perturbations of mass and angular momentum of the space-time.

In order to do this, we need to examine the contribution to the Kerr space-time by each parameter, using gauge transformations. If the agreement is confirmed, it suggests the validity of our method and results more strongly.

One of the simple set-ups other than what we considered in this thesis is the perturbation induced by a particle on a radial geodesic around a black hole. When we take the radial orbit on the axis of symmetry, the system is axisymmetric. The stationarity breaks. Considering this case might be useful as a preparation for more complicated cases.

When it is applied to the case of orbiting particle, both stationarity and axisymmetry break. Because of it, equations at almost every step become more complicated. An analytic expression for the spin-weighted spheroidal harmonics ${}_sS_{lm}^{a\omega}(\theta)$ are not known. Further, the homogeneous solution for the Hertz potential, $\Psi_{\rm H}$, depends on t, r, θ, and ϕ. It would make it more complicated to determine the parameters. However, once we obtain the gravitational field in a radiation gauge, it would be possible to compute the self-force with the prescription by Pound, Merlin, & Barack (2014).

Next, we discuss the future works on the visualization of space-time curvature. There is an interesting utilization, which is to use the lines to understand the relation between the perturbed space-time by a moving particle and the gravitational self-force acting on the particle. If it becomes possible, the visualization might give new insights about the gravitational self-force.

Appendix A

On different conventions of sign

There are different conventions about the sign among papers. Sometimes it causes confusion. We summarize the relations between different conventions.

A.1 Different definitions

A.1.1 Space-time metric tensor

The metric tensor g_{ab}.

Teukolsky (1973) and Keidl, Friedman, & Wiseman (2007) use $(+---)$ signature.

Wald (1984), Nakamura, Oohara, & Kojima (1987), and Pound, Merlin, & Barack (2014) use $(-+++)$ signature.

A.1.2 Riemann curvature tensor

The Riemann curvature tensor R_{abcd} in terms of metric g_{ab}.

The definition given by Wald (1984) is

$$R_{\mu\nu\rho}{}^{\sigma} = \frac{\partial}{\partial x^{\nu}}\Gamma^{\sigma}_{\mu\rho} - \frac{\partial}{\partial x^{\mu}}\Gamma^{\sigma}_{\nu\rho} + \left(\Gamma^{\alpha}_{\mu\rho}\Gamma^{\sigma}_{\alpha\nu} - \Gamma^{\alpha}_{\nu\rho}\Gamma^{\sigma}_{\alpha\mu}\right), \tag{A.1}$$

where

$$\Gamma^{\rho}_{\mu\nu} = \frac{1}{2} g^{\rho\sigma} \left(\frac{\partial g_{\nu\sigma}}{\partial x^{\mu}} + \frac{\partial g_{\mu\sigma}}{\partial x^{\nu}} - \frac{\partial g_{\mu\nu}}{\partial x^{\sigma}} \right). \tag{A.2}$$

On the other hand, apparently, Kegeles & Cohen (1979) define the curvature tensor with different sign. The reason is in Sec. A.1.3.

A.1.3 Ricci tensor

The Ricci tensor R_{ab} in terms of metric g_{ab} and Riemann curvature tensor R_{abcd}.

Eisenhart (1960) (Eq. (8.14)), and presumably Newman & Penrose (1962) and Teukolsky (1973) use $R_{bc} = R_{abcd} g^{da}$.

The definition given by Wald (1978) is $R_{ac} = R_{abcd} g^{db}$. In Kegeles & Cohen (1979), by comparing Eq. (2.19),

$$2R_{\alpha\beta\gamma\delta} = h_{\alpha\gamma;\beta\delta} + h_{\beta\delta;\alpha\gamma} - h_{\beta\gamma;\alpha\delta} - h_{\alpha\delta;\beta\gamma} + R^{(0)}_{\alpha\sigma\gamma\delta} h^{\sigma}{}_{\beta} - R^{(0)}_{\beta\sigma\gamma\delta} h^{\sigma}{}_{\alpha}$$

and Eq. (2.20),

$$2R_{\alpha\beta} = h_{;\alpha\beta} + h_{\alpha\beta;\rho}{}^{\rho} - h^{\rho}{}_{\alpha;\beta\rho} - h^{\rho}{}_{\beta;\alpha\rho} = 0,$$

we know that they use the same definition as Wald (1984). However, Eq. (2.20), the perturbed Ricci tensor in terms of the metric perturbation, is different by sign from that which is derived using the definition of R_{abcd} and R_{ab} by Wald (1984). This is why we believe that the definition of the Riemann tensor R_{abcd} used by Kegeles & Cohen (1979) is different from the one by Wald (1984).

A.1.4 Weyl scalars

The Weyl scalars Ψ_0, Ψ_1, ..., Ψ_4 in terms of Riemann curvature tensor R_{abcd} and basis vectors.

Teukolsky (1973), Nakamura, Oohara, & Kojima (1987), and Keidl, Friedman, & Wiseman (2007) use $\Psi_0 = -C_{abcd} l^a m^b l^c m^d$ etc., where the Weyl tensor C_{abcd} is the trace-free part of R_{abcd}.

Sano & Tagoshi (2014), Pound, Merlin, & Barack (2014), and Nichols *et al.* (2011) use $\Psi_0 = +C_{abcd}l^a m^b l^c m^d$ etc.

A.1.5 Ricci rotation coefficients

Here, we denote the rotation coefficients which are defined by Newman and Penrose (1962) by $\gamma^{\rm NP}_{\rho\mu\nu}$, in order to emphasize which definition we use:

$$\gamma^{\rm NP}_{\rho\mu\nu} = (\nabla_b (e_\rho)_a)(e_\mu)^a (e_\nu)^b. \tag{A.3}$$

In Wald (1984), the coefficients are denoted by $\omega_{\lambda\mu\nu}$:

$$\omega_{\lambda\mu\nu} = (e_\lambda)^b (e_\mu)^a (\nabla_b (e_\nu)_a) = \gamma^{\rm NP}_{\nu\mu\lambda}. \tag{A.4}$$

In Nakamura, Oohara, & Kojima (1987), the coefficients are defined as

$$\gamma^{\rm NOK}_{\rho\mu\nu} = (e_\rho)^a (\nabla_b (e_\mu)_a)(e_\nu)^b = -\gamma^{\rm NP}_{\rho\mu\nu}. \tag{A.5}$$

A.1.6 Spin coefficients

The spin coefficients ρ, μ, etc. in terms of metric g_{ab} and the null tetrad.

Newman & Penrose (1962) and Nakamura, Oohara, & Kojima (1987) use $\rho = l_{\mu;\nu} m^\mu \overline{m}^\nu$ etc. On the other hand, Sano & Tagoshi (2014) use $\rho = -l_{\mu;\nu} m^\mu \overline{m}^\nu$ etc.

Explicitly, in Newman & Penrose (1962), ρ is defined as

$$\rho_{\rm NP} = \gamma^{\rm NP}_{134} = l^+_{\mu;\nu} m^\mu \overline{m}^\nu = (l^\rho g^+_{\rho\mu})_{;\nu} m^\mu \overline{m}^\nu, \tag{A.6}$$

where $g^+_{\rho\mu}$ means the metric with $(+---)$ signature. On the other hand, in Nakamura, Oohara, & Kojima (1987), ρ is defined as

$$\begin{aligned} \rho_{\rm NOK} &= \gamma^{\rm NOK}_{314} = l^-_{\mu;\nu} m^\mu \overline{m}^\nu = (l^\rho g^-_{\rho\mu})_{;\nu} m^\mu \overline{m}^\nu \\ &= -\gamma_{134}, \end{aligned} \tag{A.7}$$

where $g^-_{\rho\mu}$ means the metric with $(-+++)$ signature. As a result,

$$\rho_{\rm NOK} = \gamma^{\rm NOK}_{314} = \gamma^{\rm NP}_{314} = -\rho_{\rm NP}. \tag{A.8}$$

A.1.7 Hertz potential

The relation between the Hertz potential Ψ and the metric perturbation in a radiation gauge is given in Chrzanowski; Kegeles & Cohen (1975; 1979) as

$$h^{\mathrm{IRG}}_{ab} = +D^{\mathrm{IRG}}_{ab}(\Psi), \quad h^{\mathrm{ORG}}_{ab} = +D^{\mathrm{ORG}}_{ab}(\Psi), \tag{A.9}$$

where differential operators D^{IRG}_{ab} and D^{ORG}_{ab} are defined as

$$\begin{aligned} D^{\mathrm{IRG}}_{ab}(\Psi) \equiv -\Big[&\Big\{l_a l_b(\overline{\boldsymbol{\delta}} + 2\overline{\beta} + \varpi - \overline{\tau}) - \overline{m}_{(a}l_{b)}(\boldsymbol{D} + \rho - \overline{\rho})\Big\}(\overline{\boldsymbol{\delta}} + 4\overline{\beta} + 3\overline{\tau}) \\ &+ \Big\{-l_{(a}\overline{m}_{b)}(\overline{\boldsymbol{\delta}} + 4\overline{\beta} - 2\varpi - \overline{\tau}) + \overline{m}_a\overline{m}_b(\boldsymbol{D} - \overline{\rho})\Big\}(\boldsymbol{D} + 3\overline{\rho})\Big]\overline{\Psi} + [\mathrm{c.c.}]\,, \end{aligned} \tag{A.10}$$

$$\begin{aligned} \rho^4\Delta^2 D^{\mathrm{ORG}}_{ab}(\Psi) \equiv -\Big[&\Big\{n_a n_b\frac{\overline{\rho}^2}{\rho^2}(\overline{\tilde{\boldsymbol{\delta}}} + 2\overline{\beta} + \varpi - \overline{\tau}) - m_{(a}n_{b)}\frac{\overline{\rho}}{\rho}\frac{-\Delta}{2\Sigma}(\tilde{\boldsymbol{D}} + \rho - \overline{\rho})\Big\}(\overline{\tilde{\boldsymbol{\delta}}} + 4\overline{\beta} + 3\overline{\tau}) \\ &+ \Big\{-n_{(a}m_{b)}\frac{-\Delta}{2\Sigma}\frac{\overline{\rho}}{\rho}(\overline{\tilde{\boldsymbol{\delta}}} + 4\overline{\beta} - 2\varpi - \overline{\tau}) + m_a m_b\frac{\Delta^2}{4\Sigma^2}(\tilde{\boldsymbol{D}} - \overline{\rho})\Big\}(\tilde{\boldsymbol{D}} + 3\overline{\rho})\Big]\Delta^2\overline{\Psi} + [\mathrm{c.c.}]\,. \end{aligned} \tag{A.11}$$

Sano & Tagoshi (2014) and Keidl, Friedman, & Wiseman (2007) follow these definitions. On the other hand, in Keidl *et al.*; Shah *et al.*; Shah, Friedman, & Keidl (2010; 2011; 2012) a definition with different sign is used. If we denote their metric perturbation by h^{Shah}_{ab},

$$h^{\mathrm{Shah}}_{ab} = -D^{\mathrm{ORG}}_{ab}(\Psi). \tag{A.12}$$

A.2 Outcomes

A.2.1 Spin coefficients

We assume that we use the same Kinnersley tetrad, which is given in Teukolsky (1973), for example.

The spin coefficients which are calculated from the definition in Newman & Penrose (1962) with $(+---)$ signature metric and ones which are calculated from the definition in Sano

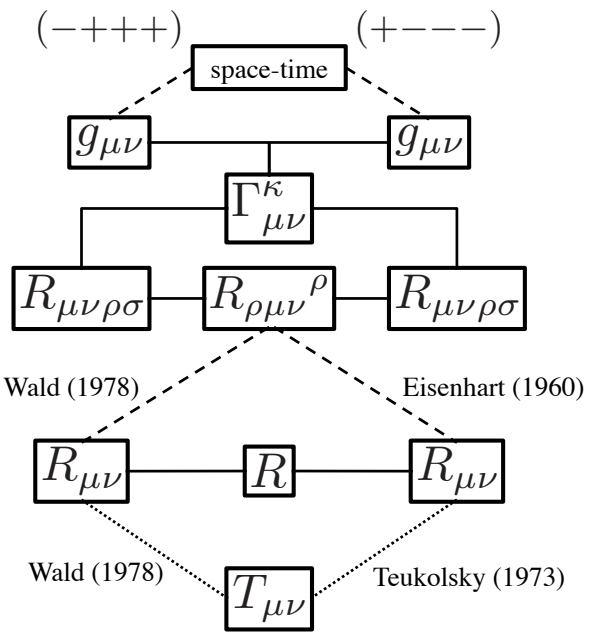

Figure A.1: Relations between values in two different conventions. For the same space-time, the values of the metric $g_{\mu\nu}$ differ by the convention of the signature. Accordingly, two "$g_{\mu\nu}$"s are put in different place in the figure. Dashed lines represent definitions which differ by the conventions. Solid lines represent the common definitions between the conventions. Though $g_{\mu\nu}$ differs between the two conventions, the Christoffel symbol $\Gamma^{\kappa}_{\mu\nu}$ agrees. Accordingly, only one "$\Gamma^{\kappa}_{\mu\nu}$" is put in the center column and is connected to the two "$g_{\mu\nu}$"s in both sides. The dotted lines represent the Einstein equations, which differ by the conventions because the value of energy-momentum tensor $T_{\mu\nu}$ does not depend on the conventions.

& Tagoshi (2014) with $(-+++)$ signature metric agree. For example, $\rho = -1/r$ for the Schwarzschild metric and the Kinnersley tetrad:

$$\rho_{\mathrm{ST}} = -l^{-}_{\mu;\nu} m^{\mu} \overline{m}^{\nu} = l^{+}_{\mu;\nu} m^{\mu} \overline{m}^{\nu} = \rho_{\mathrm{NP}}. \tag{A.13}$$

A.2.2 Weyl scalars and the Teukolsky equation

Assume that we use the definition of Riemann curvature tensor by Wald (1984). The Weyl scalars which are calculated from the definition in Teukolsky (1973) with $(+---)$ signature metric and ones which are calculated from the definition in Sano & Tagoshi (2014) with $(-+++)$ signature metric agree.

When it is the case, the Teukolsky equation agrees.

A.2.3 Einstein equation

The Einstein equation used by Teukolsky (1973) is $R_{ab} = -8\pi(T_{ab} - \frac{1}{2}g_{ab}T)$, where T_{ab} is the energy-momentum tensor and $T = T_{ab}g^{ab}$.

The Einstein equation in Wald (1984) is $R_{ab} = 8\pi(T_{ab} - \frac{1}{2}g_{ab}T)$. Namely,

$$-R_{ab}^{\text{Eisenhart}} = 8\pi\left(T_{ab} - \frac{1}{2}g^{+}_{ab}T^{+}\right), \tag{A.14}$$

$$= R_{ab}^{\text{Wald}} = 8\pi\left(T_{ab} - \frac{1}{2}g^{-}_{ab}T^{-}\right), \tag{A.15}$$

where

$$T^{+} \equiv T_{ab}g_{+}^{ab}, \quad T^{-} \equiv T_{ab}g_{-}^{ab}. \tag{A.16}$$

For the same space-time and the matter, the two equations agree because $T^{+} = -T^{-}$.

A.2.4 Hertz potential

While the relation between Ψ and h_{ab} is the same in Keidl, Friedman, & Wiseman (2007) and Sano & Tagoshi (2014), the convention of the signature of metric is different. Therefore, for a given perturbed space-time, the Hertz potentials in the two papers differs by sign:

$$\begin{aligned} h_{ab}^{\text{ST}} &= +D_{ab}^{\text{IRG}}(\Psi^{\text{ST}}), \\ &= -h_{ab}^{\text{Keidl+07}} = -D_{ab}^{\text{IRG}}(\Psi^{\text{Keidl+07}}). \end{aligned} \tag{A.17}$$

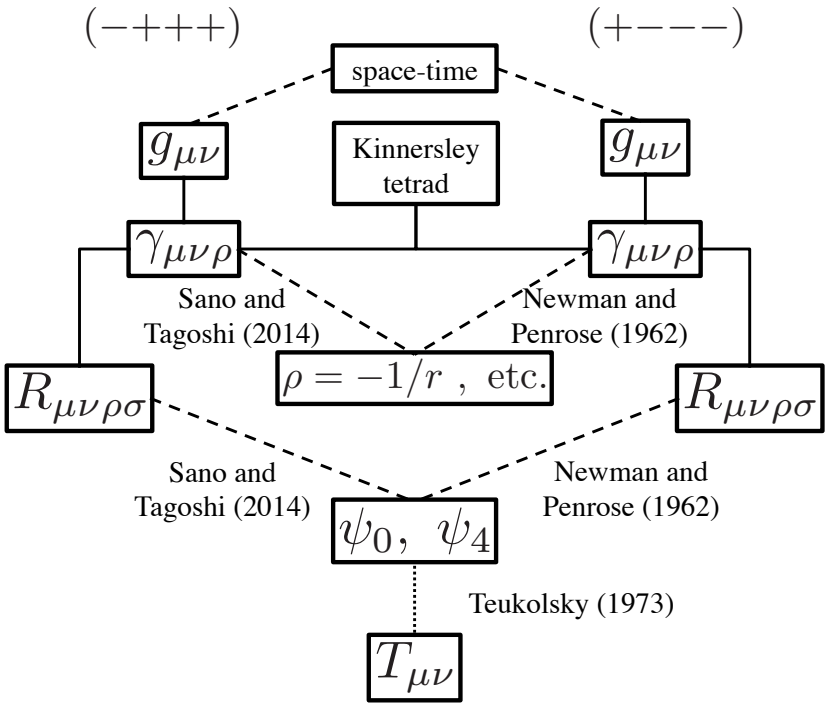

Figure A.2: The solid lines represent definitions which are common between two conventions. The dashed lines in the left half represent definitions which we use. The dashed lines in the right half are definitions which are used by Keidl *et al.* (2007), Teukolsky (1973), Newman and Penrose (1962), etc. There are two "$g_{\mu\nu}$"s in this figure because they are different by sign. Likewise, "$\gamma_{\mu\nu\rho}$" and "$R_{\mu\nu\rho\sigma}$" differ between the two conventions. In Sano and Tagoshi (2014), we used definitions of spin coefficients and Weyl scalars with different signs from those of Teukolsky (1973), so that the Teukolsky equation agrees. The dotted line represents the Teukolsky equation.

Appendix B

Verification of the Weyl scalars in the radiation gauge

Derivation of expressions for the perturbed Weyl scalars in the IRG.

The relations between the gauge-independent ψ_0, ψ_4 and the Hertz potential are important in the procedure of metric reconstruction, and are presented when CCK proposed the method. In Chrzanowski (1975), equations for perturbations of the Kerr metric are presented. In Cohen & Kegeles (1975) and Wald (1978), equations for vacuum type D space-time are presented. In Kegeles & Cohen (1979), they derived the equations for type D space-time using spinors. An additional term is there in the equation for ψ_4. The relations between the gauge-dependent ψ_1, ψ_2, and ψ_3 and the Hertz potential are not shown in Chrzanowski (1975). They are shown in Cohen & Kegeles (1975) and Kegeles & Cohen (1979). Stewart (1979) also derived formulae using spinor, and the results are presented in GHP notation (Geroch, Held, & Penrose 1973). He pointed out the missing term and overall factor $\frac{1}{2}$ in Cohen & Kegeles (1975). About 30 years later, Keidl, Friedman, & Wiseman (2007) again pointed out the error about the overall factor $\frac{1}{2}$ by CCK, and showed the first specific reconstruction for non-vacuum source. However, the equation for ψ_3 was found to be incorrect through our work, in the Schwarzschild case (Sano & Tagoshi 2014). In this section we summarize the relations. We assume the unperturbed

space-time is described by the Kerr metric and present the result in the IRG.

B.1 Commutation relations

The calculation needs a lot of labor even if we use some useful commutation relations in the Newman-Penrose formalism. Many commutation relations are available in "The Mathematical Theory of Black Holes" Chandrasekhar (1983). We present some useful relations for our calculation below (Not all relations are from Chandrasekhar's book). Arbitrary function of $(t,\ r,\ \theta,\ \phi)$ is denoted by F:

$$\boldsymbol{D}\rho F = \rho(\boldsymbol{D}+\rho)F, \qquad \boldsymbol{D}\beta F = \beta(\boldsymbol{D}+\overline{\rho})F, \tag{B.1a}$$

$$\boldsymbol{D}\varpi F = \varpi(\boldsymbol{D}+2\rho)F, \qquad \boldsymbol{D}\tau F = \tau(\boldsymbol{D}+\rho+\overline{\rho})F, \tag{B.1b}$$

$$\boldsymbol{\Delta}\rho F = \rho(\boldsymbol{\Delta}-\mu)F, \qquad \boldsymbol{\Delta}\mu F = \mu(\boldsymbol{\Delta}-\overline{\mu}-2\gamma)F, \tag{B.1c}$$

$$\boldsymbol{\delta}\rho F = \rho(\boldsymbol{\delta}+\tau)F, \quad \boldsymbol{\delta}\mu F = \mu(\boldsymbol{\delta}+2\tau-\overline{\varpi})F, \quad \boldsymbol{\delta}\varpi F = \varpi(\boldsymbol{\delta}+2\beta+2\tau)F, \tag{B.2a}$$

$$\overline{\boldsymbol{\delta}}\rho F = \rho(\overline{\boldsymbol{\delta}}-\varpi)F, \quad \overline{\boldsymbol{\delta}}\mu F = \mu(\overline{\boldsymbol{\delta}}-2\varpi+\overline{\tau})F, \quad \overline{\boldsymbol{\delta}}\varpi F = \varpi(\overline{\boldsymbol{\delta}}+2\overline{\beta}-2\varpi)F, \tag{B.2b}$$

$$\boldsymbol{\delta}\tau F = \tau(\boldsymbol{\delta}+2\beta+\tau-\overline{\varpi})F, \tag{B.2c}$$

$$(\boldsymbol{D}-\rho)(\boldsymbol{D}+\rho)F = \boldsymbol{D}\boldsymbol{D}F, \tag{B.3a}$$

$$\overline{\rho}(\boldsymbol{\delta}+2\beta-\tau)\frac{1}{\overline{\rho}}(\boldsymbol{\delta}+4\beta+\tau)F = \overline{\rho}(\boldsymbol{\delta}+2\beta)\frac{1}{\overline{\rho}}(\boldsymbol{\delta}+4\beta)F, \tag{B.3b}$$

$$(\boldsymbol{D}-\overline{\rho})\boldsymbol{\delta}F = \boldsymbol{\delta}\boldsymbol{D}F, \tag{B.4a}$$

$$\boldsymbol{D}(\boldsymbol{\delta}-\overline{\varpi})F = (\boldsymbol{\delta}-\overline{\varpi})(\boldsymbol{D}+\overline{\rho})F, \tag{B.4b}$$

$$(\boldsymbol{D}+\rho-\overline{\rho})(\boldsymbol{\delta}+\tau)F = (\boldsymbol{\delta}+\tau)(\boldsymbol{D}+\rho)F, \tag{B.4c}$$

$$(\boldsymbol{D}-\rho-\overline{\rho})(\boldsymbol{\delta}-\tau)F = (\boldsymbol{\delta}-\tau)(\boldsymbol{D}-\rho)F, \tag{B.4d}$$

$$(\boldsymbol{D}-\rho)(\boldsymbol{\delta}-\tau-\overline{\varpi})F = (\boldsymbol{\delta}-\tau-\overline{\varpi})(\boldsymbol{D}-\rho+\overline{\rho})F, \tag{B.4e}$$

$$(\boldsymbol{\Delta}+\overline{\mu})\boldsymbol{\delta}F=(\boldsymbol{\delta}+\overline{\varpi}-\tau)\boldsymbol{\Delta}F, \tag{B.5a}$$

$$\boldsymbol{\Delta}(\boldsymbol{\delta}-\overline{\varpi})F=(\boldsymbol{\delta}-\tau)(\boldsymbol{\Delta}-\overline{\mu})F, \tag{B.5b}$$

$$(\boldsymbol{\Delta}-\mu+\overline{\mu})(\boldsymbol{\delta}+\tau)F=(\boldsymbol{\delta}+\overline{\varpi})(\boldsymbol{\Delta}-\mu)F, \tag{B.5c}$$

$$(\boldsymbol{\Delta}+\mu+\overline{\mu})(\boldsymbol{\delta}-\tau)F=(\boldsymbol{\delta}-2\tau+\overline{\varpi})(\boldsymbol{\Delta}+\mu)F, \tag{B.5d}$$

$$(\boldsymbol{\Delta}+\mu)(\boldsymbol{\delta}-\tau-\overline{\varpi})F=(\boldsymbol{\delta}-2\tau)(\boldsymbol{\Delta}+\mu-\overline{\mu})F, \tag{B.5e}$$

$$(\boldsymbol{D}-\overline{\rho})(\boldsymbol{\delta}-2\beta)F=(\boldsymbol{\delta}-2\beta)\boldsymbol{D}F, \tag{B.6a}$$

$$(\boldsymbol{\Delta}+\mu+2\gamma)(\overline{\boldsymbol{\delta}}+2\alpha)F=(\overline{\boldsymbol{\delta}}+2\alpha+\varpi-\overline{\tau})(\boldsymbol{\Delta}+2\gamma)F, \tag{B.6b}$$

$$(\boldsymbol{D}-\overline{\rho}+\rho)\boldsymbol{\Delta}F+(\overline{\boldsymbol{\delta}}-2\alpha-\overline{\tau})\boldsymbol{\delta}F=(\boldsymbol{\delta}+2\beta+\tau)\overline{\boldsymbol{\delta}}F+(\boldsymbol{\Delta}-2\gamma)\boldsymbol{D}F, \tag{B.6c}$$

$$\begin{aligned}\boldsymbol{D}\boldsymbol{\Delta}F&=(\tilde{\boldsymbol{\Delta}}-\gamma-\overline{\gamma})\tilde{\boldsymbol{D}}F,\\ \boldsymbol{\delta}\overline{\boldsymbol{\delta}}F&=(\tilde{\overline{\boldsymbol{\delta}}}-\varpi-\overline{\tau})\tilde{\boldsymbol{\delta}}F,\end{aligned} \tag{B.7}$$

$$\varpi\overline{\rho}=\overline{\tau}\rho,\quad \varpi\overline{\mu}=\overline{\tau}\mu,\quad \overline{\tau}=-\tau,\quad \gamma-\overline{\gamma}=\mu-\overline{\mu},\quad 8\beta\tau+(\rho-\overline{\rho})\overline{\rho}=0, \tag{B.8}$$

$$\mu\boldsymbol{D}+\rho\boldsymbol{\Delta}=\rho\left(\frac{r^2+a^2}{\Sigma}\partial_t+\frac{a}{\Sigma}\partial_\phi\right). \tag{B.9}$$

B.2 Relations between the Weyl scalars and the metric perturbation

By using Eq. (B.3), the each component of the metric perturbation in the IRG is

$$h_{22}=h_{22}^{\overline{\Psi}}+h_{22}^{\Psi}, \tag{B.10a}$$

$$h_{22}^{\overline{\Psi}}\equiv-(\overline{\boldsymbol{\delta}}+2\overline{\beta}+\varpi+2\overline{\tau})(\overline{\boldsymbol{\delta}}+4\overline{\beta})\overline{\Psi},\quad h_{22}^{\Psi}\equiv-(\boldsymbol{\delta}+2\beta+\overline{\varpi}+2\tau)(\boldsymbol{\delta}+4\beta)\Psi, \tag{B.10b}$$

$$h_{23}=-(\boldsymbol{D}+\overline{\rho})(\overline{\boldsymbol{\delta}}+4\overline{\beta})\overline{\Psi}+(\varpi-\overline{\tau})\boldsymbol{D}\overline{\Psi},\quad h_{24}=\overline{h_{23}}, \tag{B.10c}$$

$$h_{33}=-(\boldsymbol{D}+2\overline{\rho})\boldsymbol{D}\overline{\Psi},\quad h_{44}=\overline{h_{33}}. \tag{B.10d}$$

We substitute them into the expressions for the perturbed Weyl scalars in terms of the metric perturbation $h_{\mu\nu}$.

We start with

$$-2C_{abcd} = \nabla_d\nabla_b h_{ac} + \nabla_c\nabla_a h_{bd} - \nabla_d\nabla_a h_{bc} - \nabla_c\nabla_b h_{ad} + C^{(0)}_{aecd}h^e{}_b - C^{(0)}_{becd}h^e{}_a, \tag{B.11}$$

where C_{abcd} and $C^{(0)}_{abcd}$ are the first order perturbation and the unperturbed part of the Weyl tensor, respectively. This equation is given in Kegeles & Cohen (1979), with different sign. See Appendix A for different definitions and conventions. Among independent components of $C^{(0)}_{abcd}$, non-zero components are $C^{(0)}_{1342} = \Psi_2$ and $C^{(0)}_{1212} = C^{(0)}_{3434} = -2\mathrm{Re}(\Psi_2)$.

Therefore we obtain

$$-2\psi_0 = h_{11;33} + h_{33;11} - h_{31;13} - h_{13;31}, \tag{B.12a}$$

$$-2\psi_1 = h_{11;23} + h_{23;11} - h_{21;13} - h_{13;21} - C^{(0)}_{2413}h^4{}_1, \tag{B.12b}$$

$$-2\psi_2 = h_{14;32} + h_{32;14} - h_{34;12} - h_{12;34} + C^{(0)}_{1342}h^3{}_3 - C^{(0)}_{3142}h^1{}_1, \tag{B.12c}$$

$$-2\psi_3 = h_{22;14} + h_{14;22} - h_{12;24} - h_{24;12} - C^{(0)}_{1324}h^3{}_2, \tag{B.12d}$$

$$-2\psi_4 = h_{22;44} + h_{44;22} - h_{42;24} - h_{24;42}. \tag{B.12e}$$

We use the following equation to calculate each term:

$$\begin{aligned} h_{\mu\nu;\rho\sigma} = {} & (h_{\mu\nu,\rho} + 2h_{\kappa(\mu}\gamma^{\kappa}{}_{\nu)\rho})_{,\sigma} \\ & + (h_{\lambda\mu,\rho} + 2h_{\kappa(\lambda}\gamma^{\kappa}{}_{\mu)\rho})\gamma^{\lambda}{}_{\nu\sigma} + (h_{\lambda\nu,\rho} + 2h_{\kappa(\lambda}\gamma^{\kappa}{}_{\nu)\rho})\gamma^{\lambda}{}_{\mu\sigma} + (h_{\mu\nu,\lambda} + 2h_{\kappa(\mu}\gamma^{\kappa}{}_{\nu)\lambda})\gamma^{\lambda}{}_{\rho\sigma}, \end{aligned} \tag{B.13}$$

where $\gamma_{\rho\mu\nu}$ is the Ricci rotation coefficient, which is defined in Eq. (2.5).

B.3 Second derivatives of the metric perturbation

By using Eq. (B.13), we can obtain components of second derivatives of h_{ab}, in terms of directional derivatives $\boldsymbol{D}$, $\boldsymbol{\Delta}$, $\boldsymbol{\delta}$, $\overline{\boldsymbol{\delta}}$ and spin coefficients. In equations below, h_{12} and h_{34} are

dropped because they are zero both in the IRG and the ORG:

$$h_{11;33} = (\boldsymbol{\delta} - 2\beta - \overline{\varpi})(\boldsymbol{\delta} - 2\overline{\varpi})h_{11} + 4\overline{\rho}(\boldsymbol{\delta} - 2\beta - \overline{\varpi})h_{13} + 2\overline{\rho}^2 h_{33}, \tag{B.14a}$$

$$h_{22;44} = (\overline{\boldsymbol{\delta}} + 2\alpha + \varpi)(\overline{\boldsymbol{\delta}} + 2\varpi)h_{22} - 4\overline{\mu}(\overline{\boldsymbol{\delta}} + 2\alpha + \overline{\tau})h_{24} + 2\overline{\mu}^2 h_{44}, \tag{B.14b}$$

$$h_{33;11} = 2\overline{\varpi}^2 h_{11} - 4\overline{\varpi}(\boldsymbol{D} + \overline{\rho})h_{13} + \boldsymbol{D}\boldsymbol{D}h_{33}, \tag{B.14c}$$

$$h_{44;22} = 2\overline{\tau}^2 h_{22} + 4\overline{\tau}(\boldsymbol{\Delta} - \overline{\mu} + 2\gamma)h_{24} + (\boldsymbol{\Delta} + 3\gamma - \overline{\gamma})(\boldsymbol{\Delta} + 2\gamma - 2\overline{\gamma})h_{44}, \tag{B.14d}$$

$$h_{31;13} = -(\boldsymbol{\delta} - 2\beta - \overline{\varpi})\overline{\varpi}h_{11} + \boldsymbol{D}(\boldsymbol{\delta} - 2\beta - \overline{\varpi})h_{13} + \boldsymbol{D}\overline{\rho}h_{33}, \tag{B.15a}$$

$$h_{42;24} = (\overline{\boldsymbol{\delta}} + 2\alpha + \varpi)\overline{\tau}h_{22} + (\boldsymbol{\Delta} + 3\gamma - \overline{\gamma})(\overline{\boldsymbol{\delta}} + 2\alpha + \overline{\tau})h_{24} - (\boldsymbol{\Delta} + 3\gamma - \overline{\gamma})\overline{\mu}h_{44}, \tag{B.15b}$$

$$h_{13;31} = h_{31;13}, \tag{B.15c}$$

$$h_{24;42} = h_{42;24}, \tag{B.15d}$$

$$\begin{aligned} h_{11;23} &= (\boldsymbol{\delta} - \overline{\varpi})(\boldsymbol{\Delta} - \mu - 2\gamma - 2\overline{\gamma})h_{11} + 2\tau\mu h_{11} \\ &\quad + 2\overline{\rho}\overline{\tau}h_{33} + 2(\boldsymbol{\delta} - \overline{\varpi})(\overline{\tau}h_{13} + \tau h_{14}) + 2\overline{\rho}(\boldsymbol{\Delta} - \mu - 2\gamma)h_{13}, \end{aligned} \tag{B.16a}$$

$$\begin{aligned} h_{22;14} &= (\overline{\boldsymbol{\delta}} + \varpi)(\boldsymbol{D} + \rho)h_{22} + 2\varpi\rho h_{22} \\ &\quad + 2\overline{\mu}\overline{\varpi}h_{44} - 2(\overline{\boldsymbol{\delta}} + \varpi)(\varpi h_{23} + \overline{\varpi}h_{24}) - 2\overline{\mu}(\boldsymbol{D} + \rho)h_{24}, \end{aligned} \tag{B.16b}$$

$$h_{23;11} = -2\varpi(\boldsymbol{D} + \rho)h_{33} + 2\overline{\varpi}(\varpi h_{13} + \overline{\varpi}h_{14}) + \boldsymbol{D}\boldsymbol{D}h_{23} + 2\overline{\varpi}\varpi h_{13}, \tag{B.16c}$$

$$h_{14;22} = 2\tau(\boldsymbol{\Delta} + \mu - 2\overline{\mu})h_{44} + 2\overline{\tau}(\tau h_{24} + \overline{\tau}h_{23}) + (\boldsymbol{\Delta} + \mu - \overline{\mu})(\boldsymbol{\Delta} - 2\overline{\gamma})h_{14} + 2\overline{\tau}\tau h_{24}, \tag{B.16d}$$

$$h_{21;13} = \overline{\varpi}\mu h_{11} - \varpi\overline{\rho}h_{33} - \mu(\boldsymbol{D} + \overline{\rho})h_{13} - (\boldsymbol{\delta} - \overline{\varpi})(\varpi h_{13} + \overline{\varpi}h_{14}) + \boldsymbol{D}\overline{\rho}h_{23}, \tag{B.17a}$$

$$\begin{aligned} h_{12;24} &= \overline{\tau}\rho h_{22} - \tau\overline{\mu}h_{44} \\ &\quad + \rho(\boldsymbol{\Delta} - \overline{\mu} + 2\gamma)h_{24} + (\overline{\boldsymbol{\delta}} + \varpi)(\tau h_{24} + \overline{\tau}h_{23}) - (\boldsymbol{\Delta} + \mu - \overline{\mu})\overline{\mu}h_{14}, \end{aligned} \tag{B.17b}$$

$$\begin{aligned} h_{13;21} &= -\overline{\varpi}(\boldsymbol{\Delta} - \overline{\mu} - 2\gamma - 2\overline{\gamma})h_{11} + (\boldsymbol{D} - \rho)\overline{\tau}h_{33} \\ &\quad - 2\overline{\varpi}(\tau h_{14} + \overline{\tau}h_{13}) + \boldsymbol{D}(\boldsymbol{\Delta} - 2\gamma)h_{13} - \overline{\varpi}(\overline{\boldsymbol{\delta}} - 2\alpha)h_{13} - \varpi(\boldsymbol{\delta} - 2\beta)h_{13}, \end{aligned} \tag{B.17c}$$

$$\begin{aligned} h_{24;12} &= \overline{\tau}(\boldsymbol{D} + \overline{\rho})h_{22} - (\boldsymbol{\Delta} + 2\mu - \overline{\mu})\overline{\varpi}h_{44} \\ &\quad + 2\tau(\varpi h_{23} + \overline{\varpi}h_{24}) + (\boldsymbol{\Delta} + \mu - \overline{\mu})\boldsymbol{D}h_{24} - \tau(\boldsymbol{\delta} - 2\overline{\alpha})h_{24} - \overline{\tau}(\overline{\boldsymbol{\delta}} - 2\overline{\beta})h_{24}, \end{aligned} \tag{B.17d}$$

$$h_{12;34} = -\mu(\overline{\boldsymbol{\delta}} - 2\alpha - \varpi)h_{13} + (\overline{\boldsymbol{\delta}} + 2\overline{\beta})\overline{\rho}h_{23}$$
$$- \overline{\mu}(\boldsymbol{\delta} - 2\overline{\alpha} - \overline{\varpi})h_{14} + (\boldsymbol{\delta} + 2\beta)\rho h_{24} + \overline{\mu}\mu h_{11} + \rho\overline{\rho}h_{22}, \tag{B.18a}$$
$$h_{34;12} = [-\varpi(\boldsymbol{\Delta} - \mu - 2\gamma)h_{13} + \overline{\tau}(\boldsymbol{D} + \overline{\rho})h_{23} - \overline{\tau}\varpi h_{33}] + \text{c.c.}, \tag{B.18b}$$
$$h_{32;14} = \boldsymbol{D}(\overline{\boldsymbol{\delta}} + 2\overline{\beta} - \varpi)h_{23} + \boldsymbol{D}\rho h_{22}$$
$$- 2\rho\overline{\varpi}h_{24} - (\overline{\boldsymbol{\delta}} + 2\overline{\beta} - \varpi)\varpi h_{33} + 2\overline{\mu}(\varpi h_{13} + \overline{\varpi}h_{14}), \tag{B.18c}$$
$$h_{14;32} = (\boldsymbol{\Delta} - \gamma - \overline{\gamma})(\boldsymbol{\delta} - 2\overline{\alpha} + \tau)h_{14} - (\boldsymbol{\Delta} - \gamma - \overline{\gamma})\mu h_{11} - 2\overline{\tau}\mu h_{13}$$
$$+ 2\overline{\rho}(\overline{\tau}h_{23} + \tau h_{24}) + (\boldsymbol{\delta} + 2\beta - \overline{\varpi})\tau h_{44}. \tag{B.18d}$$

B.4 Reduced expressions for the Weyl scalars

We substitute the expressions of $h_{\mu\nu;\rho\sigma}$ in the previous section into Eq. (B.12). When we use the IRG, since $h_{11} = h_{13} = h_{14} = 0$, many terms vanish in equation for ψ_0. On the other hand, equation fro ψ_4 become very complicated. In this section, we discuss the relation between what we obtained with the results that are presented in Stewart (1979) and Keidl, Friedman, & Wiseman (2007).

For ψ_0, we have

$$\begin{aligned} 2\psi_0 &= -2\overline{\rho}^2 h_{33} - \boldsymbol{D}\boldsymbol{D}h_{33} + 2\boldsymbol{D}\overline{\rho}h_{33} \\ &= -(\boldsymbol{D} - 2\overline{\rho})\boldsymbol{D}h_{33} \\ &= (\boldsymbol{D} - \overline{\rho})(\boldsymbol{D} - \overline{\rho})(\boldsymbol{D} - \overline{\rho})(\boldsymbol{D} + 3\overline{\rho})\overline{\Psi} \\ &= \boldsymbol{D}\boldsymbol{D}\boldsymbol{D}\boldsymbol{D}\overline{\Psi}. \end{aligned} \tag{B.19}$$

This is consistent with Eq. (4.27) in Stewart (1979) and Eq. (95) in Keidl, Friedman, & Wiseman (2007).

For ψ_1, in a similar manner as ψ_0, we have

$$\begin{aligned} 2\psi_1 &= -2\overline{\rho\tau}h_{33} + 2\varpi(\boldsymbol{D}+\rho)h_{33} - \boldsymbol{D}\boldsymbol{D}h_{23} - \varpi\overline{\rho}h_{33} + \boldsymbol{D}\overline{\rho}h_{23} + (\boldsymbol{D}-\rho)\overline{\tau}h_{33} \\ &= (2\varpi+\overline{\tau})(\boldsymbol{D}+\rho-\overline{\rho})h_{33} - \boldsymbol{D}(\boldsymbol{D}-\overline{\rho})h_{23} \\ &= \boldsymbol{D}\boldsymbol{D}\boldsymbol{D}(\overline{\boldsymbol{\delta}}+4\overline{\beta})\overline{\Psi} - 3\varpi\boldsymbol{D}(\boldsymbol{D}+2\rho)\boldsymbol{D}\overline{\Psi}. \end{aligned} \tag{B.20}$$

We prefer this form because $(\overline{\boldsymbol{\delta}}+4\overline{\beta}) = (\rho/\sqrt{2})\eth^{-}_{(2)}$ is isolated in the first term. Our result is consistent with Eq. (4.27) in Stewart (1979) and Eq. (96) in Keidl, Friedman, & Wiseman (2007),

$$\begin{aligned} 8\psi_1 = -2(\boldsymbol{D}+\rho-\overline{\rho})(\boldsymbol{D}+\rho-\overline{\rho})h_{23} \\ - (\boldsymbol{D}+\rho-\overline{\rho})(\overline{\boldsymbol{\delta}}-2\alpha+2\overline{\beta}-2\varpi-\overline{\tau})h_{33} \\ - (\overline{\boldsymbol{\delta}}-3\alpha+\overline{\beta}-3\varpi-\overline{\tau})(\boldsymbol{D}-\overline{\rho})h_{33}. \end{aligned} \tag{B.21}$$

For ψ_2, in a similar manner as ψ_0 and ψ_1, we have

$$\begin{aligned} 2\psi_2 &= -2\overline{\rho}(\overline{\tau}h_{23}+\tau h_{24}) - (\boldsymbol{\delta}+2\beta-\overline{\varpi})\tau h_{44} \\ &\quad - \boldsymbol{D}(\overline{\boldsymbol{\delta}}+2\overline{\beta}-\varpi)h_{23} - \boldsymbol{D}(\rho h_{22}) + 2\rho\overline{\varpi}h_{24} + (\overline{\boldsymbol{\delta}}+2\overline{\beta}-\varpi)\varpi h_{33} \\ &\quad + \overline{\tau}(\boldsymbol{D}+\overline{\rho})h_{23} - \overline{\tau}\varpi h_{33} + \tau(\boldsymbol{D}+\rho)h_{24} - \tau\overline{\varpi}h_{44} \\ &\quad + (\overline{\boldsymbol{\delta}}+2\overline{\beta})\overline{\rho}h_{23} + (\boldsymbol{\delta}+2\beta)\rho h_{24} + \rho\overline{\rho}h_{22} \\ &= -(\boldsymbol{D}-\overline{\rho})\rho h_{22} - \boldsymbol{D}(\overline{\boldsymbol{\delta}}+2\overline{\beta}-\varpi)h_{23} - 2\overline{\rho\tau}h_{23} + (\overline{\boldsymbol{\delta}}+2\overline{\beta}-\varpi)(\varpi+\overline{\tau})h_{33} \\ &\quad + \overline{\tau}(\boldsymbol{D}+\overline{\rho})h_{23} + (\overline{\boldsymbol{\delta}}+2\overline{\beta})\overline{\rho}h_{23} - (\overline{\boldsymbol{\delta}}+2\overline{\beta})\overline{\tau}h_{33} \\ &\quad + \tau(\boldsymbol{D}+\rho)h_{24} + (\boldsymbol{\delta}+2\beta)\rho h_{24} - (\boldsymbol{\delta}+2\beta)\tau h_{44} \\ &= \boldsymbol{D}\boldsymbol{D}\rho(\overline{\boldsymbol{\delta}}+2\overline{\beta})\frac{1}{\rho}(\overline{\boldsymbol{\delta}}+4\overline{\beta})\overline{\Psi} - 4\varpi(\boldsymbol{D}+\rho)\boldsymbol{D}(\overline{\boldsymbol{\delta}}+4\overline{\beta})\overline{\Psi} + 6\varpi\boldsymbol{D}\varpi\boldsymbol{D}\overline{\Psi}. \end{aligned} \tag{B.22}$$

In this form, $\rho(\overline{\boldsymbol{\delta}}+2\overline{\beta})\rho^{-1}(\overline{\boldsymbol{\delta}}+4\overline{\beta}) = (\rho^2/2)\eth^{-}_{(1)}\eth^{-}_{(2)}$ and $(\overline{\boldsymbol{\delta}}+4\overline{\beta}) = (\rho/\sqrt{2})\eth^{-}_{(2)}$ are isolated in the

first and second term, respectively. Our result is consistent with Eq. (4.27) in Stewart (1979),

$$\begin{aligned}12\psi_2 = &-(\boldsymbol{D}+2\rho-\overline{\rho})(\boldsymbol{D}+2\rho-\overline{\rho})h_{22}^{\overline{\Psi}} - 2(\boldsymbol{D}+2\rho-\overline{\rho})(\overline{\boldsymbol{\delta}}+2\overline{\beta}-\varpi-\overline{\tau})h_{23}\\ &- 2(\overline{\boldsymbol{\delta}}+2\overline{\beta}-3\varpi-\overline{\tau})(\boldsymbol{D}+\rho-\overline{\rho})h_{23} - (\overline{\boldsymbol{\delta}}+2\overline{\beta}-3\varpi-\overline{\tau})(\overline{\boldsymbol{\delta}}+4\overline{\beta}-4\varpi-\overline{\tau})h_{33}\\ &- (\boldsymbol{D}+2\rho-\overline{\rho})(\boldsymbol{D}+2\rho-\overline{\rho})h_{22}^{\Psi} + (\boldsymbol{\delta}+2\beta+2\tau)(\boldsymbol{D}+2\rho-2\overline{\rho})h_{24}\\ &+ (\boldsymbol{D}+2\rho-\overline{\rho})(\boldsymbol{\delta}+2\beta+2\overline{\varpi}+2\tau)h_{24} - (\boldsymbol{\delta}+2\beta+2\tau)(\boldsymbol{\delta}+4\beta-\overline{\varpi}+2\tau)h_{44}. \quad \text{(B.23)}\end{aligned}$$

The last four terms are proportional to Ψ. The sum of these four terms vanish. Then the equation becomes Eq. (97) in Keidl, Friedman, & Wiseman (2007).

For ψ_3, we have

$$\begin{aligned}2\psi_3 = &-\boldsymbol{D}(\overline{\boldsymbol{\delta}}+\varpi-\overline{\tau})h_{22} + (\boldsymbol{\Delta}+\mu+\overline{\mu})(\boldsymbol{D}+\rho)h_{24}\\ &- 2(\overline{\tau}-\overline{\varpi})(\overline{\boldsymbol{\delta}}-2\overline{\beta}+\varpi)h_{24} - \tau(\boldsymbol{\delta}+2\beta+3\overline{\tau})h_{24} - (\rho-\overline{\rho})\overline{\rho}h_{24}\\ &- 2\varpi^2 h_{23} - (\tau-2\varpi)(\overline{\boldsymbol{\delta}}+2\overline{\beta}+\tau)h_{23} - (2\tau+\overline{\varpi})(\boldsymbol{\Delta}+\mu-\overline{\mu})h_{44}. \quad \text{(B.24)}\end{aligned}$$

By considering the Schwarzschild case $\varpi = \tau = 0$, $\rho = \overline{\rho}$, we have

$$2\psi_3 = \boldsymbol{D}\overline{\boldsymbol{\delta}}(\overline{\boldsymbol{\delta}}+2\overline{\beta})(\overline{\boldsymbol{\delta}}+4\overline{\beta})\overline{\Psi} + 6\gamma\boldsymbol{D}\rho(\boldsymbol{\delta}+4\beta)\Psi, \quad \text{(B.25)}$$

and find that Eq. (98) in Keidl, Friedman, & Wiseman (2007),

$$\begin{aligned}8\psi_3^{(\text{Keidl+07})} &= -(\boldsymbol{D}+3\rho-\overline{\rho})(\overline{\boldsymbol{\delta}}+2\alpha+2\overline{\beta}-\overline{\tau})h_{22}^{\overline{\Psi}} - (\overline{\boldsymbol{\delta}}+\alpha+\overline{\beta}-\varpi-\overline{\tau})(\boldsymbol{D}+2\rho-\overline{\rho})h_{22}^{\overline{\Psi}}\\ &\quad - 2(\overline{\boldsymbol{\delta}}+\alpha+\overline{\beta}-\varpi-\overline{\tau})(\overline{\boldsymbol{\delta}}+2\overline{\beta}-\varpi-\overline{\tau})h_{23}\\ &= \boldsymbol{D}\overline{\boldsymbol{\delta}}(\overline{\boldsymbol{\delta}}+2\overline{\beta})(\overline{\boldsymbol{\delta}}+4\overline{\beta})\overline{\Psi}\end{aligned} \quad \text{(B.26)}$$

is not consistent with our result. There is not a term proportional to Ψ in their equation. The second equality holds for the Schwarzschild case. If we use the expression by Keidl, Friedman, & Wiseman (2007) instead, ψ_3 derived from $\Psi = \Psi_{\rm P} + \Psi_{\rm H}$ fails to become smooth on the surface $r = r_0$. On the other hand, it is likely that there are typos in Eq. (4.27) of

Stewart (1979). If we "correct" them by $(D_{31}{\delta'_{01}}^2\delta_{0-3} \to D_{31}{\delta'_{01}}^2\delta'_{0-3})$ in the first term and $(\chi \to \overline{\chi})$ after first bracket [ ], the expression becomes identical to Eq. (98) of Keidl, Friedman, & Wiseman (2007), apart from the lack of terms proportional to Ψ:

$$\begin{aligned}
8\psi_3^{(\mathrm{Stewart79})} = &-(\boldsymbol{D}+3\rho-\overline{\rho})(\overline{\boldsymbol{\delta}}+2\alpha+2\overline{\beta}-\overline{\tau})h_{22} - (\overline{\boldsymbol{\delta}}+\alpha+\overline{\beta}-\varpi-\overline{\tau})(\boldsymbol{D}+2\rho-\overline{\rho})h_{22} \\
&- 2(\overline{\boldsymbol{\delta}}+\alpha+\overline{\beta}-\varpi-\overline{\tau})(\overline{\boldsymbol{\delta}}+2\overline{\beta}-\varpi-\overline{\tau})h_{23} \\
&- \boldsymbol{\Delta}(\boldsymbol{\delta}+2\beta-2\overline{\alpha}+2\tau+\overline{\varpi})h_{44} - (\boldsymbol{\delta}+3\beta-\overline{\alpha}+3\tau+\overline{\varpi})(\boldsymbol{\Delta}+2\mu-\overline{\mu})h_{44} \\
&+ \boldsymbol{\Delta}(\boldsymbol{D}+2\rho-2\overline{\rho})h_{24} + (\boldsymbol{D}+3\rho-\overline{\rho})(\boldsymbol{\Delta}+2\overline{\mu}+2\gamma)h_{24} \\
&+ (\overline{\boldsymbol{\delta}}+\alpha+\overline{\beta}-\varpi-\overline{\tau})(\boldsymbol{\delta}+2\beta+2\tau+2\overline{\varpi})h_{24} + (\boldsymbol{\delta}+3\beta-\overline{\alpha}+3\tau+\overline{\varpi})(\overline{\boldsymbol{\delta}}+2\alpha-2\overline{\tau})h_{24}.
\end{aligned} \tag{B.27}$$

In order to check whether our result is consistent with the expression above, it is necessary to use Eq. (3.3), the condition that the Hertz potential satisfies the source-free perturbation equation for $\psi_{(s=-2)}$.

For ψ_4, we have

$$\begin{aligned}
2\psi_4 = &-(\overline{\boldsymbol{\delta}}+2\alpha+\varpi)(\overline{\boldsymbol{\delta}}+2\varpi)h_{22} + 2(\overline{\boldsymbol{\delta}}+2\alpha+\varpi-\overline{\tau})\overline{\tau}h_{22} \\
&+ 4(\overline{\boldsymbol{\delta}}+2\alpha+\varpi-\overline{\tau})\overline{\mu}h_{24} + 2(\boldsymbol{\Delta}+3\gamma-\overline{\gamma})(\overline{\boldsymbol{\delta}}+2\alpha+\overline{\tau})h_{24} - 4(\boldsymbol{\Delta}+\mu+2\gamma)\overline{\tau}h_{24} \\
&- (\boldsymbol{\Delta}+3\gamma-\overline{\gamma})(\boldsymbol{\Delta}+2\gamma-2\overline{\gamma})h_{44} - 2(\boldsymbol{\Delta}+\mu+2\gamma)\overline{\mu}h_{44}.
\end{aligned} \tag{B.28}$$

This is consistent with Eq. (4.27) in Stewart (1979),

$$\begin{aligned}
2\psi_4 = &-(\overline{\boldsymbol{\delta}}+3\alpha+\overline{\beta}-\overline{\tau})(\overline{\boldsymbol{\delta}}+2\alpha+2\overline{\beta}-\overline{\tau})h_{22} - (\boldsymbol{\Delta}+\mu+2\gamma)(\boldsymbol{\Delta}+2\mu-\overline{\mu})h_{44} \\
&+ (\boldsymbol{\Delta}+\mu+2\gamma)(\overline{\boldsymbol{\delta}}+2\alpha-2\overline{\tau})h_{24} + (\overline{\boldsymbol{\delta}}+3\alpha+\overline{\beta}-\overline{\tau})(\boldsymbol{\Delta}+2\overline{\mu}+2\gamma)h_{24}.
\end{aligned} \tag{B.29}$$

In order to check whether our result is consistent with the expression by Keidl, Friedman, & Wiseman (2007), it is necessary to use Eq. (3.3). In the Schwarzschild case, our expression can be reduced to

$$2\psi_4 = (\overline{\boldsymbol{\delta}}-2\overline{\beta})\overline{\boldsymbol{\delta}}(\overline{\boldsymbol{\delta}}+2\overline{\beta})(\overline{\boldsymbol{\delta}}+4\overline{\beta})\overline{\Psi} - 6\gamma\rho^2\partial_t\Psi, \tag{B.30}$$

which is consistent with Eq. (99) of Keidl, Friedman, & Wiseman (2007),

$$2\psi_4 = (\overline{\boldsymbol{\delta}} + 3\alpha + \overline{\beta} - \overline{\tau})(\overline{\boldsymbol{\delta}} + 2\alpha + 2\overline{\beta} - \overline{\tau})(\overline{\boldsymbol{\delta}} + \alpha + 3\overline{\beta} - \overline{\tau})(\overline{\boldsymbol{\delta}} + 4\overline{\beta} + 3\overline{\tau})\overline{\Psi} + 3\Psi_2 \left[\tau(\overline{\boldsymbol{\delta}} + 4\alpha) - \rho(\boldsymbol{\Delta} + 4\gamma) - \mu\boldsymbol{D} + \varpi(\boldsymbol{\delta} + 4\beta) + 2\Psi_2\right] \Psi. \quad \text{(B.31)}$$

Without imposing $a = 0$, the first term becomes

$$\begin{aligned}(\overline{\boldsymbol{\delta}} + 3\alpha + \overline{\beta} - \overline{\tau})(\overline{\boldsymbol{\delta}} + 2\alpha + 2\overline{\beta} - \overline{\tau})(\overline{\boldsymbol{\delta}} + \alpha + 3\overline{\beta} - \overline{\tau})(\overline{\boldsymbol{\delta}} + 4\overline{\beta} + 3\overline{\tau})\overline{\Psi} \\ = \rho^3(\overline{\boldsymbol{\delta}} - 2\overline{\beta} - \overline{\tau})\frac{1}{\rho}(\overline{\boldsymbol{\delta}} - \overline{\tau})\frac{1}{\rho}(\overline{\boldsymbol{\delta}} + 2\overline{\beta} - \overline{\tau})\frac{1}{\rho}(\overline{\boldsymbol{\delta}} + 4\overline{\beta} + 3\overline{\tau})\overline{\Psi} \\ = \rho^3(\overline{\boldsymbol{\delta}} - 2\overline{\beta})\frac{1}{\rho}\overline{\boldsymbol{\delta}}\frac{1}{\rho}(\overline{\boldsymbol{\delta}} + 2\overline{\beta})\frac{1}{\rho}(\overline{\boldsymbol{\delta}} + 4\overline{\beta})\overline{\Psi}.\end{aligned} \quad \text{(B.32)}$$

Further, in the stationary and axisymmetric case, the second term becomes zero:

$$\begin{aligned}[\tau(\overline{\boldsymbol{\delta}} + 4\alpha) - \rho(\boldsymbol{\Delta} + 4\gamma) - \mu\boldsymbol{D} + \varpi(\boldsymbol{\delta} + 4\beta) + 2\Psi_2]\Psi \\ = [4\tau\alpha - 4\rho\gamma + 4\varpi\beta + 2\Psi_2]\,\Psi \\ = [4\tau\alpha - 4\rho\gamma + 4\varpi\beta + 4\gamma\rho - 4(2\alpha - \varpi)\tau]\,\Psi \\ = 0.\end{aligned} \quad \text{(B.33)}$$

Appendix C

Gravitational fields in terms of the Hertz potential

In this chapter we show expressions in terms of the Hertz potential $\Psi_{\rm P}$, for some of the Weyl scalars and the metric perturbation.

Since the angular part of $\overline{\Psi_{\rm P}}$ is ${}_2Y_l(\theta)$, $\psi_1^{\rm P}$ can be written as

$$\psi_1^{\rm P} = \frac{1}{2}\sum_{l=2}^{\infty}\left[-\frac{1}{\sqrt{2}}\frac{\partial^3}{\partial r^3}\rho\overline{R_l^{\rm P}}\sqrt{(l+2)(l-1)}\ {}_1Y_l - 3\varpi\frac{\partial}{\partial r}\frac{1}{\rho^2}\frac{\partial}{\partial r}\rho^2\frac{\partial}{\partial r}\overline{R_l^{\rm P}}\ {}_2Y_l\right]. \tag{C.1}$$

This expression is obtained by substituting $\Psi = \Psi_{\rm P}$ into Eq. (3.8b). Because of the stationarity and axisymmetry, $\frac{\partial}{\partial t}$ and $\frac{\partial}{\partial \phi}$ in $\boldsymbol{D}$ and $\boldsymbol{\delta}$ are dropped. Thus $\boldsymbol{D} = \frac{\partial}{\partial r}$. And the derivative with respect to θ becomes the spin-weight lowering operator $\eth^-_{(2)}$, according to Eq. (2.22b). And then the operator changes ${}_2Y_l$ to ${}_1Y_l$, according to Eq. (2.19b). In a similar manner, expressions for $\psi_2^{\rm P}$, $h_{22}^{\rm P}$, and $h_{23}^{\rm P}$ are obtained:

$$\psi_2^{\rm P} = \frac{1}{2}\sum_{l=2}^{\infty}\left[\frac{1}{2}\frac{\partial^2}{\partial r^2}\rho^2\overline{R_l^{\rm P}}\sqrt{(l+2)(l-1)(l+1)l}\ {}_0Y_l \right.$$
$$\left. +\frac{4}{\sqrt{2}}\frac{\varpi}{\rho}\frac{\partial}{\partial r}\rho\frac{\partial}{\partial r}\rho\overline{R_l^{\rm P}}\sqrt{(l+2)(l-1)}\ {}_1Y_l + 6\varpi\frac{\partial}{\partial r}\varpi\frac{\partial}{\partial r}\overline{R_l^{\rm P}}\ {}_2Y_l\right], \tag{C.2}$$

$$h_{22}^{\rm P} = -\sum_{l=2}^{\infty}{\rm Re}\left(\rho^2\overline{R_l^{\rm P}}\sqrt{(l+2)(l-1)(l+1)l}\ {}_0Y_l - \frac{4}{\sqrt{2}}\varpi\overline{\rho}\overline{R_l^{\rm P}}\sqrt{(l+2)(l-1)}{}_1Y_l\right), \tag{C.3}$$

$$h^{\mathrm{P}}_{23} = \sum_{l=2}^{\infty} \left[\frac{1}{\sqrt{2}} \frac{1}{\overline{\rho}} \frac{\partial}{\partial r} \overline{\rho} \rho \overline{R^{\mathrm{P}}_l} \sqrt{(l+2)(l-1)}\ {}_1Y_l + (\varpi + \tau) \frac{\partial}{\partial r} \overline{R^{\mathrm{P}}_l}\ {}_2Y_l \right]. \tag{C.4}$$

On the other hand, h^{P}_{33} is obtained as

$$h^{\mathrm{P}}_{33} = -\sum_{l=2}^{\infty} \frac{1}{\overline{\rho}^2} \frac{\partial}{\partial r} \overline{\rho}^2 \frac{\partial}{\partial r} \overline{R^{\mathrm{P}}_l}\ {}_2Y_l. \tag{C.5}$$

Appendix D

Numerical evaluation

D.1 Spin-weighted spherical harmonics

The analytic expression of ${}_sY_{lm}(\theta,\phi)$ is given by Torres Del Castillo (2003). After some rearrangements, we have

$$\begin{aligned} {}_sY_{lm} = (-1)^m \sqrt{\frac{2l+1}{4\pi}} \sqrt{\frac{(l+m)!\,(l-m)!}{(l+s)!\,(l-s)!}} \left(\cos\frac{\theta}{2}\right)^{2l} \\ \times \sum_{k=k_{\min}}^{k_{\max}} (-1)^k \frac{(l-s)!}{(l-s-k)!\,k!} \frac{(l+s)!}{(l-m-k)!\,(s+m+k)!} \left(\tan\frac{\theta}{2}\right)^{2k+m+s} e^{im\phi}, \end{aligned} \tag{D.1}$$

where $k_{\min} = \max\{0, -m-s\}$, $k_{\max} = \min\{l-s, l-m\}$.

Because our perturbed space-time is axisymmetric, we need only $m = 0$ modes:

$$\begin{aligned} {}_sY_l \equiv {}_sY_{l0} = \sqrt{\frac{2l+1}{4\pi}} \sqrt{\frac{l!\,l!}{(l+s)!\,(l-s)!}} \left(\cos\frac{\theta}{2}\right)^{2l} \\ \times \sum_{k=k_{\min}}^{k_{\max}} (-1)^k \frac{(l-s)!}{(l-s-k)!\,k!} \frac{(l+s)!}{(l-k)!\,(s+k)!} \left(\tan\frac{\theta}{2}\right)^{2k+s}. \end{aligned} \tag{D.2}$$

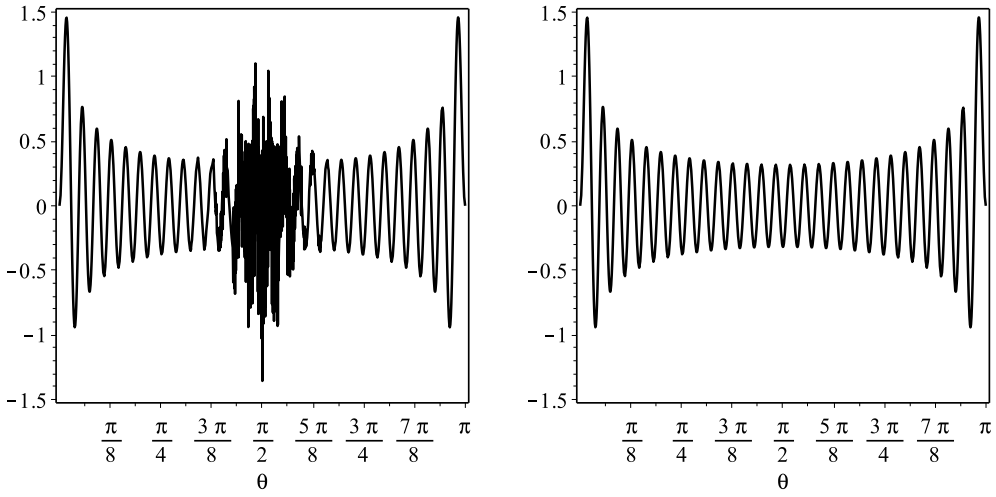

Figure D.1: Plot of ${}_{-2}Y_{56}(\theta)$ by *Maple*. Left panel: Eq. Eq. (D.2). Right panel: Eq. Eq. (D.4).

By using *Maple*, a closed-form expression is obtained:

$$
\begin{aligned}
{}_sY_l = \sqrt{\frac{2l+1}{4\pi}}\sqrt{\frac{l!\;l!}{(l+s)!\;(l-s)!}}\left(\cos\frac{\theta}{2}\right)^{2l}\left[1+\tan^2\left(\frac{\theta}{2}\right)\right]^{l}\frac{\Gamma(l+|s|+1)}{\Gamma(l+1)} \\
\times P\left(l,-|s|,\frac{1-\tan^2(\theta/2)}{1+\tan^2(\theta/2)}\right)\times\begin{cases}\left(\tan\frac{\theta}{2}\right)^{s}\left[-\left(\tan\frac{\theta}{2}\right)^2\right]^{-s/2} & (s\geq 0)\\ \left(\tan\frac{\theta}{2}\right)^{-s}\left[-\left(\tan\frac{\theta}{2}\right)^2\right]^{s/2}(-1)^{-s} & (s<0)\end{cases},
\end{aligned}
\tag{D.3}
$$

where $P(l,s,x)=P_l^s(x)$ is the Legendre function and $\Gamma(x)$ is the gamma function. Since θ is confined in $0\leq\theta\leq\pi$ in our coordinate system, $\tan(\theta/2)\geq 0$ holds. Therefore

$$
{}_sY_l = (-i)^s\sqrt{\frac{2l+1}{4\pi}}\sqrt{\frac{l!\;l!}{(l+s)!\;(l-s)!}}\frac{\Gamma(l+|s|+1)}{\Gamma(l+1)}P\left(l,-|s|,\cos\theta\right). \tag{D.4}
$$

is obtained.

Numerical evaluation of Eq. (D.2) by *Maple* becomes inaccurate when $l\gtrsim 50$. On the other hand, Eq. (D.4) does not have such a problem. See Fig. D.1.

D.2 Summation

We consider an algorithm to evaluate infinite summation such as

$$\psi_0 = \sum_{l=2}^{\infty} R_l^{(2)}(r)\ {}_2Y_l(\theta). \tag{D.5}$$

As an example we take the perturbed Weyl scalar $\psi_0(r,\theta)$ in this section. We consider the perturbed Schwarzschild space-time by a particle at rest for explicity.

Actually, analytical evaluation of this sum is possible in this case (Keidl, Friedman, & Wiseman 2007). However, we do not expect that it is possible in the cases of more complicated models. Therefore we need numerical evaluation of this summation.

The typical plot of $R_l^{(2)}(r)\ {}_2Y_l(\theta)$ as a function of l is shown in Fig. D.2. The coordinates (r,θ) are fixed at $(8M,\ \pi/4)$. The value oscillates, mainly due to the angular harmonics ${}_2Y_l(\theta)$. Because the amplitude of this oscillation decreases with l, we evaluate the summation by truncating at some $l_{\max}$, which has to be large enough. However, determining appropriate value of $l_{\max}$ is not very simple. For example, if we set $l_{\max} = 50$ by observing the left panel of Fig. D.2, the resultant plot of $\mathrm{Re}(\psi_0)$ artificially blows up near $r = r_0$. Even if we set $l_{\max} = 100$, it still blows up. See the left panel of Fig. D.3. On the other hand, at points far from $r = r_0$, $l_{\max} = 50$ seems to be large enough so that the value converges. That means to compute $50 \lesssim l \leq 100$ modes at such region (r,θ) is a waste. The middle and right panel of Fig. D.3 show the radial dependence of $R_l^{(2)}(r)$ at different point r. We observe that the value $R_l^{(2)}(r)$ for smaller $|r - r_0|$ decays at larger l. Thus, for efficiency, we should truncate at different $l_{\max}$, depending on r and probably also on θ.

We do not give $l_{\max}$ as a function of (r,θ), instead we introduce a procedure to judge if the sum converges at each point (r,θ). Below we consider how to judge it. One might think that it converges when the following relation holds:

$$\left| R_{l_{\max}}^{(2)}\ {}_2Y_{l_{\max}} \right| \ll \left| \sum_{l=2}^{l_{\max}} R_l^{(2)} {}_2Y_l \right|. \tag{D.6}$$

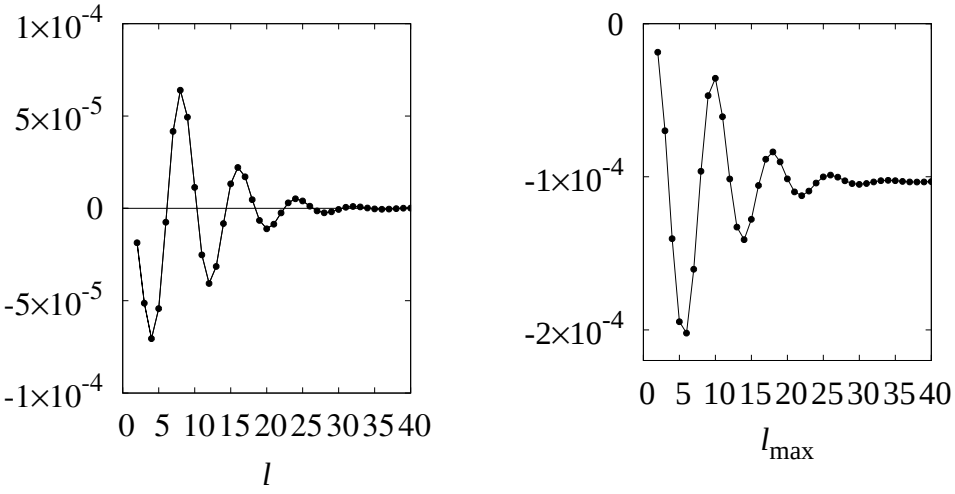

Figure D.2: The left panel: The l dependence of ${R_l^{(2)}}_2Y_l$ at $(r,\theta) = (8M, \pi/4)$. The amplitude of the oscillation decreases with l. The right panel: The $l_{\max}$ dependence of $\sum_{l=2}^{l_{\max}} {R_l^{(2)}}_2Y_l$ at $(r,\theta) = (8M, \pi/4)$.

However, since the mode ${R_l^{(2)}}_2Y_l$ oscillates with l, it is actually less accurate to truncate at $l = l_{\max}$ which gives small $|{R_l^{(2)}}_2Y_l|$. It is because such an $l_{\max}$ gives an extremal value of $\sum_{l=2}^{l_{\max}} {R_l^{(2)}}_2Y_l$, thus that value is relatively far from the convergent value. See Fig. D.2 again. The right panel shows the $l_{\max}$ dependence of $\sum_{l=2}^{l_{\max}} {R_l^{(2)}}_2Y_l$. It is more accurate to truncate when the difference between two consecutive extremal values is small compared to their average:

$$\left| \sum_{l=2}^{l_i} {R_l^{(2)}}_2Y_l - \sum_{l=2}^{l_{i+1}} {R_l^{(2)}}_2Y_l \right| \ll \frac{1}{2} \left| \sum_{l=2}^{l_i} {R_l^{(2)}}_2Y_l + \sum_{l=2}^{l_{i+1}} {R_l^{(2)}}_2Y_l \right|, \tag{D.7}$$

where l_i gives the ith extremal value $\sum_{l=2}^{l_i} {R_l^{(2)}}_2Y_l$.

Finally, when $l_{\max}$ becomes large enough, we take the average of two consecutive extremal values as the numerical evaluation of the infinite summation.

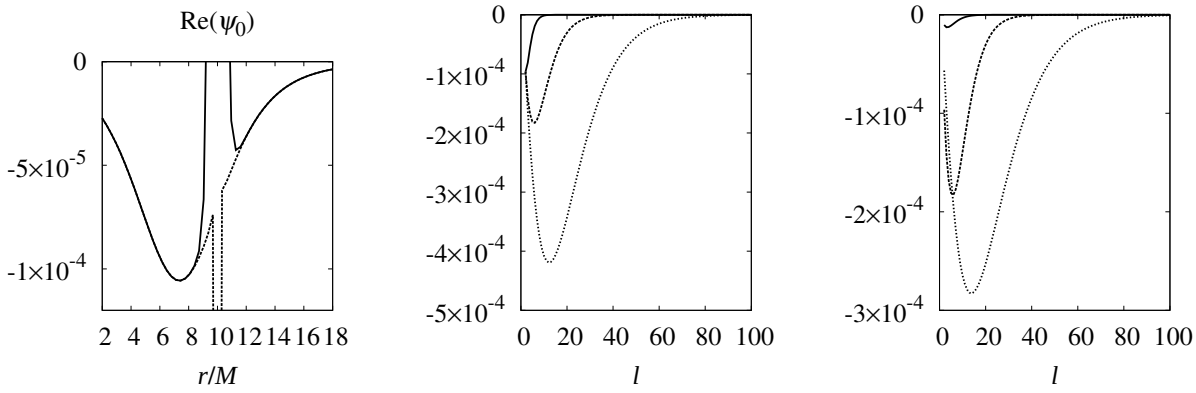

Figure D.3: The left panel: The radial dependence of $\mathrm{Re}(\psi_0)$, by evaluating with constant $l_{\max}$. The angular coordinate is fixed at $\theta = \pi/4$. The solid line is for $l_{\max} = 50$ and the dashed line is for $l_{\max} = 100$. At $9.9M \lesssim r \lesssim 10.1M$, $l_{\max} = 100$ is not large enough. The middle and right panel: The l dependence of $R_l^{(2)}(r)$ at different value of r. The left panel: The solid line is for $r = 5M$, the dashed line is for $r = 8M$, and the dotted line (the rightmost one) is for $r = 9M$. The right panel: The solid line is for $r = 15M$, the dashed line is for $r = 12M$, and the dotted line (the rightmost one) is for $r = 11M$. The position of the particle is $r_0 = 10M$. The value $R_l^{(2)}(r)$ for smaller $|r - r_0|$ decays at larger l.

Bibliography

Amaro-Seoane, P., Aoudia, S., Babak, S., Binetruy, P., Berti, E., Bohe, A., *et al.* 2012, arXiv:1201.3621

Amaro-Seoane, P., Gair, J. R., Pound, A., Hughes, S. A., & Sopuerta, C. F. 2014, arXiv:1410.0958

Barack, L., & Ori, A. 2001, PRD, 64, 124003

Chandrasekhar, S. 1983, The Mathematical Theory of Black Holes (Oxford University Press, New York)

Chrzanowki, P. L. 1975, PRD, 11, 2042

Cohen, J. M., & Kegeles, L. S. 1974, PRD, 10, 1070

Cohen, J. M., & Kegeles, L. S. 1975, Physics Letters54 A, 1

Crowder, J., & Cornish, N. J. 2005, PRD, 72, 083005

Dennison, K. A., & Baumgarte, T. W. 2012, PRD, 86, 084051

Eisenhart, L. P. 1960, "Riemannian Geometry", Princeton University Press, Princeton, New Jersey

Geroch, R., Held, A., & Penrose, R. 1973, JMP, 14, 874

Goldberg, J. N., Macfarlane, A. J., Newman, E. T., Rohrlich, F., & Sudarshan E. C. G. 1967, JMP, 8, 2155

Gralla, S. E., & Wald, R. M. 2008, Class. Quant. Grav., 25, 205009

Kawamura, S., Ando, M., Seto, N., Sato, S., Nakamura, T., Tsunobno, K., *et al.* 2011, Class. Quant. Grav., 28, 094011

Kegeles, L. S., & Cohen, J. M. 1979, PRD, 19, 1641

Keidl, T. S., Friedman, J. L., & Wiseman, A. G. 2007, PRD, 75, 124009

Keidl, T. S., Shah, A. G., Friedman, J. L., Kim, D.-H., & Price, L. R. 2010, PRD, 82, 124012

Mino, Y., Sasaki, M., & Tanaka, T. 1997, PRD, 55, 3457

Mundim, B. C., Nakano, H., Yunes, N., Campanelli, M., Noble, S. C., & Zlochower, Y. 2014, PRD, 89, 084008

Nakamura, T., Oohara, K., & Kojima, Y. 1987, PTPS, 90

Newman, E. T., & Penrose, R. 1962, JMP, 3, 566

Newman, E. T., & Penrose, R. 1966, JMP, 7, 863

Nichols, D. A., Owen, R., Zhang, F., Zimmerman, A., Brink, J., Chen, Y., *et al.* 2011, PRD, 84, 124014

Nichols, D. A., Zimmerman, A., Chen, Y., Lovelace, G., Matthews, K. D., Owen, R., *et al.* 2012, PRD, 86, 104028

Nisbet, A. 1955, Proc. R. Soc. Lond., A 1955 231, 1185, 250

Ori, A. 2003, PRD, 67, 124010

Poisson, E., Pound, A., & Vega, I. 2011, Living Reviews in Relativity, 14, 7

Pound, A. 2010, PRD, 81, 024023

Pound, A., Merlin, C., & Barack, L. 2014, PRD, 89, 024009

Quinn, T. C., & Wald, R. M. 1997, PRD, 56, 3381

Regge, T., & Wheeler, J. A. 1957, PRD, 108, 1063

Sano, Y., & Tagoshi, H. 2014, PRD, 90, 044043

Sano, Y., & Tagoshi, H. 2015, arXiv:1412.8607; PRD (submitted)

Seto, N., Kawamura, S., & Nakamura, T. 2011, PRL, 87, 221103

Shah, A. G., Keidl, T., S., Friedman, J. L., Kim, D.-H., & Price, L. R. 2012, PRD, 83, 064018

Shah, A. G., Friedman, J. L., & Keidl, T. S. 2012, PRD, 86, 084059

Stewart, J. M. 1989, Proc. Roy. Soc. Lond., A 367, 527

Teukoslky, S. A. 1972, PRL, 29, 1114

Teukolsky, S. A. 1973, ApJ, 185, 635

Torres del Castillo, G. F. 2003, "3-D Spinors, Spin-Weighted Functions and their Applications", Progress in Mathematical Physics, 32, Birkhäuser, Boston

Wald, R. M. 1973, JMP, 14, 1453

Wald, R. M. 1978, PRL, 41, 203

Wald, R. M. 1984, "General Relativity", The Univiersity of Chicago Press, Chicago & London

Zerilli, F. J. 1970, PRD, 2, 2141

Zhang, F., Zimmerman, A., Nichols, D. A., Chen, Y., Lovelace, G., Matthews, K. D., *et al.* 2012, PRD, 86, 084049

List of my papers

- Sano, Y., & Tagoshi, H. 2014, PRD, 90, 044043
- Sano, Y., & Tagoshi, H. 2015, PRD, submitted. (arXiv:1412.8607)